OUKA
The University of Osaka
Institutional Knowledge Archive

Title	Study on Self-Assembly and Chiral Recognition of Thiaheterohelicene Derivatives on the Ag(111) surface
Author(s)	Ye, Changqing
Citation	大阪大学, 2026, 博士論文
Version Type	VoR
URL	https://doi.org/10.18910/105435
rights	
Note	

The University of Osaka Institutional Knowledge Archive : OUKA

https://ir.library.osaka-u.ac.jp/

The University of Osaka

Doctoral Dissertation

Study on Self-Assembly and Chiral Recognition of Thiaheterohelicene Derivatives on the Ag(111) surface

(Ag(111)表面におけるチアヘテロヘリセン誘導体の自己組織化およびキラル認識に関する研究)

YE CHANGQING

January 2026

Graduate School of Engineering,

The University of Osaka

Abstract

Chiral recognition at nanoscale is a fundamental issue in surface science, attracting both significant scientific interest in the hierarchy of chiral progression and broad practical applications such as molecular sensing and asymmetric catalysis, and so on. Despite extensive experimental and theoretical studies, the mechanism of chiral recognition at the nanoscale is still open to debate. Helicenes, with their rigid helical structure, serves as an ideal model system for studying chiral behavior in two-dimensional environments. In this thesis, the adsorption, self-assembly, and chiral recognition behaviors of thiaheterohelicenes on Ag(111) has been investigated by density functional theory (DFT) calculations, molecular dynamics (MD) simulations, and scanning tunneling microscopy (STM).

First, the adsorption and self-assembly of racemic [7]thiaheterohelicene ([7]TH) was investigated using DFT calculations and MD simulations to explore the early stage of the structural formation on the surface, which is difficult to elucidated by experimental observation. DFT calculations revealed an adsorption geometry where one terminal of the molecule lies nearly flat on the surface. MD simulations demonstrated that [7]TH preferentially forms heterochiral dimers, which act as fundamental building blocks and further assemble into zigzag chain structures stabilized by π–π interactions between neighboring helical backbones. The resulting alternating enantiomer arrangement reproduces the characteristic features observed in STM images, indicating that intermolecular interactions dominate the self-assembly process of [7]TH.

Next, the role of functional groups at the terminal of the helicene backbone clarified by using 2,13-dihydroxymethyl-[7]TH ([7]TH-diol). STM measurements showed that both racemic and enantiopure [7]TH-diol form similar zigzag chain structures on Ag(111). MD simulations revealed distinct molecular recognition mechanisms for structure formation: van der Waals interactions between helical skeletons dominated in heterochiral chains of the racemic system, while hydrogen bonding between hydroxymethyl groups stabilizes homochiral chains in the enantiopure system. The zigzag chain motifs observed in STM images were reproduced in MD simulations, indicating that intermolecular interactions play a dominant role over molecule–substrate interactions in the ordered structure. These results demonstrate that terminal functional groups can substantially modify intermolecular recognition mechanisms without necessarily altering the resulting self-assembly motifs.

Finally, the self-assembly behavior of racemic [5]thiaheterohelicene ([5]TH) was investigated to clarify the role of molecular length in chiral recognition. DFT

calculations revealed pronounced site- and orientation-dependent adsorption of [5]TH on Ag(111), while its intrinsic intermolecular interactions were found to be weak and energetically similar among different homochiral and heterochiral dimers. Deviations from preferred adsorption sites and orientations on Ag(111) result in an energy cost nearly an order of magnitude larger than that associated with deviations from optimal intermolecular distances dictated by intermolecular interactions alone. This energetic hierarchy indicates that self-assembly is governed primarily by substrate registry, with intermolecular interactions acting as secondary constraints. Consequently, the ordered structures observed experimentally can be rationalized as a balance in which molecules anchor at their preferred adsorption sites and orientations on the substrate, while locally adopting dimer motifs favored by intermolecular interactions. These findings provide insight into how helical length controls the balance between intermolecular and molecule–substrate interactions in chiral self-assembly on Ag(111).

Contents

1 Introduction **1**
- 1.1 Research Motivation 1
- 1.2 Outline of Thesis 3

2 Research Background **5**
- 2.1 Chiral Molecules 5
  - 2.1.1 Molecular Chirality 5
  - 2.1.2 Definition of Chirality 6
- 2.2 Molecular Chirality at Interfaces: Assembly and Recognition on Surfaces. 7
  - 2.2.1 Basic Properties of Helicene 8
  - 2.2.2 Carbohelicenes and Their Derivatives on Solid Surfaces . . 9
  - 2.2.3 Thiaheterohelicene and Their Derivatives 19

3 Methods **27**
- 3.1 Density functional theory 27
  - 3.1.1 Hohenberg–Kohn Theorems 28
  - 3.1.2 Kohn–Sham Equations 29
  - 3.1.3 Tersoff–Hamann Approximation 31
- 3.2 Molecular dynamics simulations 32
  - 3.2.1 Force Field: General AMBER Force Field (GAFF) 32
  - 3.2.2 Numerical Integration: Verlet Algorithm 36
  - 3.2.3 Temperture Control: Thermostat 37
- 3.3 Scanning Tunneling Microscopy 41

4 Chiral Recognition Mechanism of Two-Dimensional Self-Assembly Formed by [7]Thiaheterohelicene **45**
- 4.1 Introduction 45
- 4.2 Methods 46
  - 4.2.1 Computational Details of DFT Calculations 46
  - 4.2.2 Computational Details of MD Simulations 47

4.3 Adsorption Geometry of [7]TH on Ag(111) 52
4.4 Formation Mechanism of Chain Structures 54
4.5 Molecular Configurations of Neighboring Chain Pairs 61
4.6 Conclusions 64

5 Chiral Recognition Mechanism of 2,13-Bis(hydroxymethyl)-[7]Thiaheterohelicene on Ag(111) Investigated by STM and MD Simulations 65
5.1 Introduction 65
5.2 Methods 66
5.3 STM Observation of Ordered Structures of [7]TH-diol on Ag(111) . 68
5.4 MD simulations of [7]TH-diol 70
5.4.1 Dimer Conformations 70
5.4.2 Formation of Chain-like Structures 72
5.4.3 Role of Functional Groups in Molecular Arrangements . . . 80
5.5 Conclusions 82

6 Interplay of Molecule–Substrate and Intermolecular Interactions in [5]Thiaheterohelicene Assembly on Ag(111) 83
6.1 Introduction 83
6.2 Methods 85
6.3 MD Investigation of Intrinsic Molecular Recognition of [5]TH . . . 86
6.3.1 Single-Molecule Adsorption of [5]TH on Ag(111) 91
6.4 Intermolecular Interactions of [5]TH Dimers 93
6.5 Competition between Adsorption-Site Registry and Intermolecular Distance Optimization 96
6.6 Molecular Models of Ordered [5]TH Structures 98
6.7 Effect of Helical Structure on Intermolecular and Molecule–Substrate Interactions 99
6.8 Conclusions 100

7 Summary 103

Acknowledgments 107

Publication List 109

References 111

Chapter 1

Introduction

1.1 Research Motivation

Chirality describes the property of asymmetry in objects, where an object and its mirror image cannot be superimposed onto each other. One familiar example from our daily life is the distinction between our left and right hands. This characteristic is commonly observed in nature. For example, most snails have right-handed spiral shells, and the shell handedness determines their mating behavior and internal organ arrangement.[1,2] Certain fish, such as flatfish, exhibit pronounced left-handed asymmetries in body structure.[3] On the other hand, in the case of plants, climbing vines typically twist in a consistent clockwise or anticlockwise direction, and some flowers display visibly chiral patterns in their petals.[4–7] Even in the mineral world, crystals like quartz can form chiral structures, exhibiting different optical rotations depending on the handedness of the crystal and the wavelengths of light.[8,9]

In the 19th century, Louis Pasteur made a remarkable contribution to the understanding of molecular chirality. While studying the crystal morphology of tartaric acid and its salts, he observed that they formed chiral crystals. He then examined the sodium ammonium salt of paratartaric acid (which was later found to be a racemic mixture of tartaric acid) and manually separated its crystals with opposite handedness. After dissolving them, he found that each solution rotated plane-polarized light in opposite directions, confirming their optical activity.[10–12] Pasteur's findings connect macroscopic chirality of crystals to the properties of molecular arrangements in the microscopic world, providing the first clear evidence that chirality also exists at the molecular level.

Since then, it has become clear that chirality plays a critical role in biological systems.[13–19] Many biomolecules, such as amino acids and sugars, exhibit chiral, and only one of their enantiomers is typically found in nature. This phenomenon is known as homochirality.[20–22] For instance, natural amino acids almost exclusively exist in left-handed form, leading to the formation of chiral peptides and conse-

quently, proteins with hierarchical organized three-dimensional structures.[23–25] Homochirality is essential for the specific molecular recognition that occur during physiological processes, including enzyme-substrate interactions,[26–31] the helical architecture of DNA,[32–36] and cellular signaling pathways.[37–40] It also results in the human ability to strictly recognize different enantiomers of chiral compounds.[41–44] For example, (*R*)-limonene smells like oranges, while (*S*)-limonene smells like lemons, we distinguish fruits from odor due to different enantiomers.[45,46] In pharmaceutical field, thalidomide was used as sedative, however, only one enantiomer had the intended therapeutic effect, while the other caused severe birth defects.[47,48] Despite such cases, many synthetic drugs are still produced as racemic mixtures. These examples illustrate how molecular chirality can result in different biological effects and highlight the importance of understanding chiral recognition mechanisms at the nanoscale.

Inspired by the selective interactions between chiral molecules, researchers have developed a wide range of applications that rely on chiral recognition, such as asymmetric catalysis,[49–51] and chiral sensing.[52–54] Understanding chiral recognition at the nanoscale is therefore essential, not only for advancing fundamental science research but also for promoting practical applications in fields such as biochemistry, pharmacology, and materials science.[18,29,30,40,49–54]

Introducing chirality onto surface enables the development of two-dimensional chiral systems, offering a well-defined and controllable environment for investigating chiral recognition mechanism at the molecular level. In particular, the advent of scanning tunneling microscopy (STM) has made it possible to directly visualize individual molecules on surfaces with molecular resolution.[55–57] The adsorption of small chiral and prochiral molecules onto solid surfaces, where they form enantiomorphic configurations through self-assembly or surface-mediated synthesis, has recently attracted significant attention.[58–60] These systems provide valuable insights into the fundamental origins of chirality in complex biological and chemical systems, and serve as a basis for designing novel chiral nanomaterials with tailored properties.

Helicenes[61–63] are a class of ortho-condensed polycyclic aromatic compounds characterized by unique screw-like, helical structures. Due to steric hindrance between the tailing aromatic rings, helicene exhibit inherent chirality despite absence of asymmetric carbon atoms. The two enantiomers are denoted as left-handed ((*M*)-type) and right-handed ((*P*)-type), depending on the twisting direction of the molecular skeleton. Since their first synthesis in the early 20th century, helicenes have attracted increasing attention owing to their pronounced chiroptical properties, such as strong circular dichroism and circularly polarized luminescence. These features make them promising candidates for optoelectronic materials and so on.[63–65] Furthermore, due to their rigid helical skeleton and high thermal stability, helicenes

have become an ideal model for constructing two-dimensional chiral systems on surfaces. Self-assembled structures of helicenes on various surfaces have been extensively investigated using STM, providing a typical platform for exploring phenomena such as chiral recognition, enantioselective adsorption, and surface-mediated chirality transfer.[66–69]

However, in contrast to carbohelcienes, research on heterohelices, a class of helicenes that consists of one or more heteroaromatic rings, has been relatively limited.[61] Among these, our group has particularly focused on thiaheterohelicenes, which consist of alternating thiophene and benzene rings. The presence of thiophene rings at the terminal of the molecular skeleton facilitates synthetic modifications, enabling the molecules being easily functionalized. Taking advantage of this structural flexibility, our group have investigated different derivatives of [7]thiaheterohelicenes using STM to explore their adsorption behavior, as well as chiral recognition mechanisms in self-assembled structures.[70–73]

Although helicenes have been extensively studied on metal surfaces using STM, the mechanisms of chiral recognition among different ordered structures remain unclear. This is mainly due to the difficulty in identifying the chirality of individual enantiomers and determining their precise molecular orientations. To address these problems, theoretical calculations, such as density functional theory (DFT) calculations and molecular dynamics (MD) simulations, play a crucial role in elucidating detailed molecular arrangements and evaluating both molecule–molecule and molecule–substrate interactions.[69,74–76]

Therefore, in this work, I investigated the adsorption and self-assembly behavior of thiaheterohelicene on Ag(111), focusing on how molecular structure, chirality, and functional groups influence the formation of two-dimensional molecular assemblies and the mechanisms of chiral recognition. A combination of STM observation, DFT calculations, and MD simulations was employed to provide both experimental and theoretical insights into molecular recognition of chiral molecules at the nanoscale.

1.2 Outline of Thesis

This thesis is organized into seven chapters, each addressing a different aspect of the study on the self-assembly and chiral recognition of thiaheterohelicenes on Ag(111):

Chapter 2 provides a general introduction to chiral molecules, including definition and classification of chirality. Then, it presents helicenes as a typical model system exhibiting inherent chirality (helicity), and introduces some basic properties of the molecules. Finally, it reviews recent research progress on the self-assembly and chiral recognition behaviors of helicenes on solid surfaces, including

both carbohelicenes and thiaheterohelicenes.

Chapter 3 describes the experimental and computational methods used in this study. STM was used to observe molecular arrangements on surfaces, while DFT calculations and MD simulations were employed to investigate adsorption behavior, and chiral recognition among the molecules.

Chapter 4 studys the self-assembly behavior of racemic [7]thiaheterohelicene ([7]TH) on Ag(111). Using DFT and MD simulations, the early-stage formation of zigzag chain structures is analyzed. The role of intermolecular interactions in driving long-range chain growth is discussed, and the results are compared with previous STM observations.

Chapter 5 explores the chiral recognition behavior of 2,13-dihydroxymethyl-[7]thiaheterohelicene ([7]TH-diol). STM experiments and MD simulations are combined to investigate the differences in two-dimensional self-assembly behavior between racemic and enantiopure molecules. The influence of functional groups on chiral recognition is discussed.

Chapter 6 presents a theoretical study on [5]thiaheterohelicene ([5]TH), which has a shorter helical length than [7]TH. DFT and MD simulations are used to investigate how reduced molecular length and helicity affect adsorption behavior and stereochemical recognition on Ag(111).

Chapter 7 summarizes the main conclusions of this work and offers perspectives for future research.

Chapter 2

Research Background

Chirality is a fundamental geometrical property of molecules that has profound implications in chemistry, biology, and materials science. The spatial arrangement of atoms within a chiral molecule leads to unique behaviors, especially in interactions with other chiral systems. In particular, understanding how chiral molecules behave at solid surfaces has become increasingly important for advancing enantioselective catalysis, molecular recognition, and the design of functional chiral materials.

This chapter begins with an overview of molecular chirality, including its definitions and classifications, followed by a brief introduction to helicenes, a class of inherent chiral molecular compounds characterized by their helical structures. Recent studies on the self-assembly and molecular recognition of helicene-based systems, including carbohelicenes and thiaheterohelienes are then discussed.

2.1 Chiral Molecules

2.1.1 Molecular Chirality

The word 'chiral' was first introduced by Lord Kelvin, it originates from the Greek word '$\chi\varepsilon\iota\rho$', meaning "hand".[77] Chirality is one of the most important geometric properties of a molecule, where a molecule cannot be superimposed on its mirror image. Therefore, molecules that exhibit this property always have two different stereoisomers, known as enantiomers. A pair of enantiomers share identical physical properties, such as melting and boiling points, solubility, density, as well as the same chemical reactivity in isotropic environments. However, they differ in their interactions with polarized light, where each enantiomer rotates the plane of polarization in opposite directions. More importantly, enantiomers can interact with other chiral molecules in a different ways.

Many biomolecules, such as amino acids and sugars, are chiral, and in nearly

all cases, only one of their enantiomers is found in nature. This phenomenon is known as homochirality. Because of this, living bodies such as humans are able to precisely distinguish between different chiral compounds. For examples, (*R*)-limonene smells like oranges, while (*S*)-limonene smells like lemons.[45,46] Similarly, one enantiomers of (*L*)-aspartame tastes sweet while (*D*)-aspartame is tasteless.[78] Many synthesis drugs are also chiral and are typically produced as racemic mixture, which contain equal amounts of both enantiomers. However, often only one enantiomer provides the desired therapeutic effect, while the other may be inactive or even cause harmful side effects.[40,48,79] These phenomena highlight the critical importance of understanding the chiral recognition mechanisms, particularly at the nanoscale, where subtle differences in molecular geometry and interactions play a decisive role.

Although the concept of molecular chirality and its spontaneous resolution dates back to 1848, when Louis Pasteur manually separated left- and right-handed ammonium sodium tartrate crystals and analyzed their optical activities in solution,[10,11] the mechanism of chiral recognition at the nanoscale remains under active debate.

2.1.2 Definition of Chirality

This asymmetric property can arise from various structural features,[80] as illustrated in Figure 2.1.

Central chirality is the most common form, typically found in organic compounds. It occurs when molecule has a chiral center, often a carbon bonded to four different substituents. Axial chirality appears when a molecule has a chiral axis, such as biaryl compounds with restricted rotation around a single bond. Planar chirality occurs when a molecule has a chiral plane. This is usually observed in cyclic or bridged structures with asymmetric substitution. Helicity describes chirality in molecules with a helical or screw-like structures, for example, DNA, protein, and artificial compounds, like helicenes.[62] These structures lack mirror symmetry due to their twisted geometry.

The absolute configurations of chiral molecules can be described using several stereochemical nomenclature systems, depending on the molecular structure. The most widely used system was introduced by Cahn, Ingold, and Prelog.[81,82] For molecules with chiral centers, *R* (from the Latin rectus, meaning right) describes a configuration in which the priority of substituents proceeds clockwise around the chiral center, while *S* (from the Latin sinister, meaning left) describes a anticlockwise arrangement. For molecules exhibiting helical or axial chirality, such as helicenes, *P* (plus) denotes a right-handed helix, while *M* (minus) denotes a left-handed helix. Additionally, *D/L* designation, based on Fischer convention, is still commonly used in biochemistry, especially for sugars and amino acids.[83,84] This

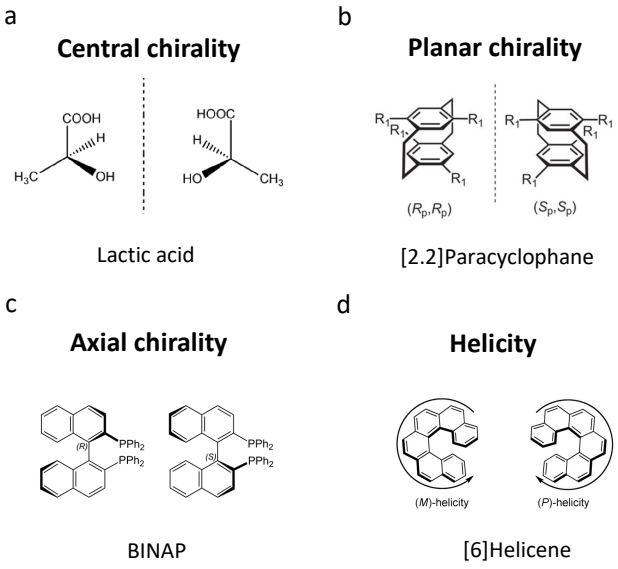


Figure 2.1: Typical examples of different types of chirality. (a) Lactic acid with central chirality. (b) Planar chiral [2.2]Paracyclophane substituted in four positions. (c) 2,2'-bis(diphenylphosphino)-1,1'-binaphthyl (BINAP) with axial chirality. (d) [6]helicene with helicity.

system assigns configuration relative to that of glyceraldehyde, with *D* indicating that the reference group is on the right side, and *L* indicating it is on the left.

2.2 Molecular Chirality at Interfaces: Assembly and Recognition on Surfaces.

Understanding the principles of intermolecular recognition is a challenging task that requires researchers to study well-designed model systems. Introducing chirality onto solid surface enables the development of well-defined two-dimensional chiral systems, which serve as ideal platforms for investigating chiral recognition mechanisms among molecular systems at the nanoscale.

Intrinsic chiral molecules can exhibit complex and informative self-assembled structures on surfaces. In such systems, molecular chirality can be transferred to the surfaces through subtle molecule–molecule and molecule–substrate interactions. Among various chiral molecules, helicenes, a class of polycyclic aromatic compounds characterized by helical structures, have been widely used as an ideal model systems for investigating chiral recognition mechanisms on the solid surfaces.

In the following section, I first briefly introduces the basic properties of helicenes

and then focuses on the two-dimensional self-assembled structures formed by helicenes and their derivatives on solid surfaces.

2.2.1 Basic Properties of Helicene

Helicenes are a class of chiral molecular compounds with screw-like, helical structures formed through consecutive ortho-condensed benzene or other aromatic rings. Their nomenclature is based on the number of aromatic rings that consist in their helical skeleton.[61] The notation $[n]$ indicates the number of aromatic rings in the structure. Typically, only compounds with five or more aromatic rings are classified as helicenes, since those with fewer than five rings lack sufficient steric strain and exhibit nearly planar structures.

Helicenes composed solely of benzene rings are referred to as carbohelicenes, whereas those incorporating heteroatoms (such as sulfur or nitrogen) into the helical skeletons are classified as heterohelicenes. For example, helicenes containing thiophene rings are referred to as $[n]$thiaheterohelicenes.

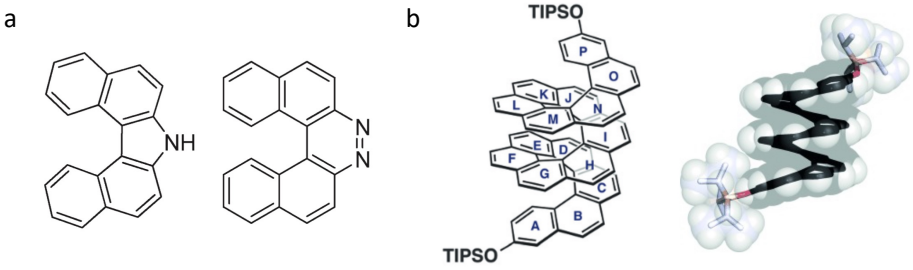


Figure 2.2: (a) The first synthesized helicene compounds.[85] (b) The longest orth-fused helicene [16]helicene.[86]

The concept of helically shaped polyaromatic hydrocarbons dates back to the early twentieth century. The first compounds recognized as helicene (shown in Figure 2.2a) were synthesized by J. Meisenheimer and K. Witte in 1903.[85] In 1918, M. S. Newman and his co-workers successfully synthesized [5]helicene, and in 1955, reported the synthesis of the first [6]helicene.[87–89] The longest orth-fused helicene reported to date is [16]helicene (Figure 2.2b), which was synthesized by K. Mori *et al.* in 2015.[86] More recently, expanded [23]helicene, a class of helical nanocarbonds compsed of alternating linear and angularly fused aromatic rings, has been reported by G. R. Kiel *et al.*.[90]

Due to significant steric hindrance between the tailing aromatic rings, the molecular skeleton twists into a helical conformation. This results into two enantiomeric forms: a right-handed ((*P*)-type for "plus") helix and a left-handed ((*M*)-type for "minus") helix, as shown in Figure 2.3a.[80] Consequently, helicenes exhibit

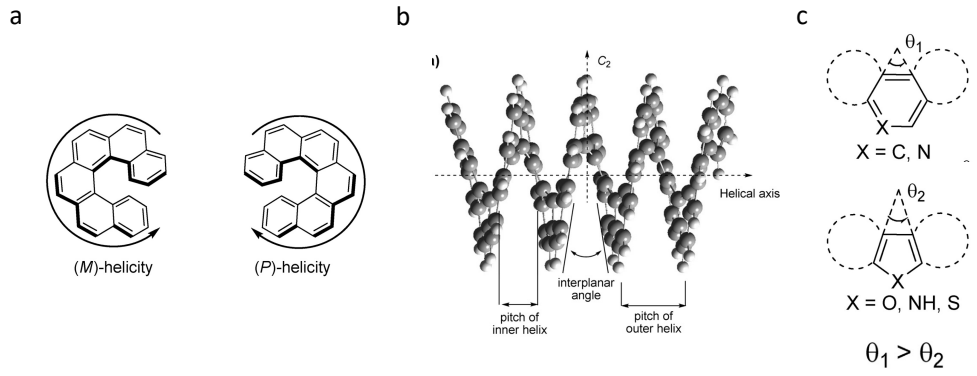


Figure 2.3: (a) Helical structure of helicene enantiomers. (b) Ball-and-stick model of [18]helicene, which exhibits a cylindrical structure with a constant pitch in both the inner and outer helices. (c) Comparison of the in-plane turn (θ) of six-member and five-member rings.[61]

a C_2-symmetry axis perpendicular to the helical axis. This intrinsic helical structure gives rise to axial chirality (also helicity), even in the absence of chiral centers.

As the number of aromatic rings increases, the helicene extends along its helical axis and gradually form a cylindrical structure with a constant pitch in both the inner and outer helices, as shown in Figure 2.3b).[91] For helicenes composed of six-membered rings, approximately six rings are needed to complete a full 360° turn.[92] While in the case of thiaheterohelicenes, four thiophene and three benzene rings are required,[93] due to smaller in-plane angular distribution (Figure 2.3c).[94]

The nonplanar structure of helicenes arises from the torsion between connected aromatic rings. The inter-planar (or dihedral) angle between the two terminal rings depends on molecular length and the substituents present. For instance, in carbohelicenes, this angle increases as the molecule is extended from [4]helicene (26.70°) to [6]helicene(58.5°).[61] However, with further elongation, the angle starts to decrease, in [11]helicene, the angle between terminal rings is only 4°.[95]

2.2.2 Carbohelicenes and Their Derivatives on Solid Surfaces

Among helicenes, carbo[7]helicene ([7]CH) is one of the most extensively studied due to its well-defined helical structure (Figure 2.4a). When adsorbed on surfaces such as (111) surfaces of Ag, Au, and Cu, [7]CH tends to be adsorbed with one terminal lying nearly parallel to the surface plane, as shown in Figure 2.4b.

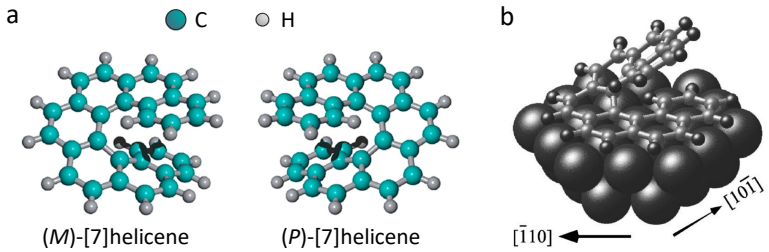


Figure 2.4: (a) Ball-and-stick-models for the two [7]CH enantiomers. (b) Adsorption geometry of (*M*)-[7]CH on the Cu(111) surface.Reproduced with permission from refs.[96] © 2008 and American Chemical Society, and 2001 American Institute of Physics.

Molecular Chirality Transmission from Single Molecules to Molecular Monolayer

When adsorbed onto the (111) surfaces of Ag, Au, and Cu, enantiopure (*M*)-[7]CH forms a highly ordered, threefold symmetric self-assembled structures (referred as triplets), as illustrated in Figure 2.5.[96–98] Each bright spot observed in the STM images corresponds to a single molecule, highlighted by white circle in Figure 2.5a. Molecular modeling reveals that the molecules within each unit cell are rotated by 120° relative to one another (Figure 2.5f–h). The uppermost part of helicene appears as a bright lobe in the STM images, therefore, the rotational alignment of three molecules gives rise to the characteristic triplet appearance. Notably, these well-ordered chiral structures emerge predominantly at coverages approaching monolayer saturation ($\theta \approx 1.0$).

On all three (111) surfaces, the triplets of (*M*)-[7]CH exhibits a clockwise tilt relative to the [$1\bar{1}0$] direction of the substrate surface. On Ag(111) and Au(111), the short unit cell vector tilts by approximately $10° \pm 2°$, as indicated by green lines in Figure 2.5a, b. On Cu(111), the tilt angle increases to 13.3°, shown by the angle between the red frame and yellow arrow in Figure 2.5e. Due to the nearly identical interatomic distances of Ag and Au surfaces (d = 288 pm), the triplet structures formed on Ag(111) and Au(111) are almost identical. In contrast, the more compact arrangement observed on Cu(111) reflects its smaller atomic distance (d = 255 pm). Thus, molecular chirality is transferred through stereochemical recognition both among neighboring molecules and between molecules and specific adsorption sites on the surface. In addition, the opposite enantiomer, (*P*)-[7]CH, forms a mirror-symmetric structure exhibiting a anticlockwise tilt relative to the high-symmetry direction of the substrate.

At a lower coverage ($\theta < 1.0$), two different self-assembled structures are

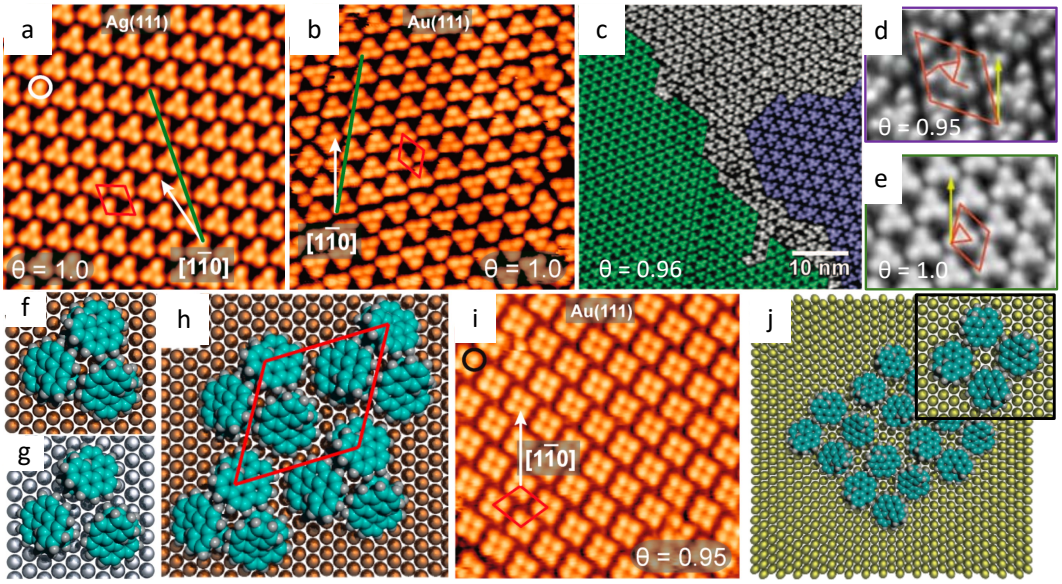


Figure 2.5: Self-assembled structures formed by (*M*)-[7]CH on the (111) and (100) surfaces of Ag, Au, and Cu. STM images (20×20 nm^2) of triplet patterns forming by (*M*)-[7]CH on the (a) Ag(111) and (b) Au(111) surfaces at saturated coverage (θ = 1.0). (c) STM image (50×50 nm^2) of (*M*)-[7]CH on Cu(111) at θ = 0.96, where both "triplet" (green area) and "pinwheel" (purple area) coexist on the surface terrace. The unit cells of (d) "pinwheel" phase which composed of six-molecule pinwheel and three-molecule triplet patterns, and (e) "triplet" phase which composed exclusively triplet patterns. Structural models of triplet pattern on the (f) Cu(111) and (g) Ag(111) surfaces, respectively. (h) Unit cell of the triplet pattern on the Cu(111) surface. (i) STM image 50×50 nm^2) of (*M*)-[7]CH on Au(111) at θ = 0.95, where the molecules form quadruplet pattern. (j) Unit cell of quadruplet pattern on the Au(111) surface. The STM images were obtained at (a) 2.90 V, 21 pA; (b) –2.90 V, 43 pA; (c) 2.05 V, 19 pA; (i) 2.73 V, 26 pA. Reproduced with permission from refs[98],[96], and[97]. © 2008 and 2014 American Chemical Society, and 2003 Wiley-VCH Verlag GmbH & Co. KGaA, Weinheim.

observed on the Cu(111) and Au(111) surfaces. On the Cu(111) surface, a ”6+3” pinwheel-like structure” consisting of six molecules is formed and shows either a clockwise or anti-clockwise arrangement (Figure 2.5e), indicating the transmission of chirality into self-assembled structures by azimuthal orientations of the molecules. In contrast, the molecules form a long-range ordered structures of quadruplet
(Figure 2.5i) on the Au(111) surface, where the molecules are rotated by 90° within each unit (Figure 2.5j). These fourfold symmetric patterns exist at low coverages and persist up to monolayer saturated coverage (θ = 1.0).

Prevalent Chain Structures Formed by Helicene Racemates

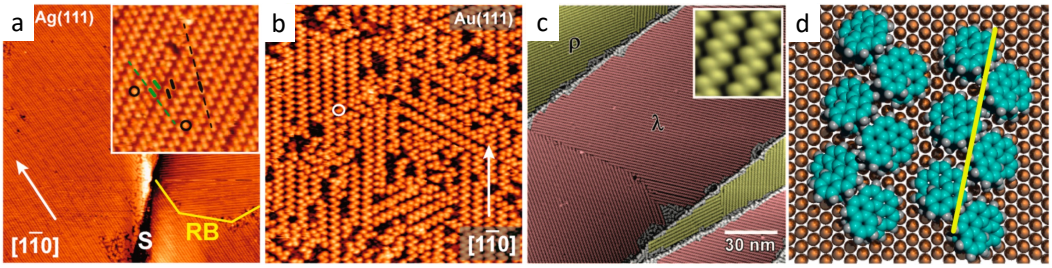


Figure 2.6: Zigzag chain structures formed by *rac*-[7]CH on the (a) Ag(111), (b) Au(111), and (c) Cu(111) surfaces. (d) Structural model of zigzag chains of *rac*-[7]CH on the Cu(111) surface. The STM images were obtained at (a) 200×200 nm^2, 2.78 V, 11 pA, (the inset) 20×20 nm^2, 1.23 V, 59 pA; (b) 40×40 nm^2, 2.78 V, 11 pA; (c) 150×150 nm^2, 2.61 V, 20 pA. Reproduced with permission from refs[98],[96]. © 2008 and 2014 American Chemical Society.

After deposition of *rac*-[7]CH onto the (111) surfaces of Ag, Au, Cu, ordered structures are observed only at coverages approaching a saturated monolayer. These structures are characterized as zigzag chains (Figure 2.6), in which the molecules adopt an alternating arrangement of (*M*)- and (*P*)-type enantiomers within each chain. Compared to the triplet patterns of (*M*)-[7]CH, the formation of heterochiral zigzag chains indicates that no spontaneous resolution of [7]CH enantiomers occur on the (111) surfaces of Ag, Au, and Cu.

On the Cu(111) surface, mirror domains are formed due to different oblique alignments of zigzag chains, as indicated by the yellow and red areas in Figure 2.6c. The chains in two mirror domains run tilted by opposite angles of ±10.9° with respect to the [1$\bar{1}$0] direction of the (111) surface. As shown in the molecular model in Figure 2.6d shown, the molecules within the zigzag chains are considered being adsorbed on identical adsorption sites on Cu(111).

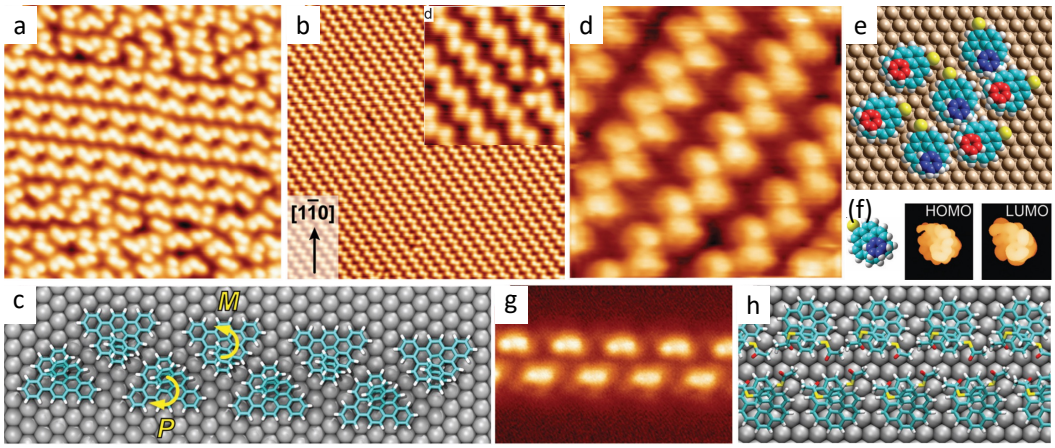


Figure 2.7: Self-assembled structures formed by three different [7]CH derivatives on the (111) surfaces of Au, Ag. STM images of zigzag chain structures of *rac*-db[7]CH on Ag(111) at (a) 0.8 ML, and (b) 1.0 ML. (c) Chain model of *rac*-db[7]CH on Ag(111) based on force field mediated molecular dynamics. (d) STM image of zigzag chains formed by *rac*-Br[7]CH on Au(111). (e) Chain model of *rac*-Br[7]CH on Au(111) based on STM and AMBER force field calculations. (f) Electron density of LUMO (right) and HOMO (middle) according to the orientation of *rac*-Br[7]CH (left). (g) STM image of zigzag chain structure formed by *rac*-AT[7]CH on Ag(111). (h)Chain model *rac*-AT[7]CH on Ag(111) relaxed by MD simulations. The STM were obtained at (a) 25×25 nm^2, 0.5 V, 20 pA; (b) 50×50 nm^2, 350 mV, 10 pA; (the inset) 8×8 nm^2, 350 mV, 10 pA; (d) 9.3×9.3 nm^2, –2.8 V, 23 pA; (g) 4.5×3 nm^2, 30 mV, 2.8 pA. Reproduced with permission from refs[75]. © The Royal Society of Chemistry 2019.

In contrast, on the Ag(111) surface, the zigzag chains align along highly symmetric directions of the surface, and therefore, no mirror domains are formed (Figure 2.6a). Due to the larger interatomic distance of Ag, stress accumulates within the racemic molecular layer, which results in relaxation into different structural phase after every third or fourth zigzag chain. While on the Au(111) surface, no well-defined long-range ordered structure is observed, as shown in Figure 2.6b. This may be attributed to surface reconstruction on Au(111), which disrupts regular molecular arrangements.

Similar zigzag chain structures have also been observed for racemic mixtures of several [7]CH derivatives on Ag(111) and Au(111).[75] In all cases, (*M*)- and (*P*)-type enantiomers arrange alternatingly along the chain direction, revealing heterochiral recognition among the molecules.

At low coverage, dibenzo-heptahelicene (db[7]CH) form heterochiral dimers on Ag(111). As coverage increase, the molecules assemble into heterochiral trimers,

which are considered precursors of zigzag chain. At saturated monolayer coverage, the zigzag chain structures dominate the surface terraces and align parallel to the highly symmetric direction of (111) surface.

Similarly, 9-bromo-heptahelicene (Br[7]CH) forms long-range ordered zigzag chains on Au(111), and chains are oriented parallel to the highly symmetric direction of the surface. Compared to [7]CH, the presence of Br atoms does not modify the preference for heterochiral recognition, suggesting that Br. . . Br interactions are weak among the molecules. MD simulations indicate that Br atoms are adsorbed on bridge site of Au(111), and intermolecular distance is larger than that of [7]CH dimer. As a result, Br[7]CH exhibits better lattice matching to Au substrate, which facilitates the formation of long-range ordered structures.

In the case of S,S'-1,17-diacetothio-heptahelicene (AT[7]CH), due to the presence of acetylthiolate groups, hydrogen bonds are expected to form between the molecules. However, STM observations together with MD simulations demonstrate that the molecules instead assemble into heterochiral zigzag chains.

Competition of Homochiral and Heterochiral Recognition

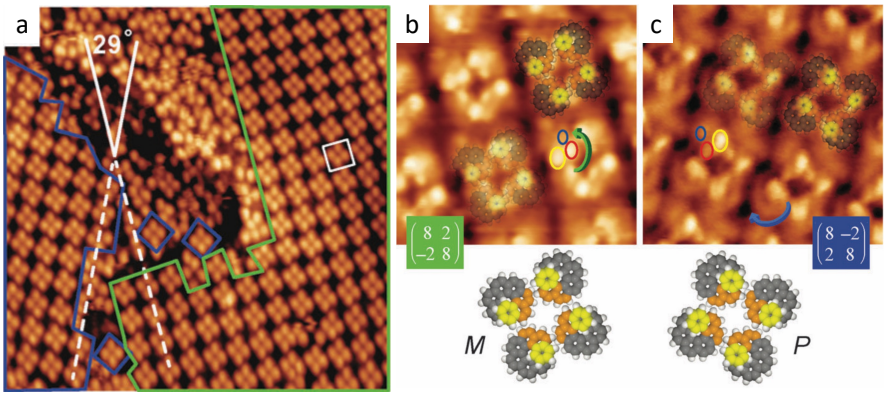


Figure 2.8: Self-assembled structures formed by *rac*-[7]CH on Cu(100). (a) STM image near a mirror-domain boundary. (b, c) STM images and molecular models of two quadruplet unit cells. The STM images were obtained at (a) 35×35 nm^2, –2.73 V, 40 pA; (b) 6×6 nm^2, 0.86 V, 179 pA; (c) 6×6 nm^2, –0.77 V, 198 pA. Reproduced with permission from refs[67]. © The Royal Society of Chemistry 2014.

On the Cu(100) surface, *rac*-[7]CH undergoes spontaneous enantiomeric resolution, whose self-assembled structures exhibit two mirror domains, as shown in Figure 2.8 a. Unlike heterochiral zigzag chains observed on Cu(111), the molecules formed homochiral quadruplet patterns, with each unit are composed of four (*M*)-

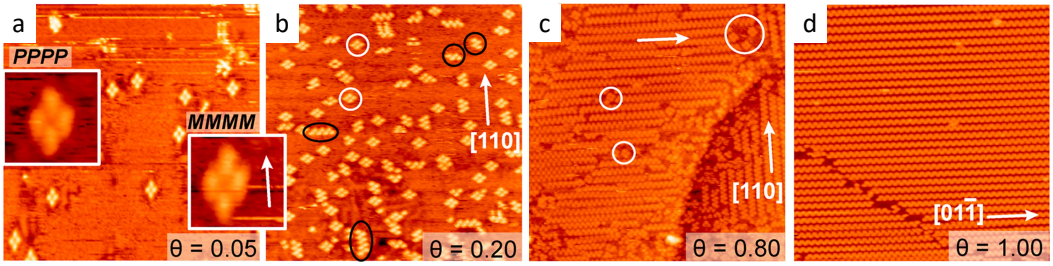


Figure 2.9: Self-assembled structures formed by *rac*-[7]CH on Ag(100) at different coverages (θ). (a) Homochiral quadruplets are observed at θ = 0.05, (b) small zigzag chains appear at θ = 0.20, (c) zigzag chain structures dominate and a few quadruplets left as defects at θ = 0.80, (d) zigzag chains fully saturated the surface terraces at θ = 1.00. The STM images were obtained at (a) 50×50 nm^2, (the insets) 5×5 nm^2, –2.84 V, 31 pA; (b) 45×45 nm^2, 2.84 V, 19 pA; (c) 60×60 nm^2, –2.73 V, 23 pA; (d) 50×50 nm^2, –2.78 V, 20 pA. Reproduced with permission from refs[99]. © 2015 American Chemical Society.

type or (*P*)-type [7]CH enantiomers. These quadruplet patterns appear at initial stage of adsorption and persist up to saturated monolayer coverage. The unit cells of two mirror-image domains are rotate ±14.5° with respect to $[01\bar{1}]$ direction of the (100) surface, as illustrated in Figure 2.8b, c. Due to favorable registry between the molecular units and the substrate lattice, all four molecules within each quadruplet are considered to be adsorbed on identical adsorption sites. This suggests that, besides intermolecular interactions, the stereochemical recognition between molecule and substrate surface also play a critical role in governing the molecular arrangements.

On the other hand, when *rac*-[7]CH is deposited onto Ag(100), a transition from homochiral nuclei to larger heterochiral motifs is observed with increasing surface coverage, as illustrate in Figure 2.9. At very low coverage (θ = 0.05), only isolated homochiral quadruplets are observed on the surface terrace, resembling those formed on Cu(100). As the coverage increase (θ = 0.20), small zigzag chain segments begin to emerge and align along the highly symmetric direction of the surface, highlighted as the black circles in Figure 2.9b. With further increase in coverage (θ = 0.80), the zigzag chains grow longer, and the quadruplets gradually disappear, remaining only near defects, as indicated by white circles in Figure 2.9c. At saturated monolayer coverage (θ = 1.00), homochiral quadruplets completely disappear and only large domains of zigzag chain structure composed of alternant (*M*)- and (*P*)-type enantiomers exist.

Force field simulations show that, at the initial nucleation stage, homochiral quadruplets are energetically more stable than heterochiral counterparts. How-

ever, as the molecular cluster grow larger, heterochiral arrangements become more favorable in energy. Therefore, the phase transition observed in experiment can be explained as follow: At early stage of adsorption, the molecules tend to occupy the energetically favorable surface sites, and the good match between homocrhial quadruplets and the substrate lattice results in a high stability. While the coverage increasing, growing mismatch between the molecular adlattice and the substate lattice induces stress in the two-dimensional molecular structure, and therefore reduce the stability of homochiral arrangements. In contrast, sufficient lateral interactions between different enantiomers, as well as the possibility of occupying favorable adsorption sites in zigzag chains, facilitate the growth of stress-free heterochiral structures at higher coverages.

Porous network formed by *rac*-[5]helicene

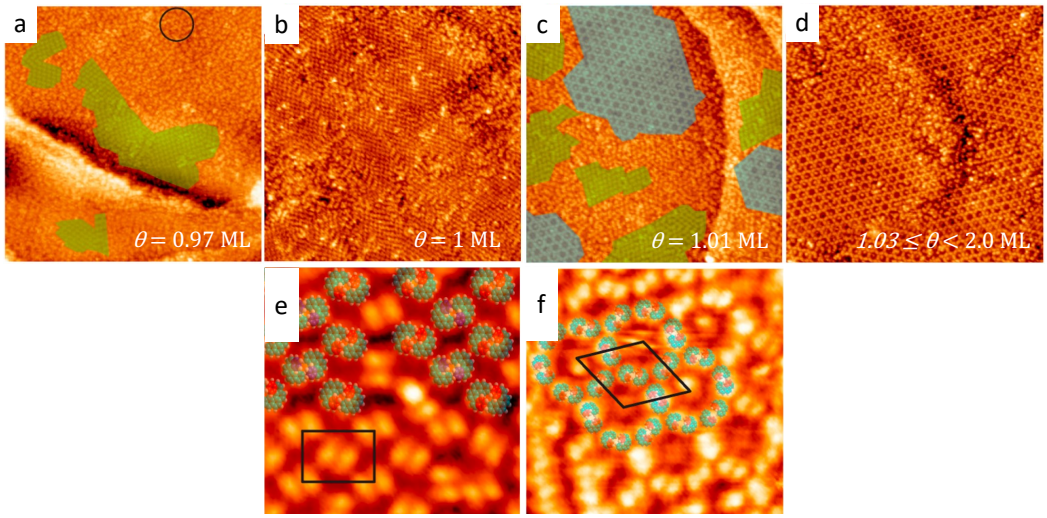


Figure 2.10: STM images (80×80 nm^2) of [5]CH on Cu(111) at different coverages. The checkerboard phase is highlighted in green and the honeycomb phase is highlighted in blue in (a) and (c). (e, f) Adsorption models imposed on STM images for checkerboard pattern and honeycomb structure, respectively. The STM images were obtained at (a) 1.78 V, 20 pA; (b) 2.27 V, 20 pA; (c) 3.27 V, 35 pA; (d) 2.84 V, 20 pA; (e) 9.5×9.5 nm^2, 2.50 V, 35 pA; (f) 8.5×8.5 nm^2, 2.50 V, 35 pA. Reproduced with permission from refs[100]. © 2017 American Chemical Society.

Due to the high mobility of [5]helicene ([5]CH) on Cu(111), the formation of long-range ordered structures is only observed at coverage close to monolayer saturation. At a coverage of θ = 0.97, ordered islands characterized by a 'checkerboard' pattern (green area in Figure 2.10a) are observed. Additionally, some patches

of honeycomb structures also emerge on the surface, as indicated by black circles in Figure 2.10a. The monolayer (θ = 1.0) is defined as the highest surface density, where only checkerboard pattern dominates the surface terraces (Figure 2.10b). As the coverage further increases, the honeycomb structures extend and become dominant (blue area in Figure 2.10c), while the checkerboard pattern gradually disappears. Finally, only honeycomb structure remains on the surface.

The basic building block of both ordered structures is a homochiral dimer of [5]CH. In the checkerboard pattern, each domain consists of homochiral dimers of both enantiomers (Figure 2.10e). Since one lattice vector of the checkerboard adlayer aligns with the $[1\bar{1}0]$ direction of the substrate, mirror domains are absent. The alternating arrangement of homochiral dimers with opposite handedness makes the checkerboard structure a racemic phase. In contrast, each domain of the honeycomb structure is composed exclusively of homochiral dimers of either (*M*)- or (*P*)-type [5]CH enantiomers. The unit cell of the honeycomb structure contains six dimers in three distinct orientations, giving rise to mirror domains that are tilted by $\pm 14 \pm 2^{\circ}$ with respect to the $[1\bar{1}0]$ direction of Cu(111). Therefore, the honeycomb structure represents an enantiomorphous phase in which spontaneous chiral resolution occurs.

From racemic checkerboard phase to conglomerate honeycomb phase, the transition in the crystallization behavior of *rac*-[5]CH on Cu(111) demonstrates that increasing molecular coverage can drive a sharp structural phase transition accompanied by chiral resolution.

A similar phase transition is observed for *rac*-[5]CH on Bi(111). At a low coverage, individual homochiral dimers and heterochiral trimers are observed on the surface (Figure 2.11 a). As the coverage increases, the molecules assemble into ordered structures composed of homochiral dimers of (*P*)-type enantiomers (Figure 2.11 b, c). The dimers have similar comformation to those observed on Cu(111). Domains containing exclusively (*M*)-type homochiral dimers are also observed on the surface, indicating enantiomeric resolution for *rac*-[5]TH.

With the further increase in the coverage, a chiral phase transition takes place from the two-dimensional conglomerate phase composed of homochiral dimers to a racemate phase composed of heterochiral trimers (Figure 2.11 d, e). The racemate phase is commensurate with the Bi(111) lattice along the high-symmetry direction, but is incommensurate along the perpendicular direction. This arrangement can thus be described as a unidirectional commensurate phase. The heterochiral [5]CH trimers exhibit a wavy alignment, attributed to the swinging of trimer rows after every second or third trimer (Figure 2.11 d). This swing mechanism is likely driven by steric repulsion between adjacent trimers of the same handedness.

Spontaneous chiral resolution of *rac*-[5]CH also occurs on Cd(0001). At full monolayer coverage, the entire surface is covered with two types of homochiral

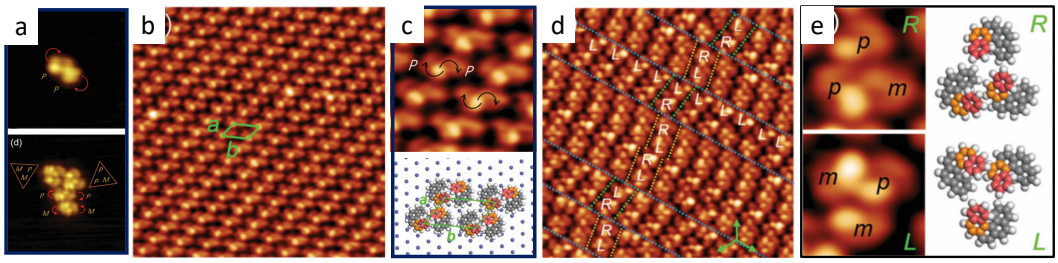


Figure 2.11: Two-dimensional crystallization of *rac*-[5]CH on Bi(111). (a) STM images of a homochiral dimer (top, 8×8 nm^2) and aggregation of two homochiral dimers and two heterochiral trimers (bottom, 10×10 nm^2). (b) STM image (20×20 nm^2) of conglomerates domain formed by (*P*)-[5]CH dimers. (c) Enlarged view (upper, 5×5 nm^2) and schematic model (bottom) of homochiral dimers. (d) STM image (20×20 nm^2) of racemic domain formed by heterochiral trimers. (e) Enlarged views (left, 2×2 nm^2) and schematic models (right) of heterochiral trimers. The STM images were obtained at (a) (top) 2.5 V, 30 pA, (bottom) 4.0 V, 30 pA; (b) 2.5 V, 30 pA; (c) 4.5 V, 30 pA; (d) 4.5 V, 30 pA. Reproduced with permission from refs[101]. © the Owner Societies 2021.

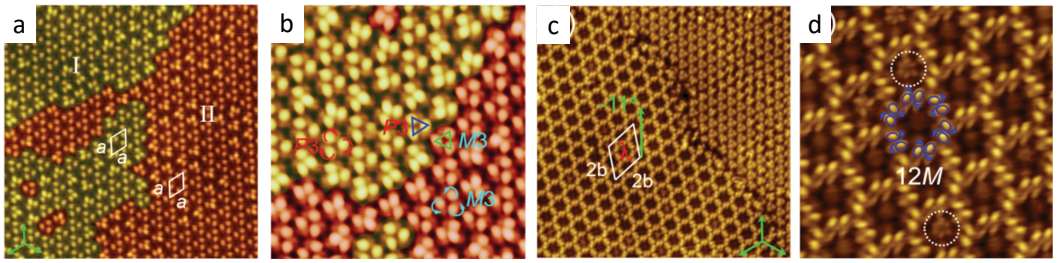


Figure 2.12: Spontaneous chirality separation *rac*-[5]CH on Cd(0001). STM images of (a) (30×30 nm^2) and (b) (15×15 nm^2) of two enantiophous domains composed of homochiral trimers coexisting on the same substrate terrace. Homochial trimers and a few heterochiral trimers exist near domain boundary. STM images of (c) (44×44 nm^2) and (d) (13×13 nm^2) of porous networks of homochiral [5]CH dimers formed after RT annealing. The building block consisting of six homochiral dimers contribute to honeycomb structure. The STM images were obtained at (a) –3.3 V, 25 pA; (b) –2.5 V, 20 pA; (c) 2.5 V, 23 pA; (d) 1.4 V, 33 pA. Reproduced with permission from refs[69]. © the Owner Societies 2022.

trimers. (*M*)-enantiomer dominated domains coexist with the (*P*)-enantiomer dominated domains on the same substrate terraces, where the two-dimensional enantiomorphism is expressed as supramolecular chirality (Figure 2.12 a, b). The racemic mixture of [5]CH is essentially separated into two mirror-image domains without oblique lattices.

Furthermore, annealing the sample to room temperature, a structural transition occurs from trimer phase to a porous network. The handedness of lattice emerges in these network structures through the formation of two enantiomorphous domains, one of which is illustrated in Figure 2.12 c. As shown in Figure 2.12 d, the unit cell of porous network is composed of six homochiral dimers of (*P*)-type enantiomers. These mirror domains show an oblique angle of $\pm 11^\circ$ with respect to the highly symmetric directions of Cd(0001), thereby restoring the lattice handedness.

The self-assembled structures with enantiomer separation of [5]CH on Cd(0001) can be attributed to the electrostatic interactions between enhanced molecular dipole moments, which are induced by strong molecule–substrate interactions.

2.2.3 Thiaheterohelicene and Their Derivatives

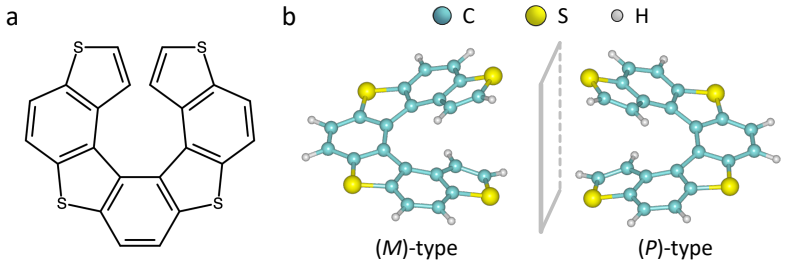


Figure 2.13: (a) Structure, and (b) Ball-and-stick model of [7]thiaheterohelicene.

Thiaheterohelicenes are a class of helcienes composed of alternating thiophene and benzene rings (Figure 2.13). The incorporation of sulfur into their helical skeletons allows for the modulation of both molecule–molecule and molecule–substrate interactions, which makes thiaheterohelicenes particularly attractive for studying chiral phenomena on solid surfaces.

Self-assembled Structures of Pristine Thiaheterohelicenes on Ag(111)

When racemic [5]thiaheterohelicene (*rac*-[5]TH) is deposited onto Ag(111), various ordered structures emerge depending on the molecular coverage. At submonolayer coverage, the molecules form a honeycomb-like structure with relative low packing density. The honeycomb structure is aligned along the $[11\bar{2}]$ direction of

the Ag(111) surface, indicating a commensurate relationship between the molecular layer and the substrate lattice (Figure 2.14 a). However, due to potential rotation within the porous network, high-resolution images of individual molecules could not be obtained. Based on statistic analysis, each unit cell of the honeycomb structure is inferred to consist of both (*M*)- and (*P*)-type enantiomers, as shown in Figure 2.14 c.

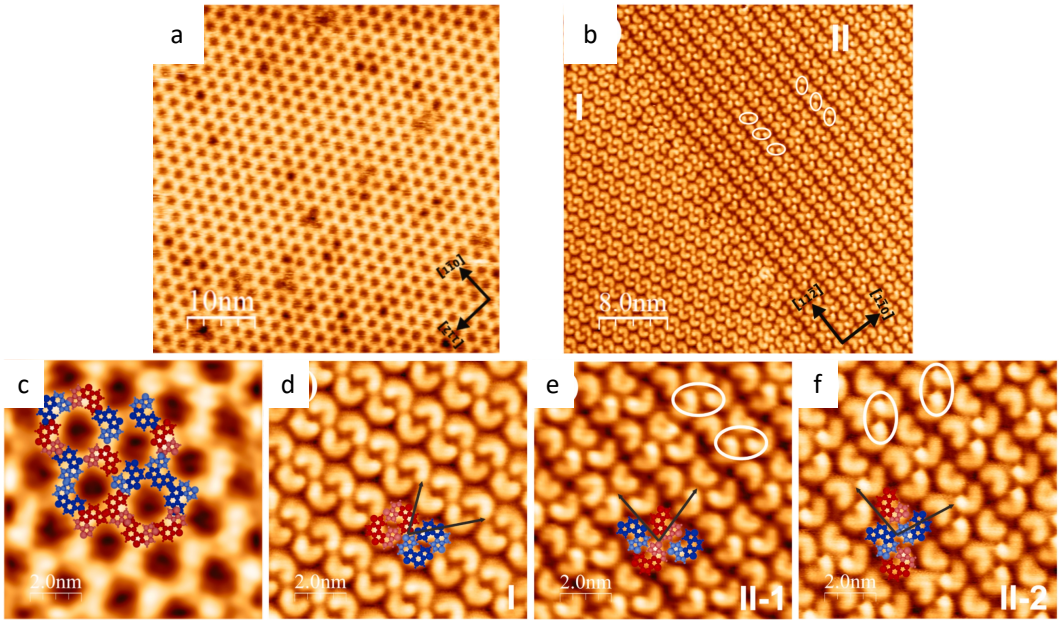


Figure 2.14: Various ordered structures of *rac*-[5]TH on Ag(111). STM images of (a) (50×50 nm^2) of honeycomb structure formed at a coverage less than 1 ML, and (b) (40×40 nm^2) of two orderded structures labelled I and II coexisting on substrate terrace. STM images (10×10 nm^2) with corresponding adsorption models of (c) honeycomb structure, (d) ordered structure I, (e, f) two phases of ordered structure II. The (*M*)-type and (*P*)-type molecules are colored in red and blue, respectively. The STM images were obtained at (a) 0.15 V, 50 pA; (b) 0.5 V, 50 pA. Reproduced with permission from refs[72]. © 2022 Elsevier B.V..

As the molecular coverage increases, *rac*-[5]TH molecules self-assembled into more compact, ordered domains consisting of regularly aligned molecular rows on Ag(111). Figure 2.14 b shows two predominant structures (labeled I and II), which coexist on the surface terrace. Individual [5]TH molecules appear as crescent-shaped features with one end appearing brighter in the STM images. Assuming the brighter end corresponds to the upper part of the molecule, molecules exhibiting a clockwise curvature are assigned to the (*P*)-enantiomer, while those with a anticlockwise curvature correspond to the (*M*)-enantiomer. Structure I consists of parallel rows tilted approximately 15±1° from the $[11\bar{2}]$ direction. Each row is

formed by homochiral dimers arranged in a face-to-face configuration, where adjacent dimers alternate between (*M*)- and (*P*)-type enantiomers (Figure 2.14 d). In contrast, structure II comprises parallel rows aligned along the $[11\bar{2}]$ direction, in which adjacent heterochiral molecules form back-to-side dimers, in which enantiomers rotate approximately 90° with respect to each other. Additionally, structure II exhibits two substructures with a relative phase shift, and two substructures are found near defects in the ordered, as illustrated in Figure 2.14 e, f.

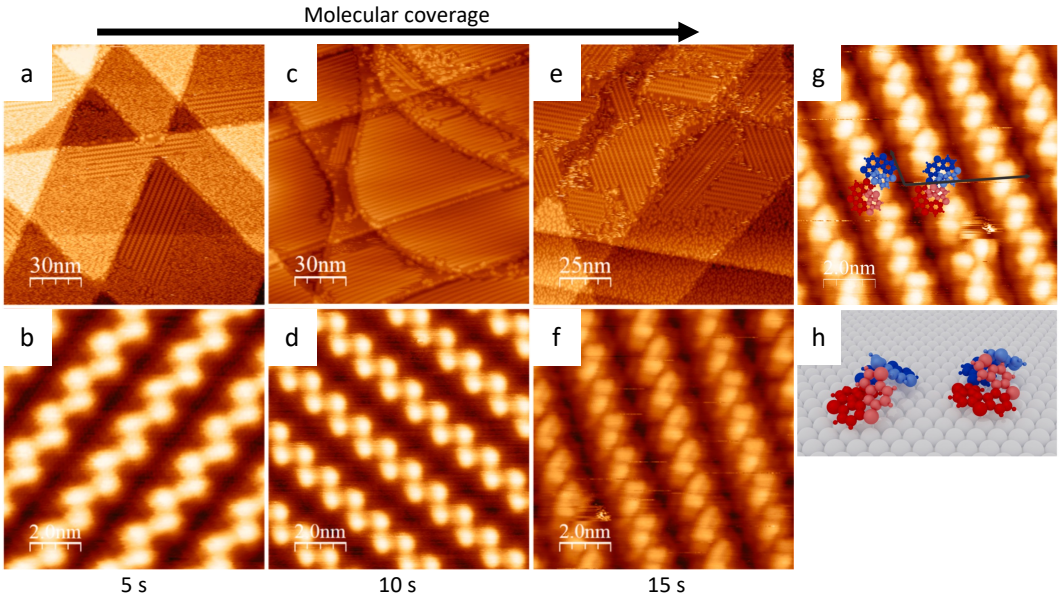


Figure 2.15: Self-assembled structures of *rac*-[7]CH on Ag(111) as a function of surface coverage, which is controlled by varying the deposition time. (a, b) Formation of small domains with zigzag chains at submonolayer coverage. (c, d) Larger domains with zigzag chains at increasing coverage. (e, f) Small domains with zigzag chains, surrounded by disordered area at saturated coverage. (g) High-resolution STM image of zigzag chain structure with adsorption model. (h) Side view of adsorption model. The (*M*)-type and (*P*)-type molecules are colored in red and blue, respectively. The STM images were obtained at (a) 150×150 nm^2, 2.5 V, 150 pA; (b) 10×10 nm^2, 2.5 V, 10 pA; (c) 150×150 nm^2, –3.5 V, 50 pA; (d) 10×10 nm^2, 2.5 V, 50 pA; (e) 125×125 nm^2, –2.6 V, 25 pA; (f) 10×10 nm^2, –2.6 V, 25 pA; (g) 10×10 nm^2, –2.6 V, 25 pA. Reproduced with permission from refs[72]. © 2022 Elsevier B.V..

Figure 2.15 shows STM images of racemic [7]thiaheterohelicene (*rac*-[7]TH) adsorbed on Ag(111), illustrating the evolution of self-assembled structures as a function of surface coverage, which are controlled by varying the deposition time. After depositing the molecules for 5 s, islands with ordered structure emerge on

the surface terrace and are surrounded by disordered area (Figure 2.15 a). Each ordered island shows a characteristic self-assembled zigzag chain structure, with no observable molecular defects within the ordered regions (Figure 2.15 b). These chains are oriented parallel to $[1\bar{1}0]$ direction of Ag(111).

As the deposition time increase from 5 s to 15 s at a temperature of 170 °C, ordered islands of zigzag chains expand on the surface (Figure 2.15 c, e). While the overall surface coverage increases with deposition time, the zigzag chain structure remains unchanged. Only slight variation in the distance between neighboring chains are observed, as shown in Figure 2.15b, d, and f. These zigzag chains are composed of alternating (*M*)-and (*P*)-type enantiomers (Figure 2.15g, h), which are similar to the chain structures reported for *rac*-[7]CH on the (111) surfaces of Ag, Au, and Cu. Notably, neighboring zigzag chains exhibit distinct molecular conformations, suggesting subtle conformational adaptations driven by intermolecular interactions.

Functional Group Effect on Self-assembled Structures of Thiaheterohelicenes

One of the main advantages of thiaheterohelicenes is the presence of thiophene rings, which can serve as anchors for different functional groups. The π-electron-rich nature of sulfur atoms in the thiophene rings lowers the activation energy required for attaching various functional segments to the helical backbone, therefore, facilitating structural modification and functionalization.

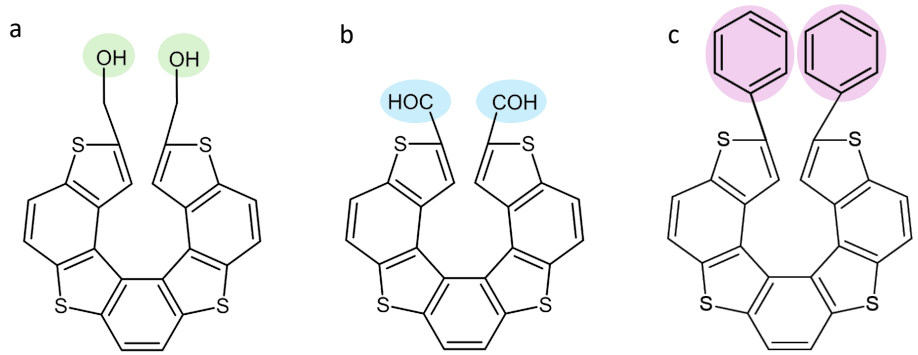


Figure 2.16: Structures of three thiaheterohelicene derivatives. (a) [7]TH-diol, (b) [7]TH-CHO, (c) [7]TH-dp.

In the following, I introduce recent investigations on chiral recognition behavior of different [7]TH derivatives on solid surfaces, namely, 2,13-dihydroxymethyl-[7]thiaheterohelicene ([7]TH-diol), 2,13-diformyl-[7]thiaheterohelicene ([7]TH-CHO), 2,13-diphenyl-[7]thiaheterohelicene ([7]TH-dp).

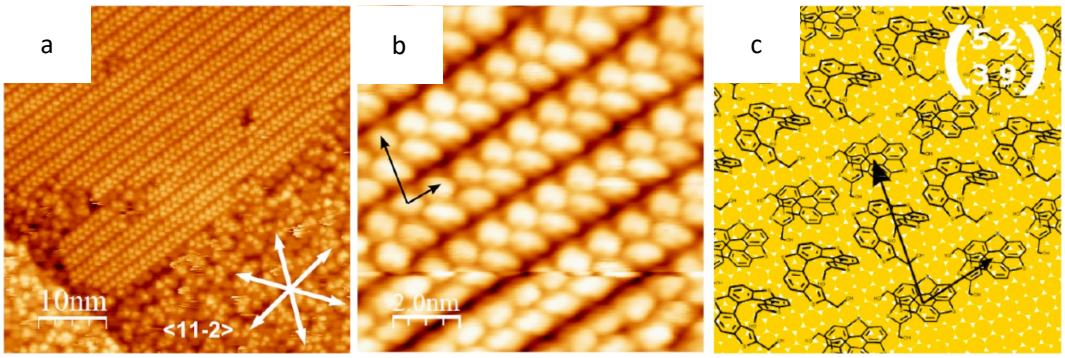


Figure 2.17: Self-assembled structures formed by (*M*)-[7]TH-diol on Au(111). (a) STM image of ordered islands of zigzag chain structures with a preferential orientation. (b) STM image and (c) corresponding molecular model of zigzag chains. The STM images were obtained at (a) –3.0 V, 50 pA; (b) –3.0 V, 15 pA. Reproduced with permission from refs[70]. © 2015 American Chemical Society.

For (*M*)-[7]TH-diol molecules on Au(111), highly ordered islands exhibiting self-assembled structures are observed, surrounded by disordered regions (Figure a). The islands consist of zigzag chain structures with preferential direction tilted clockwise and anticlockwise from the $[11\bar{2}]$ direction of the Au(111) substrate by an angle of $12 \pm 2°$. Contrast to the triplet pattern formed by (*M*)-[7]CH on Au(111), the chain structure formed by (*M*)-[7]TH-diol break the substrate symmetry. A molecular adsorption model is postulated for these zigzag chains, assuming the absence of both hydrogen bonding between the hydroxyl groups of adjacent molecules and strong π–π stacking interactions.

[7]TH-CHO is a derivative of [7]TH, whose terminal H atoms are substituted with two aldehyde groups. When *rac*-[7]TH-CHO is deposited onto Ag(111) at a saturated monolayer coverage, a zigzag chain structure is formed on the surface terrace, surrounded by disordered regions (Figure 2.18 a, b). This chain structure closely resembles those formed by (M)-[7]TH-diol, *rac*-[7]TH and some of its derivatives. Within the chains, different enantiomers are arranged alternatingly, and adjacent chains exhibit opposite conformations. As illustrated in Figure 2.18 c, two neighboring chains have (*M*)–(*P*)–(*P*)–(*M*) enantiomeric sequence from left to right. Similar to the heterochiral chains formed by [7]TH, the ordered self-assembled structures result from heterochiral recognition between the enantiomers. Although the introduction of aldehyde groups into helical backbone extends the π-conjugated structure of the molecule, it does not significantly alter the chiral recognition behavior of *rac*-[7]TH-CHO on Ag(111) compared to *rac*-[7]TH.

As shown in Figure 2.19 c, [7]TH-dp has phenyl groups at both terminals of the [7]TH backbone, resulting in an extended helical structure. Different from the linear

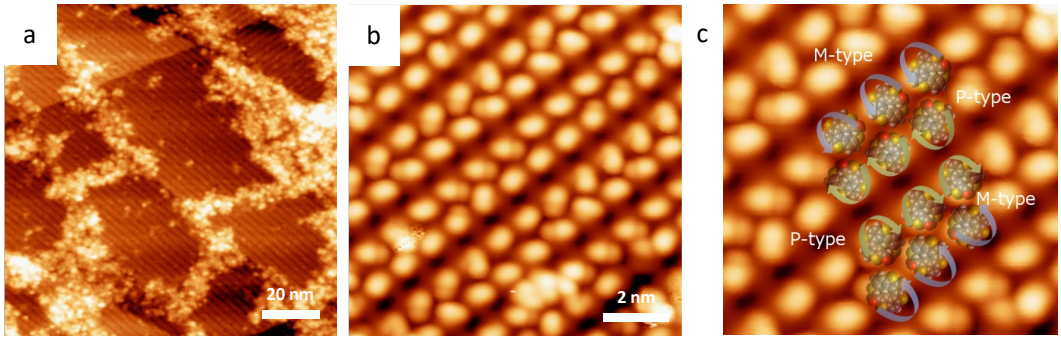


Figure 2.18: Self-assembled structures formed by (*rac*)-[7]TH-CHO on Ag(111). (a) STM image of large domains with zigzag chain structures surrounded by disordered areas. (b) High-resolution STM image and (c) adsorption model of zigzag chains. The arrows indicates the helicity of molecules that annulate towards the surface. The STM images were obtained at (a) 100×100 nm^2, 2.0 V, 20 pA; (b) 10×10 nm^2, –2.0 V, 20 pA. Reproduced with permission from refs[102].

chain structures typically observed for [7]TH and its derivatives with small functional groups, *rac*-[7]TH-dp form distinctive hexagonal motifs with curved boundaries on Ag(111), as illustrated in Figure 2.19 a. There are two types of hexagonal units, highlighted by the green and blue frame in Figure 2.19 b, are separated by curved boundaries. These hexagons are tilted $\pm15^\circ$ with respect to the $[1\bar{1}0]$ direction of Ag(111) and exhibit mirror symmetry about the step edge.

In STM images, bright protrusions appear as semi-trianglar shape with either left-handed or right-handed sense. As shown in Figure 2.19 c, each hexagonal unit comprises six same [7]TH-dp enantiomers. Therefore, the upper hexagon in Figure 2.19 c consists of (*M*)-[7]TH-dp, while the botton one consists of (*P*)-[7]TH-dp. Additionally, both (*M*)- and (*P*)-[7]TH-dp mix in curved boundary, suggesting early stage of hexagonal motif formation.

On the other hand, deposition of enantiopure (*M*)-[7]TH-dp onto Ag(111) results in a uniform distribution of homochiral hexagonal motif across the surface terrace (Figure 2.19 d). These hexagonal motifs exhibit slight distortions from a regular hexagon, reflecting the symmetry of the (111) surfaces. Each hexagonal unit consists of six molecules aligned along the $[11\bar{2}]$ direction, and there are two distinct types of bright protrusions observed in STM images (Figure 2.19 b).

Note that, careful control over the deposition amount does not alter the self-assembled structure of (*M*)-[7]TH-dp. It is presumed that the phenyl groups close to the surface adopt a flat orientation to maximize van der Waals interactions with the substrate. As depicted in the adsorption model (Figure 2.19 f), the lower phenyl groups lie outside of hexagonal unit to prevent steric hindrance with neighboring

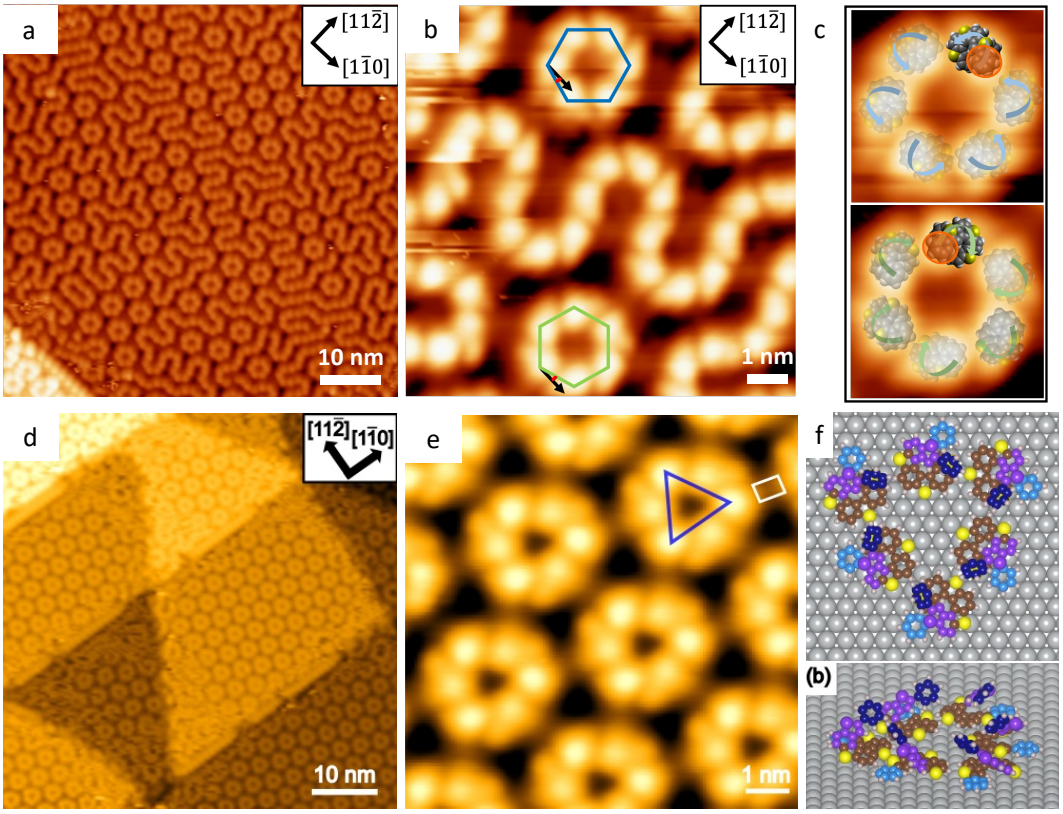


Figure 2.19: Self-assembled structures formed by [7]TH-dp on Ag(111). (a) STM image of hexagonal patterns and curved boundary formed by *rac*-[7]TH-dp. (b) Two types of hexagons with opposite titling angle with respect to [1$\bar{1}$0] surface direction are separated by the curved boundary. (c) Molecular models of two homochiral hexagons, and each is composed of six molecules. (d) STM image of exclusive hexagonal patterns formed by (*M*)-[7]TH-dp. (e) Enlarged STM image of hexagonal patterns. (f) Top view (top) and side view (bottom) of molecular model of a hexagon unit, which is composed of six molecules. The STM images were obtained at (a) 67×67 nm^2, –0.5 V, 20 pA; (b) 15×15 nm^2, 3.0 V, 20 pA; (d) 3.0 V, 50 pA; (e) 3.0 V, 50 pA. Reproduced with permission from refs[102] and[103].

molecules, while the upper phenyl groups partially overlap with adjacent helical skeletons. Based on this model, the two types of bright protrusions observed in STM images are the result of different intermolecular distance between the molecules. Therefore, steric hindrance and van der Waals interactions between adjacent molecules, together with the molecule–substrate interactions contribute to the formation of the distorted hexagonal structure of (*M*)-[7]TH-dp.

Chapter 3

Methods

This chapter introduces the fundamental concepts of the theoretical and calculation methods employed in this study, including density functional theory calculations, molecular dynamics simulations and scanning tunneling microscopy.

3.1 Density functional theory

Density functional theory (DFT) is quantum mechanical method widely used to investigate the electronic structure of atoms, molecules and condensed matter systems.[104–106] Unlike wavefunction-based approaches, such as Hartree–Fock method,[107–109] DFT uses the electro density, which is a function of three spatial variables regardless of the number of electrons, to describe the physical properties of a system. This makes DFT computationally efficient and suitable for large systems.

The electronic structure of a quantum system can be described by time-independent Schrodinger's equations. For an isolated many-electron system, it is given by

$$\widehat{H}\Psi = E\Psi \tag{3.1}$$

where $\widehat{H}$ is the Hamiltonian operator, Ψ is the many-electron wavefunction, and E is the total energy of the system.

The $\widehat{H}$ can be written as

$$\widehat{H} = \widehat{T} + \widehat{V}_{\mathrm{ne}} + \widehat{V}_{\mathrm{ee}} \tag{3.2}$$

where

$$\widehat{T} = \sum_{i=1}^{N} \left(-\frac{1}{2}\nabla_i^2 \right) \tag{3.3}$$

is the kinetic energy operator,

$$\hat{V}_{\mathrm{ne}} = \sum_{i=1}^{N} v(r_i) \tag{3.4}$$

is the electron-nucleus energy operator,

$$\hat{V}_{\mathrm{ee}} = \sum_{i<j}^{N} \frac{1}{r_{ij}} \tag{3.5}$$

is the electron-electron energy operator.

3.1.1 Hohenberg–Kohn Theorems

The foundational principle of DFT is based on the Hohenberg–Kohn theorems, which state that the ground-state properties of a many-electron system are uniquely determined by its total electron density.[110] Specifically, for a many-electron system, the external potential $v(r)$ together with the number of electrons N, fully determines all the electronic properties of the system.

The first Hohenberg–Kohn theorem states that the external potential $v(r)$, and therefore the total energy and all other ground-state properties of a system, are uniquely determined by the ground-state electron density $\rho(r)$. This theorem allows the electron density $\rho(r)$ to replace $v(r)$ and the number of electrons N as the fundamental variable in determining the properties of an electronic system. It establishes a one-to-one correspondence between the ground-state electron density and the external potential.

Considering two different external potentials v and v', that both yield the same ground-state electron density ρ for an N-electron system. These potentials correspond to two different Hamiltonians, $\widehat{H}$ and $\widehat{H}'$, and therefore, are associated with different ground-state wavefunctions, Ψ and Ψ', respectively. If we now use Ψ' as a trial wavefunction for $\widehat{H}$, it yields:

$$E_0 < \langle \Psi' | \widehat{H} | \Psi' \rangle = \langle \Psi' | \widehat{H}' | \Psi' \rangle + \langle \Psi' | \widehat{H} - \widehat{H}' | \Psi' \rangle = E_0' + \int \rho(r)[v(r) - v'(r)]dr \tag{3.6}$$

where E_0 and E_0' are the ground-state energies for $\widehat{H}$ and $\widehat{H}'$, respectively. Similarly, taking Ψ as a trial wavefunction for $\widehat{H}'$, we obtain:

$$E_0' < \langle \Psi | \widehat{H}' | \Psi \rangle = \langle \Psi | \widehat{H} | \Psi \rangle + \langle \Psi | \widehat{H}' - \widehat{H} | \Psi \rangle = E_0 + \int \rho(r)[v'(r) - v(r)]dr \tag{3.7}$$

Adding Eq. (3.6) and Eq. (3.7) leads to

$$E_0 + E_0' < E_0' + E_0 \tag{3.8}$$

which is a contradiction. Therefore, there cannot exist two different external potential that produce the same ground-state electron density for a specific system.

The second Hohenberg–Kohn theorem states that the ground-state energy of a system is minimized when the electron density corresponds to the true ground state. This establishes a variational principle for the energy, whereby any trial electron density yields an energy equal to or greater than the true ground-state energy.

According to the first Hohenberg–Kohn theorem, a given electron density $\rho(r)$ determines its unique $v(r)$, and $v(r)$ together with N determine Hamiltonian $\widehat{H}$, and hence the wavefunction Ψ. Therefore, the Ψ is a functional of $\rho(r)$, and so is the expectation value of observable $\widehat{F}$. That is,

$$F[\rho(r)] = \langle \Psi | \hat{F} | \Psi \rangle \tag{3.9}$$

where $F[\rho] = T[\rho] + \hat{V}_{ee}[\rho]$.

The total energy functional $E_v[\rho(r)]$, which depends on the external potential v, can be expressed as,

$$E_v[\rho'(r)] = \int \rho'(r) v(r) dr + F[\rho'(r)] \tag{3.10}$$

According to the variational principle, for any trial wavefunction Ψ' corresponding to a trial density $\rho'(r)$, the total energy satisfies:

$$\langle \Psi' | \hat{F} | \Psi' \rangle + \langle \Psi' | \hat{V} | \Psi' \rangle > \langle \Psi | \hat{F} | \Psi \rangle + \langle \Psi | \hat{V} | \Psi \rangle \tag{3.11}$$

where Ψ is the wavefunction corresponding to the ground-state electron density $\rho(r)$. This can also be expressed as:

$$\int \rho'(r) v(r) dr + F[\rho'(r)] > \int \rho(r) v(r) dr + F[\rho(r)] \tag{3.12}$$

Therefore, the variational principle of the second Hohenberg–Kohn theorem is obtained:

$$E_v[\rho'(r)] > E_v[\rho(r)] \tag{3.13}$$

3.1.2 Kohn–Sham Equations

Although the Hohenberg–Kohn theorems establish that the ground-state energy is a functional of the electron density, they do not provide the exact form of the universal functional $F(\rho)$, which includes kinetic and electro-electron interaction energies.

To solve this problem, Walter Kohn and Lu Jeu Sham proposed a practical scheme that simplifies the many-body problem.[104,111] In Kohn–Sham density functional theory, the interacting many-electron system is replaced with a fictitious system of non-interacting electrons that move in an local, effective external potential called Kohn–Sham effective potential $v_{\text{eff}}(r)$. This fictitious system is constructed to reproduces the same electron density as the true interacting system.

The Hamiltonian of the system is defined as:

$$\widehat{H}_{\text{s}} = \sum_{i}^{N} \left(-\frac{1}{2}\nabla_i^2 \right) + \sum_{i}^{N} v_{\text{s}}(r) \tag{3.14}$$

in which the electron-electron repulsion term is absent. Correspondingly, the ground-sate wavefunction is determined by one-electron orbitals $\psi_i(r_i)$ as:

$$\Psi_{\text{s}} = \frac{1}{\sqrt{N!}} \det[\psi_1 \psi_2 \dots \psi_N] \tag{3.15}$$

where ψ_i are the lowest eigenstates and satisfy the single-particle Kohn–Sham equations:

$$\widehat{h}_{\text{s}}\psi_i = \left[-\frac{1}{2}\nabla^2 + v_{\text{s}}(r) \right] \psi_i = \varepsilon_i \psi_i \tag{3.16}$$

The kinetic energy for the non-interacting particles is given by:

$$T_{\text{s}}[\rho] = \langle \Psi_{\text{s}} \left| \sum_{i}^{N} \left(-\frac{1}{2}\nabla_i^2 \right) \right| \Psi_{\text{s}} \rangle = \sum_{i}^{N} \langle \Psi_{\text{s}} \left| -\frac{1}{2}\nabla_i^2 \right| \Psi_{\text{s}} \rangle \tag{3.17}$$

For this fictitious system of non-interacting electrons, the universal functional $F[\rho]$ can be expressed as:

$$F[\rho] = T_{\text{s}}[\rho] + J[\rho] + E_{\text{xc}}[\rho] \tag{3.18}$$

where:

$$E_{\text{xc}}[\rho] \equiv T[\rho] - T_{\text{s}}[\rho] + \hat{V}_{\text{ee}} - J[\rho] \tag{3.19}$$

is the exchange-correlation energy,

$$J[\rho] = \frac{1}{2} \int \frac{\rho(r)\rho(r')}{|r - r'|} dr dr' \tag{3.20}$$

is the classical electrostatic repulsion (Hartree energy).

Here, $T[\rho]$ and $V_{\text{ee}}[\rho]$ are the kinetic and electron–electron interaction energies of the true interacting system. The exchange-correlation energy $E_{\text{xc}}[\rho]$ thus

accounts for intrinsic many-body effect of exchange-correlation and store the difference energy between T and T_{s}.

The Kohn-Sham equation is represented as:

$$\left[-\frac{1}{2}\nabla^2 + v_{\mathrm{eff}}(r)\right]\psi_i = \varepsilon_i \psi_i \tag{3.21}$$

$$v_{\mathrm{eff}}(r) = v(r) + \frac{\delta J[\rho]}{\delta\rho(r)} + \frac{\delta E_{\mathrm{xc}}[\rho]}{\delta\rho(r)} = v(r) + \int \frac{\rho(r')}{|r-r'|}dr' + v_{\mathrm{xc}}(r) \tag{3.22}$$

$$\rho(r) = \sum_i^N \sum_s |\psi_i(r,s)|^2 \tag{3.23}$$

where $v_{\mathrm{eff}}(r)$ is the effective potential in which non-interacting particles move, and $v_{\mathrm{xc}}(r)$ defines the exchange-correlation potential as:

$$v_{\mathrm{xc}}(r) = \frac{\delta E_{\mathrm{xc}}[\rho]}{\delta\rho(r)} \tag{3.24}$$

The total energy of the system can be obtained by:

$$E = \sum_i^N \varepsilon_i + \frac{1}{2}\int \frac{\rho(r)\rho(r')}{|r-r'|}drdr' + E_{\mathrm{xc}}[\rho] - \int v_{\mathrm{xc}}(r)\rho(r)dr \tag{3.25}$$

where

$$\sum_i^N \varepsilon_i = \sum_i^N \langle\psi_i \left| -\frac{1}{2}\nabla^2 + v_{\mathrm{eff}}(r) \right| \psi_i\rangle = T_{\mathrm{s}}[\rho] + \int v_{\mathrm{eff}}(r)\rho(r)dr \tag{3.26}$$

3.1.3 Tersoff–Hamann Approximation

The Tersoff–Hamann approximation[112,113] is a theoretical model developed by J. Tersoff and D. R. Hamann to describe the tunneling process between a real surface and a model probe tip in STM. This model provides a simplified way to simulate STM images based on the local density of states (LDOS) of a surface.

In this approach, the tip is modeled as locally spherical potential well, whose wavefunction is spherically symmetric and centered at the tip apex. Under this approximation, the tunneling current is found to be directly proportional to the surface LDOS at the Fermi level E_F at the position of the tip and at the energy corresponding to the applied bias voltage V. The tunneling current I at bias voltage V is given by:

$$I(V) \propto \int_{E_F}^{E_F+eV} \rho_s(\mathbf{r}_0, E)dE \tag{3.27}$$

where $\rho_s(\mathbf{r}_0, E) = \sum_\nu |\psi_\nu(\mathbf{r}_0)|^2 \delta(E - E_\nu)$ represents LDOS of the sample at the tip position r_0 and energy E.

In constant current mode, the STM image corresponds to the surface height $z(x, y)$ at which the integrated LDOS reached a constant value, which reflecting the electronic topography of the surface.

3.2 Molecular dynamics simulations

Molecular dynamics (MD) is a computational method used to simulate the motion of atoms and molecules over time.[114–116] Unlike quantum mechanical methods such as density functional theory introduced in the previous section, which explicitly account for the electronic structure of system, MD treats all atoms as classical particles and neglects electronic motions. This approximation enables the study of much larger systems consisting of significant numbers of atoms.

In MD, the time-dependent behavior of an atomic/molecular system is explored by integrating Newton's equations of motion. The position of each atom is updatd at each time step based on the net forces acting upon it. The motion of an atom i is governed by Newton's second law, expressed as:

$$\frac{d^2 r_i}{dt^2} = \frac{F_i}{m_i} \tag{3.28}$$

where r, F, m represent the position, net force, and mass of atom i, respectively. These forces are typically derived from empirical or semi-empirical interatomic potential (force field).

By iteratively calculating the positions and velocities of atoms over short time intervals (timestep), MD generates a trajectory that captures the time evolution of the system. The general workflow of MD simulations, including initialization, force calculation, integration of motion, is illustrated in Figure 3.1.

In the following, the force field and other computational algorithms including motion integration and temperature control used in this study are introduced.

3.2.1 Force Field: General AMBER Force Field (GAFF)

To calculate the forces acting on acting on each atom in MD simulations, one of the most essential component is the force field: a mathematical model that describes the potential energy of an atomic or molecular system as a function of atomic positions.

Force fields typically consist of empirical or semi-empirical functions that approximate interatomic interactions, including bonded and non-bonded terms. Bonded terms account for bond stretching (two-body interactions), angle bending

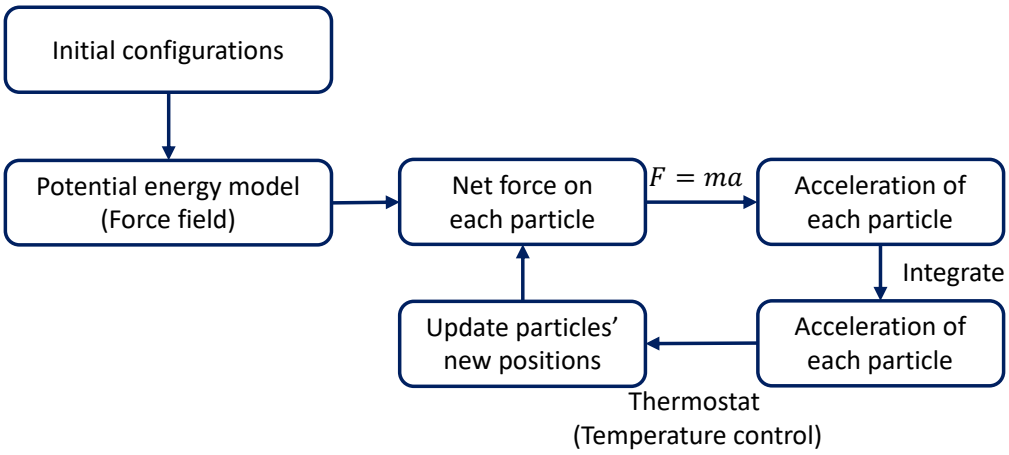


Figure 3.1: Schematic diagram of the MD simulation workflow.

(three-body interactions), and torsional rotation (four-body interactions), while non-bonded terms describe electrostatic and van der Waals interactions. The different contributions of atomic interactions are illustrated in Figure 3.2.

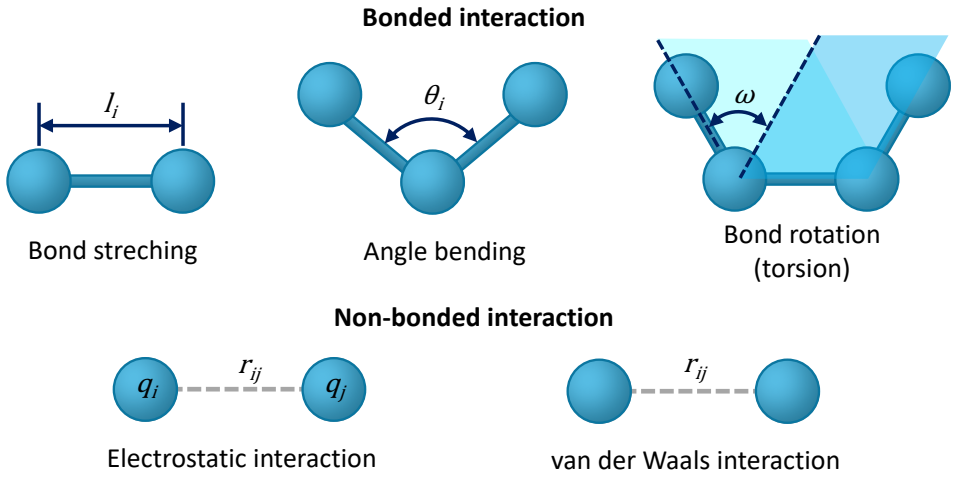


Figure 3.2: Schematic representation of four key interactions to molecular mechanics forcefield. Bonded terms include bond stretching (two-body interactions), angle bending (three-body interactions) and torsional rotation (four-body interactions), while non-bonded terms include electrostatic and van der Waals interactions.

Among various available force fields, the General AMBER Force Field (GAFF) is widely used for modeling small organic molecules. The GAFF was developed as an extension of the AMBER force field, which was originally designed for proteins

and nucleic acids, to allow consistent treatment of a broad range of organic and bio-organic molecules.[117,118] The GAFF takes a simple functional form, expressed as:

$$E(r^N) = \sum_{\text{bonds}} \frac{k_i}{2}\left(l_i - l_{i,0}\right)^2 + \sum_{\text{angles}} \frac{k_i}{2}\left(\theta_i - \theta_{i,0}\right)^2 + \sum_{\text{dihedrals}} \frac{V_n}{2}(1 + \cos(n\omega - \gamma)) + \sum_{i=1}^{N}\sum_{j>i}^{N}\left\{4\varepsilon_{ij}\left[\left(\frac{\sigma_{ij}}{r_{ij}}\right)^{12} - \left(\frac{\sigma_{ij}}{r_{ij}}\right)^{6}\right] + \frac{q_i q_j}{4\pi\varepsilon_0 r_{ij}}\right\} \tag{3.29}$$

where, $E(r^N)$ denotes the potential energy of the atomic system, which is expressed as a function of the positions of all particles; $l_{i,0}$ and $\theta_{i,0}$ represent the equilibrium bond lengths and bond angles, respectively; k_i , V_n are force constants; n is multiplicity and γ is the phase angle for the torsional rotation. ε_{ij}, σ_{ij} and q_i are the parameters characterize the non-bonded interactions.

- The first term in Eq. (3.29) describes the interactions between pairs of bonded atoms as a harmonic potential. According to Hooke's law, the energy varies with the square of the displacement from the reference bond length $l_{i,0}$.
- The second term accounts for all valence angles in the molecule, which is also models as harmonic oscillators around the equilibrium angle $\theta_{i,0}$.
- The third term represents the torsional energy associated with rotation around a bound, which is modeled as a periodic function depending on the torsional angle, its multiplicity n, and phase angle γ.
- The last term sorts up all non-bonded interactions, which are typically modeled using a Coulomb potential for electrostatic interactions and a Lennard-Jones potential for van der Waals interactions. Only the interactions between atoms in different molecules, or atoms belong to the same molecule but separated by at least three bonds, are considered as non-bonded contributions.

Electrostatic Interactions and Partial Atomic Charges

One of the most critical components that describe interactions between non-bonded atoms is electrostatic interactions. Because classical MD does not explicitly treat electrons, the electronic distribution around each atom is approximated using partial atomic charges, which reflect how electron density is distributed across the molecule. To represent this electrostatic potential in MD simulations, a common approach is to assign fractional point charges to the atoms within a molecule. These charges are fixed at the positions of atomic nuclei and referred to as partial atomic

charges.[119,120] The total electrostatic interaction energy (or Coulomb interaction energy) E_{Coul} is calculated as the sum of pairwise interactions among all point charges using Coulomb's law:

$$E = \sum_{i=1}^{N} \sum_{j>i}^{N} \frac{q_i q_j}{4\pi\varepsilon_0 r_{ij}} \tag{3.30}$$

where q_i and q_j represent the partial atomic charges on atoms i and j. r_{ij} is the distance between two atoms. ϵ_0 is the vacuum permittivity.

In GAFF, partial atomic charges are usually assigned using one of the following methods:

- RESP (Restrained ElectroStatic Potential) charges,[121] derived by fitting to quantum mechanically calculated electrostatic potentials, usually at the HF/6-31G* level.
- AM1-BCC (Bond Charge Correction) charges,[122–124] a faster alternative that starts from semi-empirical AM1 calculations and applies empirical corrections based on the bond types. This method is commonly used due to its efficiency and reasonable accuracy.

Lennard-Jones Potential

In addition, van der Waals interactions also play a crucial role in interactions between non-bonded atoms. These interactions arise from temporary charge fluctuations and unclude both attractive dispersion forces and short-range repulsive forces due to Pauli exclusion when electron clouds overlap. The Lennard–Jones potential is commonly used in MD simulations to model van der Waals interactions.[125–128] The interaction energy Eq. (3.31) between a pair of non-bonded atoms i and j is given by:

$$E = 4\varepsilon \left[\left(\frac{\sigma}{r}\right)^{12} - \left(\frac{\sigma}{r}\right)^{6} \right] \tag{3.31}$$

where r is the distance between two interacting atoms, ϵ is the depth of the potential well, and σ is the distance at which the potential energy across zero. The potential energy reaches a minimum of $-\epsilon$, when $r = 2^{1/6}\sigma \approx 1.122\sigma$.

Figure 3.3 illustrates Lennard–Jones potential energy of argon-argon interactions.[129] The repulsive r^{-12} term models the steep increase in energy when two atoms become very close together, while the attractive r^{-6} term captures dispersion forces at longer ranges.

The parameters ϵ_{ij} and σ_{ij} are typically defined for each atom type and combined using mixing rules. Lorentz–Berthelot rule is one of the most widely used

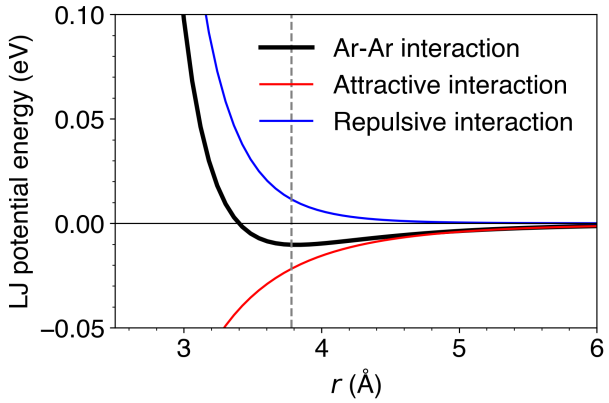


Figure 3.3: Lennard–Jones potential energy between a pair of Argon atoms.

rules.

$$\sigma_{ij} = \frac{\sigma_{ii} + \sigma_{jj}}{2} \tag{3.32}$$

$$\varepsilon_{ij} = \sqrt{\varepsilon_{ii}\varepsilon_{jj}} \tag{3.33}$$

where i and j refer to different atom types, $i \neq j$.

3.2.2 Numerical Integration: Verlet Algorithm

In MD simulations, once the forces acting on each atom are determined from the force field, the system's time evolution is computed by integrating Newton's equations of motion. Because analytical solutions are impractical for systems with large degrees of freedom, numerical integration methods are used to propagate atomic positions and velocities over small time steps.

All the algorithms for integrating the Newton's equations of motion assume that the position and its derivatives can be expanded by Taylor series.[116]

$$r(t+\delta t) = r(t) + \delta t v(t) + \frac{1}{2}\delta t^2 a(t) + \frac{1}{6}\delta t^3 b(t) + \frac{1}{24}\delta t^4 c(t) + \cdots \tag{3.34}$$

$$v(t+\delta t) = v(t) + \delta t a(t) + \frac{1}{2}\delta t^2 b(t) + \frac{1}{6}\delta t^3 c(t) + \cdots \tag{3.35}$$

$$a(t+\delta t) = a(t) + \delta t b(t) + \frac{1}{2}\delta t^2 c(t) + \cdots \tag{3.36}$$

Where v is the velocity, the first derivative of the positions with respect to time; a is the acceleration, the second derivative of the position; b and c are the third and fourth derivatives.

One of the most widely used numerical integration algorithms is Verlet algorithm.[130] This method relies on positions at the current and previous time steps, making it computationally efficient since it avoids explicit calculation of velocities. However, velocities can still be estimated if needed. It uses the current positions $r(t)$ and accelerations $a(t)$ at time t, and the positions from the previous step $r(t - \delta t)$, to calculate the new positions in the next step $t + \delta t$, $r(t - \delta t)$.

$$r(t + \delta t) = r(t) + \delta t v(t) + \frac{1}{2}\delta t^2 a(t) + \cdots \tag{3.37}$$

$$r(t - \delta t) = r(t) - \delta t v(t) + \frac{1}{2}\delta t^2 a(t) - \cdots \tag{3.38}$$

Adding Eq. (3.37) and Eq. (3.38) together gives

$$r(t + \delta t) = 2r(t) - r(t - \delta t) + \delta t^2 a(t) \tag{3.39}$$

3.2.3 Temperture Control: Thermostat

Most experimental conditions are conducted under controlled temperature and/or the pressure. To mimic this behavior in MD simulations, thermostats are employed to regulate the kinetic energy of particles and thereby control the system's temperature.[116]

Regarding the canonical ensemble (constant nvt) employed in MD simulations, the number of particles in the system(N) , the system's volume (V) and the temperature (T) are constant.[131] The temperature of the system is related to the time average of the kinetic energy $\langle E_{\text{kin}} \rangle$, which for an unconstrained system is expressed as:

$$\langle E_{\text{kin}} \rangle_{\text{nvt}} = \langle \sum_{i=1}^{N} \frac{1}{2} m_i v_i^2 \rangle = \frac{3}{2} N k_{\text{B}} T \tag{3.40}$$

where m_i and $v_i$represent the mass and the velocity of particle i, respectively. k_{B} is Boltzmann constant.

Although the system's temperature and the average kinetic energy are kept constant, the instantaneous kinetic energy fluctuates with the current velocities of the particles, and therefore, determines the instantaneous temperature.

$$k_{\text{B}} T(t) = \frac{2}{3N} E_{\text{kin}}(t) \tag{3.41}$$

To maintain the desired temperature, various thermostat algorithms have been developed. These methods can be broadly classified into three categories:

1. Velocity scaling method,[132] which alters the temperature by rescaling particle velocities at each time step. The scaling factor is determined by the ratio of the required temperature to the current one.

2. Stochastic collision method,[133] in which random collisions are introduced by occasionally altering the velocities of randomly selected particles. This is equivalent to coupling the system to a heat bath that randomly emits "thermal particles" to collide with atoms in the system.

3. Extended system method,[134,135] which introduces the energy fluctuations by extending the system's Lagrangian; that is, a Lagrangian containing additional, artificial coordinates and velocities.

Two different thermostat algorithms that are used in this work will be introduced in the following: Langevin thermostat (stochastic collisions method) and Nosé–Hoover thermostat (extended system method).

Langevin Thermostat

The Langevin thermostat[133,136] is a widely used method to control temperature in MD simulations.It assumes a group of atoms being embedded in a sea of small frictional particles and models interactions with this background implicit solvent.

The force on a particle is considered to arise from three sources: The first one (F_i) comes from the interactions between the particles, which depends upon the relative position of the particles, and is modeled by using a potential of mean force ϕ.

$$F_i = -\nabla\phi \tag{3.42}$$

The motion of the particle through the solvent contributes to the second component of forces which is equivalent to the frictional drag on the particle. The frictional force (F_f) is proportional to the speed of the particle with a constant friction coefficient:

$$F_f = -\xi v \tag{3.43}$$

where v is the velocity and ξ is the friction coefficient. The friction coefficient is related to the collision frequency (γ) by

$$\gamma = \frac{\xi}{m} \tag{3.44}$$

that γ^{-1} can be considered as the time taken for the particle to lose memory of its initial velocity (damping time). For a spherical particle the friction coefficient is

related to the diffusion constant D by:

$$\xi = \frac{k_{\mathrm{B}}T}{D} \tag{3.45}$$

The last force component (F_r) is due to the solvent atoms randomly bumping on the particle at temperature T. It can be represented as

$$F_r = \sigma\xi \tag{3.46}$$

The coefficient σ governs the strength of the random force. It is related to γ via fluctuation-dissipation theorem:

$$\sigma = \sqrt{2\xi k_{\mathrm{B}}T} = \sqrt{2\gamma m k_{\mathrm{B}}T} \tag{3.47}$$

The Langevin equation of motion for a particle can therefore be written as

$$\dot{p} = -\nabla\phi - \xi v + \sigma\xi = -\nabla\phi - \gamma p + \sigma\xi \tag{3.48}$$

Nosé–Hoover Thermostat

The Nosé–Hoover thermostat[116,134,135] is a deterministic method used in MD simulations to maintain a system at a constant temperature. Unlike stochastic methods such as Langevin thermostat, Nosé–Hoover thermostat implement a thermal reservoir as an extra coordinate to the system.

To perform MD simulations subject to a constant temperature, the reservoir is introduced into the system and represented by an additional degree of freedom, labeled s. A series of virtual variables (coordinates r, momenta p, and time t) is also introduced to describe the system. They follow the relation to the real counterparts (r', p', t'):

$$r' = r \tag{3.49}$$

$$p' = \frac{p}{s} \tag{3.50}$$

$$s' = s \tag{3.51}$$

$$dt' = \frac{dt}{s} \tag{3.52}$$

The Lagrangian for the extended system is constructed as

$$\mathcal{L}_{\mathrm{Nose}} = \sum_{i=1}^{N} \frac{m_i s^2 \dot{r}_i^2}{2} - \mathcal{U}(r) + \frac{Q\dot{s}^2}{2} - g k_{\mathrm{B}}T \ln s \tag{3.53}$$

where Q is an effective mass associated to s.

The momenta conjugate to r_i and s can be derived as

$$p_i \equiv \frac{\partial \mathcal{L}}{\partial \dot{r}_i} = m_i s^2 \dot{r}_i \tag{3.54}$$

$$p_s \equiv \frac{\partial \mathcal{L}}{\partial \dot{s}} = Q\dot{s} \tag{3.55}$$

This gives the Hamiltonian of the extended system of the N particles and additional variable s:

$$\mathcal{H}_{\text{Nose}} = \sum_{i=1}^{N} \frac{p_i^2}{2m_i s^2} + \mathcal{U}(r) + \frac{p_s^2}{2Q} + g k_{\text{B}} T \ln s \tag{3.56}$$

According to Eq. (3.56), one can define the equations of motion using the virtual variables introduced to the extended syste.

$$\frac{dr_i}{dt} = \frac{\partial \mathcal{H}_{\text{Nose}}}{\partial p_i} = \frac{p_i}{m_i s^2} \tag{3.57}$$

$$\frac{dp_i}{dt} = -\frac{\partial \mathcal{H}_{\text{Nose}}}{\partial r_i} = -\frac{\partial \mathcal{U}(r)}{\partial r_i} \tag{3.58}$$

$$\frac{ds}{dt} = \frac{\partial \mathcal{H}_{\text{Nose}}}{\partial p_s} = \frac{p_s}{Q} \tag{3.59}$$

$$\frac{dp_s}{dt} = -\frac{\partial \mathcal{H}_{\text{Nose}}}{\partial s} = \frac{\left(\sum_{i=1}^{N} \frac{p_i^2}{m_i s^2} - g k_{\text{B}} T\right)}{s} \tag{3.60}$$

These equations of motion can also be written in terms of the real variables as

$$\frac{dr_i'}{dt} = s\frac{dr_i}{dt} = \frac{p_i}{m_i s} = \frac{p_i'}{m_i} \tag{3.61}$$

$$\frac{dp_i'}{dt} = s\frac{\frac{dp_i}{s}}{dt} = \frac{dp_i}{dt} - \frac{1}{s}p_i\frac{ds}{dt} = -\frac{\partial \mathcal{U}(r')}{\partial r_i'} - \frac{s'p_s'}{Q}p_i' \tag{3.62}$$

$$\frac{1}{s}\frac{ds'}{dt} = \frac{ds}{dt} = \frac{s'p_s'}{Q} \tag{3.63}$$

$$\frac{d\left(\frac{s'p_s'}{Q}\right)}{dt} = \frac{s}{Q}\frac{dp_s}{dt} = \frac{1}{Q}\left(\sum_{i=1}^{N} \frac{{p_i'}^2}{m_i} - g k_B T\right) \tag{3.64}$$

The equations of motions for the extended system can be further simplified by introducing the thermodynamic friction coefficient $\xi = s'p'_s/Q$, and are expressed in real variables as follows: (Here, r, p, and t denote real variables)

$$\dot{r}_i = \frac{p_i}{m_i} \tag{3.65}$$

$$\dot{p}_i = -\frac{\partial \mathcal{U}(r)}{\partial r_i} - \xi p_i \tag{3.66}$$

$$\dot{\xi} = \frac{1}{Q}\left(\sum_{i=1}^{N} \frac{p_i^2}{m_i} - g k_{\mathrm{B}} T\right) \tag{3.67}$$

$$\frac{\dot{s}}{s} = \frac{d \ln s}{dt} = \xi \tag{3.68}$$

For the extended system, the Newton's second law can be replaced by

$$\ddot{r_\iota} = \frac{F_i}{m_i} - \xi \dot{r_\iota} \tag{3.69}$$

3.3 Scanning Tunneling Microscopy

The Scanning Tunneling Microscopy (STM) was invented in 1981 by Gerd Binnig and Heinrich Rohrer. It is a type of scanning probe microscope used for imaging surfaces at the atomic scale. When a conductive tip is brought extremely close (a few angstroms) to a conductive or semi-conductive surface, and a bias voltage is applied between them, electrons can tunnel through the vacuum gap separating the tip and the surface, which does not require physical contact. In constant-current mode, the tunneling current is continuously monitored as the tip scans across the surface, and is used to adjust the tip height to keep the current constant. The vertical movement of the tip is recorded to create a topographic map of the surface at atomic resolution.

The following introduction to the basic concept of quantum tunneling is adapted from ref[57]. For a simple one-dimensional model, consider a rectangular potential barrier of height $U(z)$ and an electron of mass m with energy E. The electron's state is described by a wavefunction $\psi(z)$, which satisfies the time-independent Schrodinger's equation,

$$-\frac{\hbar^2}{2m}\frac{d^2}{dz^2}\psi(z) + U(z)\psi(z) = E\psi(z) \tag{3.70}$$

In barrier region, where $E < U(z)$, Eq. (3.70) has solutions

$$\psi(z) = \psi(0)e^{-\kappa z}, \quad \psi(z) = \psi(0)e^{\kappa z} \tag{3.71}$$

where

$$\kappa = \frac{\sqrt{2m\,(U-E)}}{\hbar} \tag{3.72}$$

is the decay constant. It describes a state of the electron decaying in the $+z$ or $-z$ direction within the classically forbidden region. The probability density of finding an electron at a point z is proportional to $\kappa = \frac{\sqrt{2m(U-E)}}{\hbar}$, which has a nonzero value in the barrier, and therefore, there is a nonzero probability for the electron to penetrate and tunnel through the barrier.

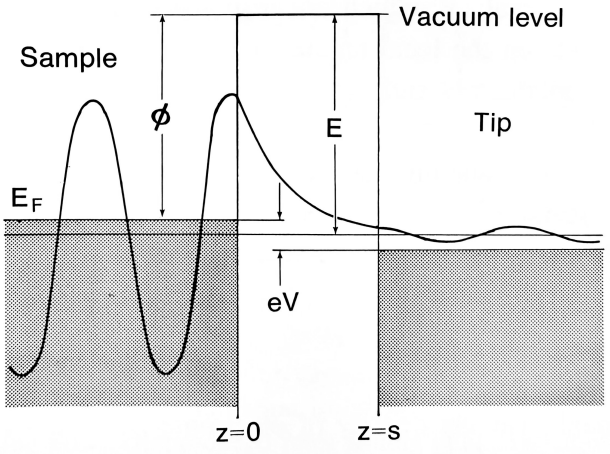


Figure 3.4: One-dimensional metal–vacuum–metal tunneling junction.[57]

Figure 3.4 illustrates tunneling process across a metal–vacuum–metal junction under simplified STM condition. It is assumed that the tip and the sample have the same work function, ϕ. Taking the vacuum level as the energy reference , the Fermi level is located at $E_F = -\phi$. When a bias voltage V is applied, a tunneling current is generated between the vacuum gap, allowing electrons to tunnel from the sample into the tip and vice visa.

A sample state ψ_n with energy level E_n lying within the energy window between $E_F - eV$ and E_F has a chance to tunnel into the tip. Assuming the applied bias is much smaller than the work function $eV \leq \phi$, the energy level of the sample states of interest are very close to the Fermi level E_F. Under this condition, the probability w for an electron in the *n*th sample state is present at the tip position $z = W$, is given by:

$$w \propto \mid \psi_n(0) \mid^2 e^{-2\kappa W} \tag{3.73}$$

where $\psi_n(0)$ is the *n*th sample state at the sample surface, and

$$\kappa = \frac{\sqrt{2m\phi}}{\hbar} \tag{3.74}$$

is the decay constant of a sample state near the Fermi level in the barrier region.

During an STM scan, the tip condition usually remains stable. The electrons coming to the tip surface, located at $z = s$, have a constant velocity to flow into the tip. The tunneling current is therefore directly proportional to the number of states in the sample that are available within the energy window eV. By including all sample states with energies between $E_F - eV$ and eV, the tunneling current can be expressed as:

$$I \propto \sum_{E_n=E_F-eV}^{E_F} |\psi_n(0)|^2 e^{-2\kappa W} \tag{3.75}$$

If the bias voltage V is small enough so that the density of electronic states does not vary significantly within the energy interval, the sum in Eq. (3.75) can be approximated using the local density of states (LDOS) at the Fermi level. The LDOS, $\rho_s(z, E)$, of the sample at position z and energy E, is defined as

$$\rho_S(z, E) \equiv \frac{1}{\epsilon} \sum_{E_n=E-\epsilon}^{E} |\psi_n(z)|^2 \tag{3.76}$$

for a sufficiently small energy interval ϵ.

Therefore, the tunneling current can be be written in terms of the LDOS of the sample:

$$\begin{aligned} I &\propto V\rho_S(0, E_F)e^{-2\kappa W} \\ &\approx V\rho_S\left(0, E_F\right)e^{-1.025\sqrt{\phi}W}. \end{aligned} \tag{3.77}$$

For typical work function values around $\phi \approx 4$ eV, the decay constant $\kappa \approx 1$ Å^{-1}. This exponential dependence of the tunneling current on the tip–sample distance allows STM to detect atomic-scale height differences on the surface.

Chapter 4

Chiral Recognition Mechanism of Two-Dimensional Self-Assembly Formed by [7]Thiaheterohelicene

The main results presented in this chapter have been published in the following paper.

Changqing Ye, Takuma Hattori, Yuji Hamamoto, Pawel Krukowski, Kouji Inagaki, Akira Saito, Hideji Osuga, Yoshitada Morikawa, and Yuji Kuwahara, "Chiral Recognition Mechanism of Two-Dimensional Self-Assembly Formed by [7]Thiaheterohelicene." *J. Phys. Chem. C* **2023**, *127*, 21305–21312.

4.1 Introduction

Chiral recognition on solid surfaces is a fundamental phenomenon in surface science, where chiral molecules interact with one another or with a chiral environment to form enantioselective or enantiospecific assemblies. These interactions are often governed by a delicate balance between molecule–molecule and molecule–substrate interactions, and can give rise to highly ordered two-dimensional supramolecular structures.

Recently, Krukowski *et al.* conducted an STM investigation on [7]thiaheterohelicene ([7]TH) on Ag(111) and found that the molecule self-assembled into well-ordered zigzag chains at the surface coverage approaching a saturated monolayer.[72] These chains represent a highly ordered two-dimensional chiral structure, highlighting the unique behavior of the molecules in low-dimensional systems. Due to the high mobility of helicenes on metal surfaces, individual molecules or small aggregates cannot be observed by STM, even at a temperature as low as 60 K.[137] Moreover, for helicenes with more than five rings, it becomes difficult to distin-

guish the chirality for each enantiomer in STM images because of steric effect of the molecules and limited spatial resolution of STM (Figure 4.1). As a result, experimental observation of the early-stage assembly of such molecules remains a significant challenge.

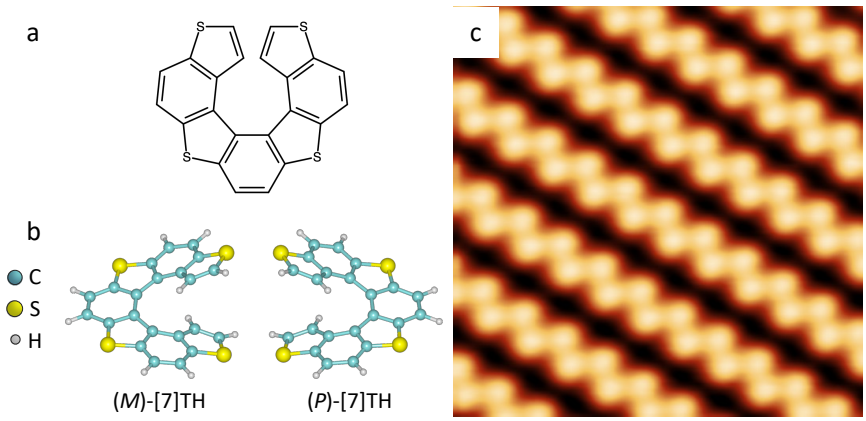


Figure 4.1: (a) Structure, and (b) ball-and-stick models of [7]TH. (c) Ordered structures of *rac*-[7]TH on Ag(111).

To better understand the chiral recognition mechanism of thiaheterohelicene, it is essential to trace the process at the initial stage: how the molecules start to assemble into certain ordered structures among a small number of molecules. his chapter presents a theoretical investigation of the growth process from isolated molecules to long-range self-assembled structures of *rac*-[7]TH on Ag(111) using DFT calculations and MD simulations. By tracing the time evolution of molecular configurations, the results reveal that *rac*-[7]TH molecules preferentially form heterochiral dimers, which subsequently develop into extended zigzag chains. This growth behavior is driven by intermolecular interactions arising from the steric characteristics of the helical molecular skeleton.

4.2 Methods

This section outlines the computational details for DFT calculations and MD simulations, including the calculation parameters, and procedural steps used in this study.

4.2.1 Computational Details of DFT Calculations

DFT calculations were performed using the STATE code[138–140] with norm-conserving pseudopotentials.[141] The wave functions and charge densities were expanded in a

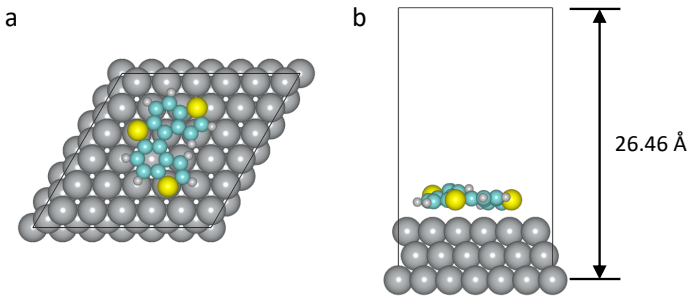


Figure 4.2: (a) Top, and (b) side view of unit cell used for [7]TH on Ag(111).

plane-wave basis set with cutoff energies of 64 Ry and 400 Ry, respectively. Dispersion forces were included using the self-consistent[142–144] van der Waals density functional method,[145] especially employing the rev-vdW-DF2 functional.[146,147]

Gas-phase structure optimizations were carried out using a periodic cubic unit cell of 26.5×26.5×26.5 Å^3, with Brillouin zone sampling restricted to the Γ point. To investigate molecule adsorption, the Ag(111) surface was modeled using a 6×6 unit cell with a calculated lattice constant of 4.09 Å (Figure 4.2a). A 4×4×1 k-point mesh was used to sample the Brillouin zone. The surface was represented using a slab model consisting of three atomic layer, with the bottom-most layer fixed to its bulk geometry. To eliminate nonphysical interactions between periodic images, a vacuum gap of $\simeq$ 22 Å was added perpendicular to the slab surface (Figure 4.2b). During all calculations, the convergence threshold for the total energy was set to 2.72×10^{-8} eV, and a gradient threshold of 5.14×10^{-2} eV/Å was used for geometry optimization.

The interaction energy of a molecule on the surface was calculated using the follwoing expression:

$$E_{\text{int}} = E_{\text{molecue/surface}} - E_{\text{molecule}} - E_{\text{surface}} \tag{4.1}$$

where $E_{\text{molecue/surface}}$, E_{molecule}, and E_{surface} represent the total energies of the adsorption system, isolated molecule, and surface, respectively.

4.2.2 Computational Details of MD Simulations

Data File Generation

The data files containing the system topology, partial atomic charges, and force field parameters were generated using Winmostar.

- **Molecular system construction**

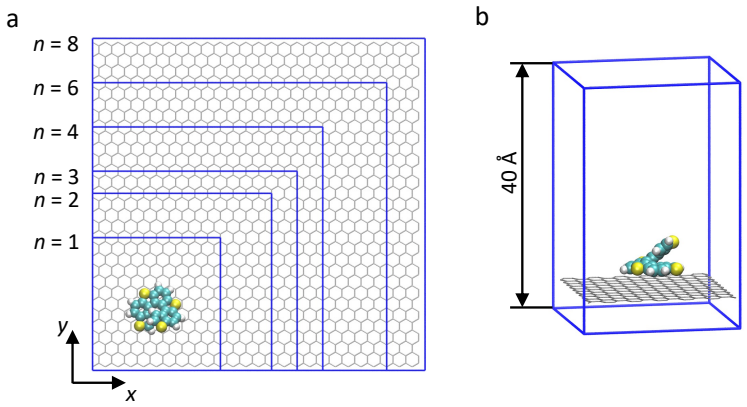


Figure 4.3: (a) Different lateral dimensions (*xy*-plane) of the unit cell that which corresponds to the change in the number of molecules. (b) The perpendicular dimension (*z*-direction) of the unit cell.

Table 4.1: Different unit cells as the number of molecules changes.

n	1	2	3	4	6	8
x-length (Å)	24.56	30.03	39.30	44.21	56.48	63.86
y-length (Å)	25.52	34.03	38.29	46.79	55.30	63.81
ρ (molecule/nm^2)	0.16	0.17	0.20	0.19	0.19	0.20

For the single-molecule adsorption simulations, the unit cell dimensions were set to 24.56 Å×25.52 Å×40.00 Å along the x, y, and z directions, respectively. (Figure 4.3a) A monolayer graphene sheet with a lattice constant of 2.456 Å was used as substrate, which was set parallel to the xy-plane at z = 5.00 Å. The molecular structure of a free molecule ([7]TH in this case) was taken from the optimized geometry obtained via DFT calculations. The molecule was randomly placed above the graphene surface, with its geometric center located z = 15.00 Å, corresponding to a vertical distance of approximately 10.00 Å away from the surface.

For the molecular migration simulations, in order to investigate the migration behavior of molecules at a low surface coverage, unit cells of different lateral dimensions (*xy*-plane) were used with respect to the number of molecules in the system while keeping the number density of molecules constant ($\simeq$0.2 molecule/nm^2, see Table 4.1). The perpendicular dimension of unit cell (*z*-direction) was 40.00 Å (Figure 4.3(b)). For example, in the case of n = 2, the three dimensions of the unit cell were x = 34.38 Å, y = 34.03 Å, z = 40.00 Å. The graphene sheet was placed parallel to the xy-plane and fixed

at z = 5.00 Å. The molecular geometry was obtained from DFT calculations of a free molecule. Each molecule was placed in an adsorbed configuration, whose structure was tilted to make its second ring lay parallel to the surface. The geometric center of each molecule was positioned at z = 10.00 Å, and therefore, the molecule was approximately 5.00 Å above the graphene substrate.

- **Partial atomic charge assignment**

  The partial atomic charges of the molecule were generated using the AM1-BCC method. The total charge of each molecule was set to be zero to ensure neutrality. For the graphene substrate, the partial charges of all carbon atoms were manually assigned to zero.

- **Force field parameter assignment**

  The general AMBER force field (GAFF) was chosen as the potential model to describe the interactions between atoms in the system. GAFF is designed to be compatible with existing AMBER force field for proteins and nucleic acids and includes parameters for a wide range of organic molecules composed of elements such as H, C, N, O, S, P, and halogens. However, it is not suitable for directly modeling the interactions including metal atoms such as Ag. Force field parameters were assigned using the ACPYPE utility, as implemented in Winmostar.

Simulation Setups

The MD simulations were performed using LAMMPS.[148] The interactions among the atoms were modeled using the general Amber force field (GAFF).[117,118] A cutoff of 12 Å was applied for non-bonded interactions. For interactions between two dissimilar atom type, the Lorentz-Berthelot rule was ued to adjust Lennard–Jones potential parameters. The pairwise neighbor list was updated every timestep with a cutoff distance of 14 Å. To reduce computational cost, C atoms in the graphene were excluded from each other's pairwise neighbor list. These C atoms were fixed at z = 5 Å throughout the simulations.

Periodic boundary conditions were applied in all directions. Long-range electrostatic interactions were computed in reciprocal space using the particle-particle particle-mesh (PPPM) solver. An extra modification in k-space solver was further applied to extend in the z-direction three times compared to the original one and turn off slab-slab interactions, therefore, avoiding artificial electrostatic interactions between periodic images.

The simulation workflow was divided into two main procedures: preparation process and production MD simulations, consisting of the following steps

(Figure 4.4):

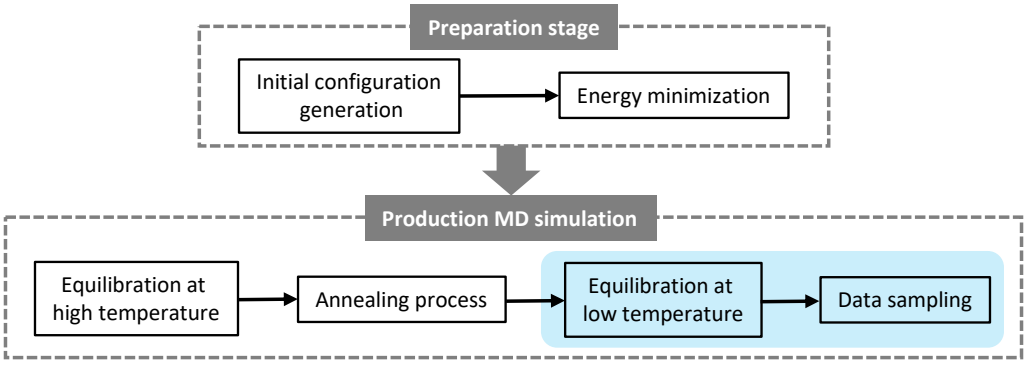


Figure 4.4: MD simulation process.

The preparation process was set to generate multiple random-distributed initial molecular configurations to avoid biased molecular arrangements.

- **Initial configuration generation**

  To generate multiple independent random configurations of the molecules from the data files prepared using Winmostar, the system was first simulated at a high temperature of 1000 K, which promotes molecular diffusion. The MD simulations were performed in *nvt* ensemble at a constant tempertature of 1000 K, employing the Nosé–Hoover thermostat for temperature control and Verlet integration for time evolution.

  The system's atomic coordinates were recorded every 1000 timesteps for single-molecule adsorption simulations, and 10000 timesteps for molecular migration simulations. After each sampling interval, a new data file containing updated atomic coordinates was generated.

  During this process, a spatial constraint, referred as the "one-way zone", was set during the simulations to confine atomic motion within a specific region of the unit cell. When an atom enters the one-way zone, its velocity component will be reverse if it has a wrong sign in the specified dimension. This setup was intended to prevent the atoms going out of the original unit cell, for example, like being adsorbed on the backside of the graphene sheet, or going far from the substrate where adsorption would not be physically meaningful.

  In the case of single-molecule adsorption simulations, atoms located above z = 25 Å had their z-component of velocity flipped downward ($-v_z$), while those below z = 10 Å were redirected upward ($+v_z$), as shown in Figure 4.5a. In the case of molecular migration simulations, atoms enter the region higher

than z = 15 Å would have the sign of the z-component of their velocities inverted to avoid unexpected upward moving ($-v_z$), as illustrated in Figure 4.5b. Additionally, the z-component of the net force acting on each molecule was set to zero, which further constrained the two-dimensional movements for the molecules.

- **Energy minimization**

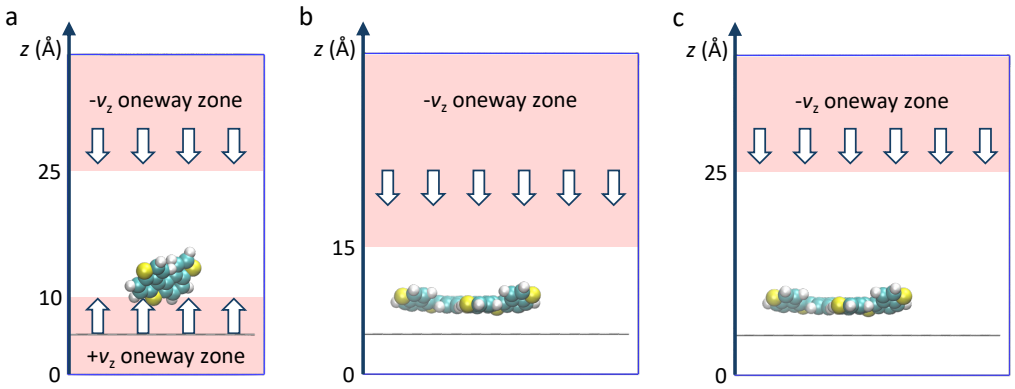


Figure 4.5: Constrained unit cells for (a) single-molecule adsorption simulations and (b) molecular migration simulations (two molecules in this case). The pink regions represent the one-way zones.

An energy minimization was performed to eliminate any unphysical net forces acting on the atoms. This was followed by a short low-temperature MD simulations to further relax the system. The simulations were run for 10000 timesteps with a timestep was of 0.1 fs, therefore, 1 ps for total simulation time. The temperature was maintained at 1 K using the Langiven thermostat.

In the production process, MD simulations were carried out under temperature-controlled conditions to investigate time evolution of molecular behavior and thermodynamic properties (temperature, kinetic energy, potential energy, *etc.*) of the system. The simulations were conducted in the *nvt* ensemble where a Nosé–Hoover thermostat[116,134,135] was applied to maintain the system temperature, as illustrate in Figure 4.6. The time step of 1 fs was used during each simulation run. In this study, the system was first equilibrated at 275 K for 5000000 timesteps (equivalent to 5 ns), then cool from 275 K to 80 K within 2000000 timesteps (2 ns), finally was equilibrated at 80 K for 600000 timesteps (0.6 ns). Atomic coordinates were recorded every 1000 timesteps (1 ps), while thermodynamic properties were output every 100 timesteps (100 fs). Note that, to ensure that molecules remained within

the unit cell, a one-way zone was defined at z>15 Å, where atoms with $+v_z$ had their velocity flipped to $-v_z$, as shown in Figure 4.5c.

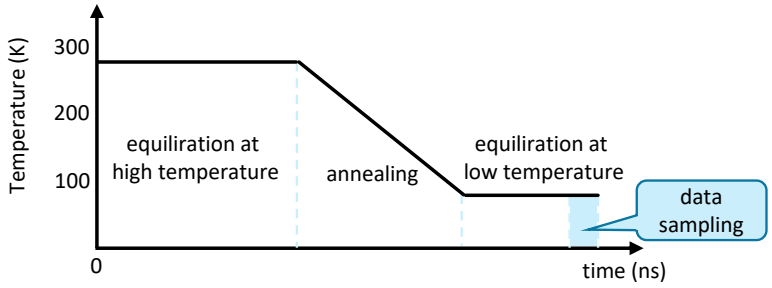


Figure 4.6: The simulation process with temperature control.

- **Equilibration at high temperature:** The initial atomic velocities were randomly assigned according to a Gaussian distribution. The system was then equilibrated at 275 K to maintain a constant temperature and allow the molecules to migrate on the surface.
- **Annealing process:** The system was gradually cooled from high temperature (275 K) to a lower temperature (80 K), mimicking a thermal annealing process. This procedure allowed the system to evolve toward a more stable configuration.
- **Equilibration at low temperature and data sampling:** Following equilibration at 80 K for 0.5 ns, the system was considered reaching thermal equilibrium. The structural and dynamic properties from the final 100 fs of the simulations were used for further analysis.

The interaction energy between an individual adsorbate and the surface is defined as

$$E_{\text{int}} = (E_{\text{mol/sur}} - nE_{\text{mol}} - E_{\text{sur}})/n \tag{4.2}$$

where $E_{\text{mol/sur}}$, E_{mol}, and E_{sur} respectively represent the potential energies of the adsorption system, isolated molecule, and isolated clean surface; *n* is the number of molecules included in the adsorption system.

4.3 Adsorption Geometry of [7]TH on Ag(111)

As shown in the STM in Figure 4.1b, each circular protrusion was considered as a single [7]TH molecule. Based on this observation, a plausible model for the molec-

ular arrangement was proposed in a previous study,[72] in which the molecule is adsorbed with one of its terminals lying parallel on the surface. To determine the adsorption geometry of a single [7]TH on Ag(111), the molecule was initially set with its second benzene ring (ring B; see Figure 4.7a) lying parallel to the surface plane.

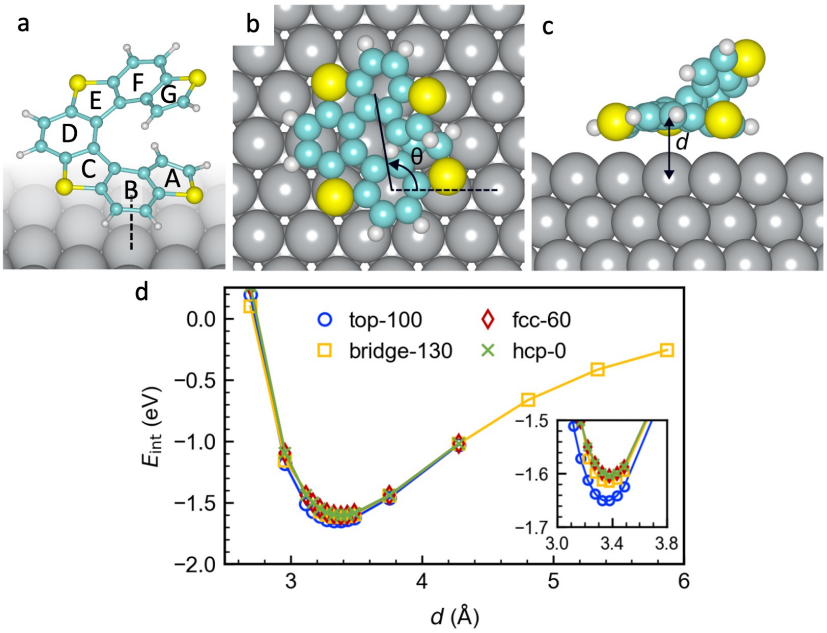


Figure 4.7: (a) Aromatic rings consisting of [7]TH, the order from A–G denotes the molecular skeleton angularly spiraling upward. (b) Top and (c) side views of adsorption geometry of [7]TH on the top site. (d) E_{int} of a single [7]TH on Ag(111) as a function of the distance d on the top-100, bridge-130, fcc-60, and hcp-0 sites.

The azimuthal angle θ and the distance d, as defined in Figure 4.7b, c, were varied in the calculations: The angle θ represents the in-plane rotation angle of the molecule, which is between the black line (molecular orientation) and the dashed line (close-packed direction of the Ag(111) surface). The parameter d represents the distance between the geometric center of ring B proximal to the surface and the topmost layer of the Ag(111) surface. The interaction energy,E_{int}, between the molecule and the surface was estimated as the number of molecules n = 1. The registry of the adsorbate was defined using the molecular position, which was represented by the center of ring B and the azimuthal angle of [7]TH on the surface; *i.e.*, the "top-100" site means that the molecule locates on the top site and rotates 100° from the close-packed direction of the (111) surface (Figure 4.7b).

The adsorption structure of [7]TH was explored on the top, bridge, fcc hollow, and hcp hollow sites of the Ag(111) surface with various molecular orientations.

Figure 4.7d shows the E_{int} of a single [7]TH on Ag(111) as a function of d when the molecule was on the four most stable adsorption geometries (the top-100, bridge-130, fcc-60, and hcp-0 sites) with fixed structures. The energy difference among the four geometries was extremely small with a deviation of the interaction energy of about 50 meV (the inset in Figure 4.7d). Consequently, the top-100 site was predicted as the most stable site for the [7]TH adsorbate on Ag(111), and the energy minimum was found to be around d = 3.4 Å by the cubic-spline interpolation. The geometries of the molecule and surface were then allowed to relax when the molecule was at the equilibrated distance on the top-100 site. The adsorption energy was estimated to be –1.83 eV, which indicated the energy difference of the adsorption system relative to the free-standing molecule and the clean surface.

Note that this value is similar to that of [7]CH on Ag(111) (–1.77 eV) estimated using the DFT-D method with the Grimme two-body potential reported by Tuca and Paci.[76] Our calculations showed that [7]TH was adsorbed with the first three (or four) rings in the lower terminal lying almost parallel to the surface and arranged in a convex configuration in which two thiophene rings slightly bent toward the surface. A similar adsorption geometry of [7]CH was reported by Fasel *et al.* based on an X-ray photoelectron diffraction experiment.[149]

The vertical distances from the surface of the first three rings were 3.2 Å for ring A, 3.4 Å for ring B, and 3.3 Å for ring C, whereas that for ring D had a similar value of 3.2 Å, indicating that not only the first three rings in the [7]TH backbone but also the fourth ring plays an important role in the interactions with the Ag(111) surface. Notably, the smallest distance between the S atom in ring C and the surface was about 3.1 Å, which suggests no strong S–Ag interactions during adsorption.[150]

Therefore, [7]TH was considered to be bound to the Ag surface via physisorption. This result was in good agreement with our previous X-ray photoelectron spectroscopy (XPS) investigation of [5]TH on Ag(111), where [5]TH was found to be physisorbed on Ag(111), and no obvious chemical shift in S 2p peaks was observed.[72]

4.4 Formation Mechanism of Chain Structures

To elucidate the formation mechanism of well-ordered structures of [7]TH, MD simulations were performed to evaluate the molecule–molecule interactions among [7]TH enantiomers on the surface. The DFT calculations indicate that [7]TH is weakly physisorbed on Ag(111), which suggests that intermolecular interactions play a crucial role in driving the formation of well-ordered structures.

In the MD simulations, the Ag(111) surface was replaced by a monolayer of graphene to simplify molecule–surface interactions. Graphene provides a flat substrate that enables two-dimensional surface diffusion of the molecules while signif-

icantly reducing computational complexity. Note that graphene has no site dependence for the adsorption of [7]TH molecules, as described later.

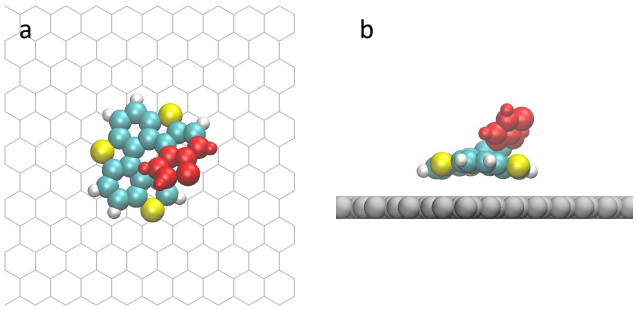


Figure 4.8: (a) Top and (b) side views of a single [7]TH adsorption on graphene.

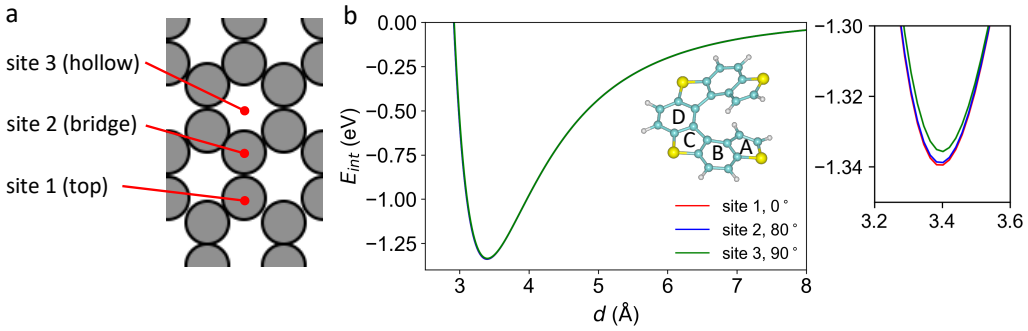


Figure 4.9: Site dependence of [7]TH adsorption on graphene. (a) Three different surface sites of graphene, sites 1, 2, and 3 are the top, bridge, and hollow sites, respectively. (b) Interaction energy profiles of [7]TH on graphene for three most stable adsorption structures. The center of ring B is on the surface sites shown in (a) and the azimuthal angle are 0, 80°, and 90°, respectively.

When a single [7]TH molecule was adsorbed on the graphene, the molecule had a geometry similar to that obtained by the DFT calculations, where the skeleton proximal to the surface is slightly convex to the surface plane (Figure 4.8). The adsorption energy on graphene was estimated to be –1.10 eV, and d was about 3.4 Å. Note that there was no apparent site preference of adsorption found in the simulations, suggesting a flat potential energy surface of the graphene for [7]TH adsorption. As shown in Figure 4.9, interaction energies calculated using the Lennard–Jones potential between [7]TH and graphene reveal that the energy difference between top and hollow adsorption sites is less than 5 meV, which is negligible compared to the value of adsorption energy (–1.10 eV).

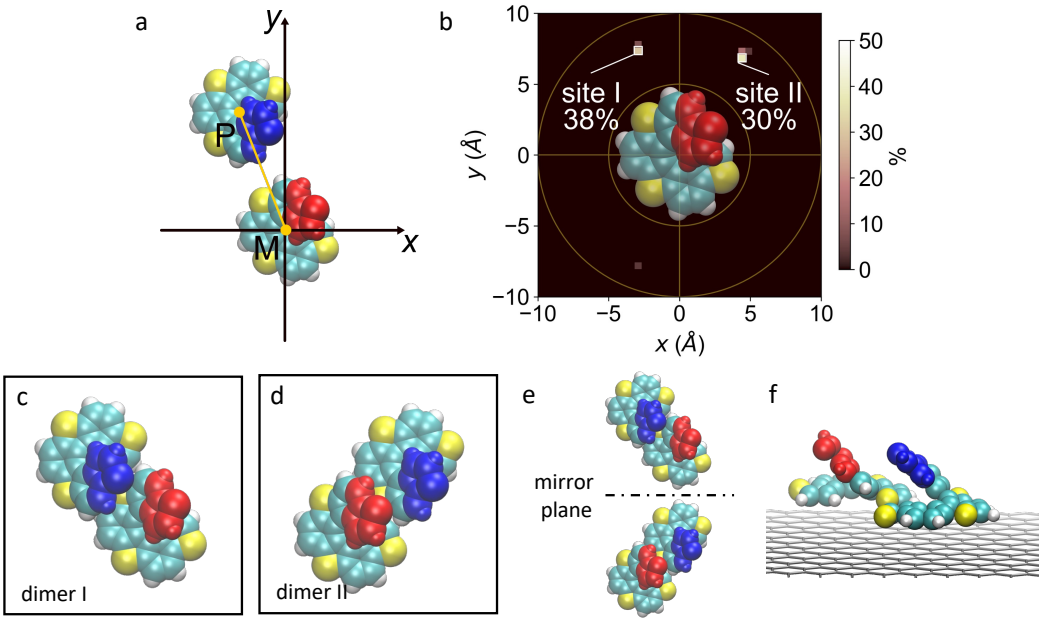


Figure 4.10: (a) Coordinate describing the molecular arrangement of the two different [7]TH enantiomers. (b)Probability distribution of the position of (*P*)-type molecule relative to (*M*)-type one. (c), (d) Most stable configurations of heterochiral dimers from top view (dimers I and II). (e) Mirror image of two heterochiral dimers. (f) Side view of the heterochiral dimer with "back-on-back" configuration.

Next, two different [7]TH enantiomers ($n = 2$, one (*M*)-type molecule and one (*P*)-type molecule) on the graphene were located on the surface. Individual monomers tended to form a heterochiral dimer from the initial configurations. To analyze this behavior, the relative positions of the geometric centers of the two enantiomers were tracked, as illustrated in Figure 4.10a. The zero point is at the geometric center of the (*M*)-type molecule, and the *x*-axis aligns parallel to the azimuthal orientation of the (*M*)-type molecule. The geometric center of the (*P*)-type molecule represents its molecular position. Figure 4.10b shows the probability distribution of the position of the (*P*)-type molecule relative to that of the (*M*)-type one among 50 randomly distributed initial configurations. The brighter pixels represent the higher probabilities of the (*P*)-type molecular position, which appeared around two regions close to the spiral-up skeleton of the (*M*)-type molecule.

In particular, they localized at two specific sites with the highest probabilities: sites I and II with 38% and 30%, respectively. The corresponding molecular arrangements (dimers I and II) are shown in Figure 4.10c, d. Interestingly, dimers I and II appeared as mirror images of each other Figure 4.10e. In both configurations, the spiral-up segments of the two enantiomers are closely aligned in a

so-called "back-on-back" arrangement. The in-plane intermolecular distance was about 8.6 Å, indicating that the two molecules bind to each other, as the planes of the molecules are almost flat. Owing to the steric effect, the spiral-up skeletons of two different enantiomers partially overlapped (Figure 4.10f), as the aromatic rings arranged in a configuration resembling the parallel-displaced benzene dimers,[151,152] and the distance between the nearest adjacent aromatic rings was about 4.6 Å. Dimers I and II were identified as the most stable configurations for a heterochiral dimer with an identical E_{int} of –1.22 eV. These dimers were formed through π–π interactions between the partially overlapped skeletons of different [7]TH enantiomers.

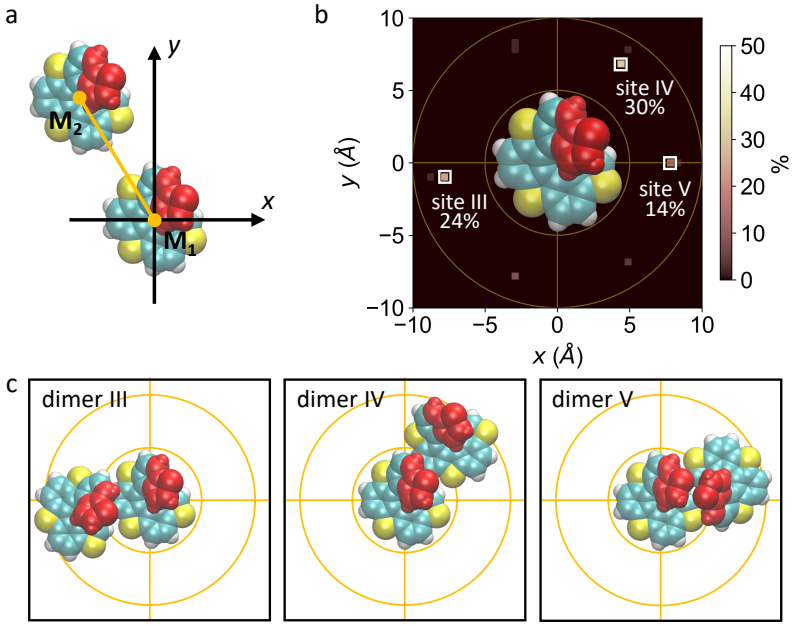


Figure 4.11: (a) Coordinate describing the molecular arrangement of the two same [7]TH enantiomers. (b)Probability distribution of the position of the second (*M*)-type molecule relative to the first (*M*)-type one. (c) Stable configurations of homochiral dimers in top view.

In contrast to the limited binding sites between different enantiomers, there were more sites available for same enantiomers to bind with each other (Figure 4.11a, b), which suggested lower kinetic energy barrier for two same enantiomers to change their arrangements. On the other hand, steric hindrance between the helical structures of same enantiomers prevented them from forming the same configuration as that of different enantiomers, as shown in Figure 4.11c. The E_{int} of three homochiral dimers are –1.20 eV for dimer III, –1.20 eV for dimer IV and –1.18 eV for dimer V. The dimers III, and IV demonstrate the same configuration but different

in the referencing molecule. The E_{int} of the most stable dimers found in the simulations was estimated to be –1.20 eV with a probability of 54%, which indicates that dimer formation is more preferred in a pair of different enantiomers (20 meV) than in identical enantiomers. Regarding the most stable configuration of homochiral dimer, two upper terminals of the molecules were not close, instead, one upper terminal approached to the lower terminal of the other enantiomer.

Additionally, the probabilities of finding both heterochiral (68%) and homochiral (44%) dimers had no significant change at a higher temperature of 275 K, which suggests that a change in temperature which is related to an entropic effect has little contribution to the dimer formation.

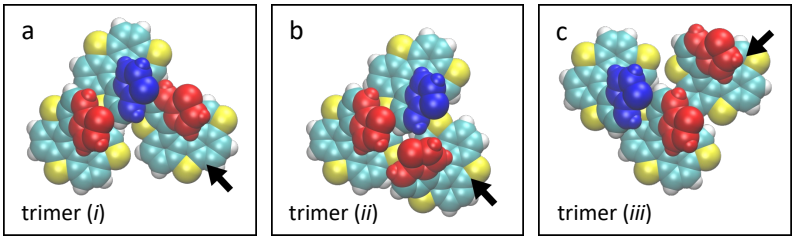


Figure 4.12: Top views of trimers formed with high probabilities.

The migration process of three [7]TH enantiomers (n = 3), consisting of two (M)-type molecules and one (P)-type molecule, was further examined on the graphene. As the simulation progressed, the molecules spontaneously aggregated into trimeric structures driven by attractive intermolecular interactions. In almost all of the samples (50 samples with different initial configurations), two of the heterochiral enantiomers were arranged into the same back-on-back configuration as the heterochiral dimer discussed previously; therefore, the trimers were identified as a heterochial pair attached with an additional enantiomer ((M)-type molecule in this case, indicated by the arrow in Figure 4.12). Figure 4.12 shows three different trimer configurations that mainly appeared in the MD simulations: 27% for trimer(i), 32% for trimer(ii), and 30% for trimer(iii). Notably, trimer(i) was composed of both dimers I and II aligned, where every neighboring pair of heterochiral molecules was arranged in a back-on-back configuration with an identical intermolecular distance of 8.6 Å. The "line-up" arrangement of trimer(i) indicated an important unit for the elongation of the dimer alignment to form the zigzag-chain configuration, as discussed later. Compared with the two molecules adopting the back-on-back dimer configuration, the attached molecule in trimer(i) is less stable and can change its azimuthal orientation owing to thermal fluctuation. In most samples, the molecule was inverted to make the upper parts of its skeletons overlap with those of the other molecules to form trimer(ii). The inversed orientation of the attached molecule

seems to increase the overlapping region between the helical skeletons of the neighboring molecules, further stabilizing the molecular cluster (E_{int} = –1.28 eV for trimer(i) and E_{int} = –1.30 eV for trimer(ii)). As a relatively small difference in interaction energy is observed between heterochiral and homochiral dimers in MD simulations, it is acceptable that the additional (*M*)-type molecule is attached to another homochiral enantiomer to form trimer(iii). The E_{int} of trimer(iii) was estimated to be –1.25 eV, which indicates that the stability of this trimer is lower than that of the trimer composed of heterochiral neighboring pairs.

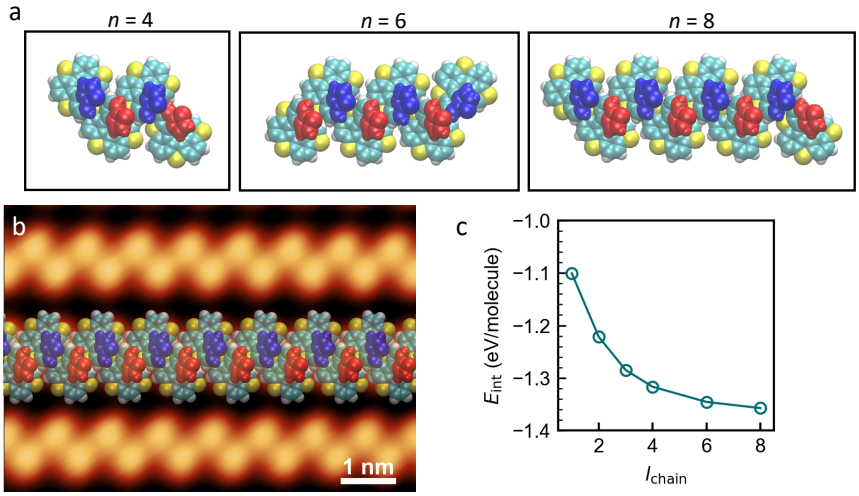


Figure 4.13: (a) Linear patterns formed by n = 4, 6, and 8 different[7]TH enantiomers. (b) Molecular model of the zigzag chain sturcture imposed on a STM image (2.0 V, 50 pA). (c) Interaction energy per molecule (E_{int}) dependence of n enantiomers consisting in the chain structure.

To explore the formation mechanism of the long-range ordered structure of *rac*-[7]TH, pairs of opposite enantiomers were subsequently introduced onto the surface in a stepwise manner, increasing the system size to n = 4, 6, and 8 molecules. As the number of molecules increased, the unit cell was correspondingly enlarged to maintain the concentration of molecules in the unit cell. In all three cases, the molecules easily aggregated into small clusters.A characteristic linear pattern was observed for different cluster sizes, in which [7]TH enantiomers align and arrange alternately (Figure 4.13a). Within this motif, neighboring molecules bind through overlapping upper helical skeletons, adopting a back-on-back configuration. This strongly suggests that the heterochiral dimer of [7]TH was a crucial building block for the growth of this linear pattern. Remarkably, the linear chain pattern well reproduced the zigzag-chain structures shown by our previous STM observations of *rac*-[7]TH on Ag(111). As the bright circular protrusion was considered as

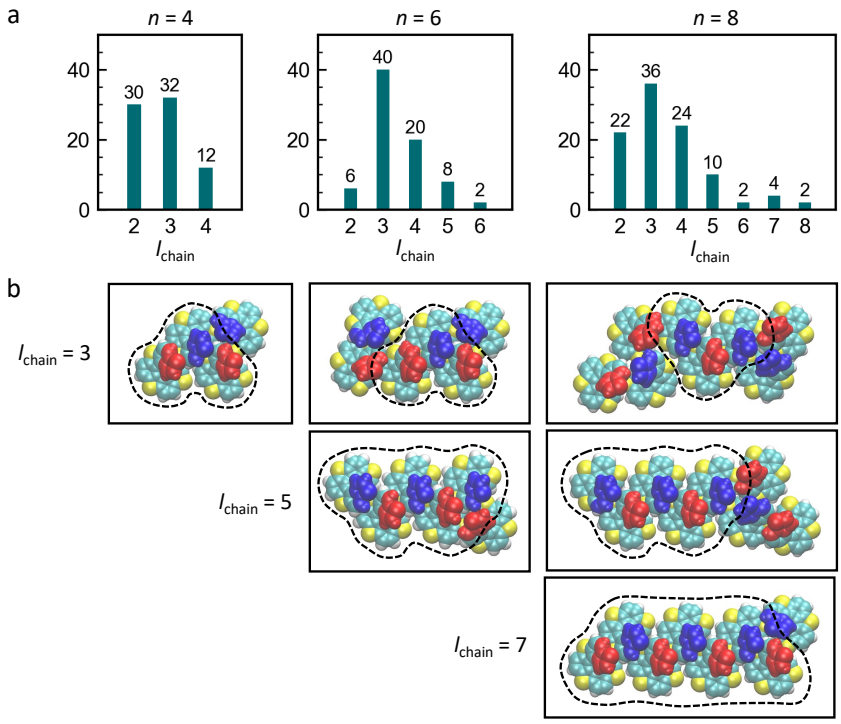


Figure 4.14: (a) Histograms of the zigzag chains formed with different number of molecules in the chain (l_{chain}). (b) Molecular arrangements containing zigzag chains with different length.

a single [7]TH molecule in the STM image, a structural model for the zigzag-chain pattern is proposed as follows. Opposite enantiomers arrange alternately and align with the upper parts of their skeletons located on the inner side of the chain (Figure 4.13b). The average distance between two neighboring identical enantiomers along the linear pattern was estimated to be 11.1 $\pm$ 0.1 Å, which was in accordance with our experimental results for the Ag(111) surface (11.1 $\pm$ 0.1 Å). As discussed above, the interactions between the thiophene rings and the Ag surface are relatively weak; consequently, molecular recognition among [7]TH molecules is primarily governed by π–π interactions between the steric structures. Accordingly, the chain length (l_{chain}) is defined as the number of molecules aligned in an alternating back-on-back configuration. Figure 4.13c shows the profile of interaction energy per molecule as a function of the number of molecules consisting of a single chain, which decreases monotonically as l_{chain} increases. The π–π interactions between neighboring molecules stabilize the structure as it grows longer. Similar chain-like arrangements were also reported for racemic mixture of [7]CH on Cu(111), Ag(111), and Au(111) because the skeletons of both [7]TH and [7]CH exhibit similar degrees of helicity. The zigzag chains are one of the most prevalent

patterns observed for racemic mixtures of helicenes composed of seven aromatic rings on the surface.[66,72,74,96,98]

Besides forming the linear patterns as zigzag chains, the molecules tended to aggregate into two-dimensional clusters in which some of the molecules adopted the chain-like configuration. Figure 4.14a shows the histograms of the zigzag chains with different l_{chain} values for the system composed of n = 4, 6, and 8 molecules (selected cases of different zigzag chains are shown in Figure 4.14c). As n increases, the distribution of heterochiral dimers (l_{chain} = 2) gradually transits to short chains (l_{chain} = 3, 4) and long chains appear, suggesting the process that building blocks start aggregating into ordered structures. Despite increasing n included in the system, short chains (l_{chain} = 3, 4) were prevalent among the two-dimensional clusters, whereas the formation of an ordered long chain was observed in rare cases. Although such non-ordered two-dimensional clusters were not observed at low coverage experimentally due to the limited time resolution of the STM measurements, these structures are expected to appear transiently during the formation of zigzag chains. With increasing molecular coverage, stronger lateral intermolecular interactions emerge, which help stabilize ordered structures.[72] In the case of eight-molecule clusters, the prominent l_{chain} decreased from 8 to 3, indicating that long chains were rarely formed. It is noteworthy that a long chain (l_{chain} = 8 and 2%) was occasionally formed in the MD simulations, and the obtained chain structure was unique and closely matched the structure observed in the experiment, where the back-on-back configuration was clearly realized. This finding highlights the importance and value of MD simulations, as they provide insights into the formation and stability of ordered structures formed by *rac*-[7]TH.

4.5 Molecular Configurations of Neighboring Chain Pairs

To investigate the interactions between neighboring zigzag chains, the relative arrangement of two chains, each composed of four alternating [7]TH enantiomers, was considered. Four representative molecular configurations were proposed, as illustrated in Figure 4.15. Both chains were aligned parallel to the x-axis, and the length in the x-direction of the unit cell was modified to be commensurate with the chain's period, thereby producing long-range, defect-free chain structures in the MD simulations. Three parameters were used to evaluate the interactions between neighboring chains. The first parameter was the alternation of the two enantiomers along the axis perpendicular to the paired chains, as arranged with the "PMPM" and "MPPM" geometries along the y-axis. The second parameter was the phase shift along the chain direction of the two neighboring chains. When the two chains

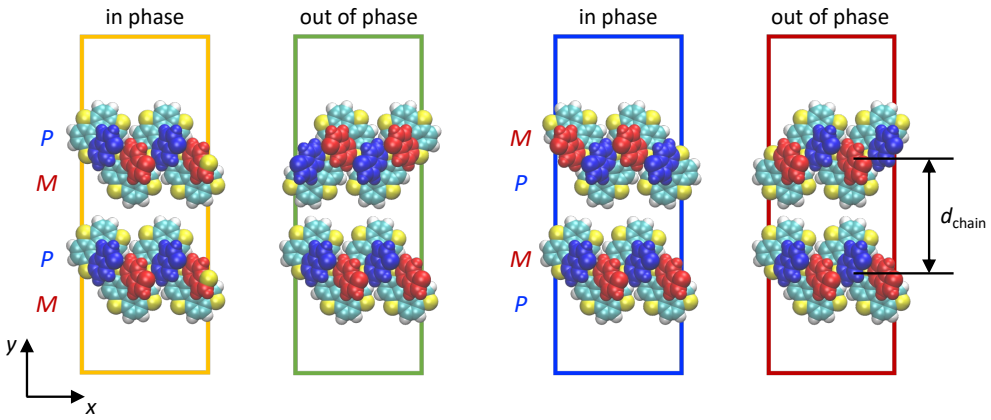


Figure 4.15: Schematic of four molecular configurations composed of two zigzag chains on graphene. Rectangles represent the unit cells (21.60×58.20 Å^2) used in the MD simulations.

share the same periodic alignment, they are defined as "in phase," whereas a relative shift of half a period corresponds to the "out-of-phase" configuration. The third parameter was the distance between the chains, d_{chain}, which was the in-plane distance between the geometric centers of two chains.

Excluding the interactions of the molecules with the surface, the formation energy per molecule for molecular chains was calculated as:

$$E_{\text{form}} = (E_{[7]\text{TH/gra}} - nE_{[7]\text{TH}} - E_{\text{gra}})/n - E_{\text{ads}} \tag{4.3}$$

Where $E_{[7]\text{TH/gra}}$, $E_{[7]\text{TH}}$, and E_{gra} represent the potential energies of the [7]TH/graphene system, an isolated free [7]TH molecule, and isolated clean graphene, respectively; E_{ads} represents the adsorption energy of a single [7]TH on graphene; and n is the number of molecules forming the chains.

Figure 4.16a shows E_{form} as a function of d_{chain} for the four arrangements; this energy was calculated using static molecular configurations. Our simulations predicted that two chains aligned in the "PMPM" geometry with identical shapes represented the most favorable arrangement for a pair of neighboring chains (yellow curve), with an optimum interchain distance of about 17.0 Å. The geometries of the chains aligned with a half-period phase shift (red and green curves) exhibited similar energy profiles, with an average optimum distance of 19.0 ± 0.1 Å. It was found that chains in identical phase could approach each other more closely because the zigzag-chain structures of each chain matched well with their neighbors. This resulted in stronger pairwise interactions and thus lower energy than the half-phase shift arrangements.

Interestingly, STM observations revealed that neighboring chains with a half-

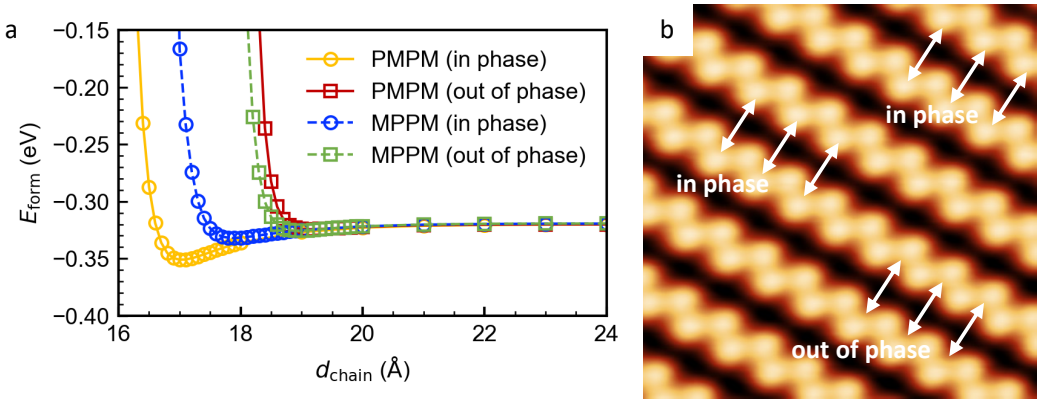


Figure 4.16: (a) Formation energy (E_{form}) dependence of dchain for four different molecular configurations. (b) Coexistence of different phase shifts between neighboring chains in STM images (10×10 nm^2, 2.0 V, 50 pA).

phase shift were the most prevalent in the zigzag-chain structures formed on the Ag terraces. Other configurations, including chains in identical and different phase shifts, were also observed within the same domains (see Figure 4.16b). The average distance between neighboring chains was about 19.9 $\pm$ 1.5 Å. The coexistence of pairing chains in different phase shifts within a single domain suggests that different chain phases are nearly equivalent in stability, as indicated by the small energy variation ($\approx$ 30 meV) among the four arrangements in the MD simulations. The interactions between the peripheral sides of neighboring chains, namely van der Waals interactions between the lower skeletons of [7]TH enantiomers, were considered weak. As a result, the arrangement of neighboring zigzag chains could be easily influenced by other factors such as surface molecular coverage, substrate characteristics, molecule–tip interactions during STM scanning, and so on.

The graphene used in the MD simulations provided a smooth potential surface for adsorbed [7]TH molecules, lacking obvious adsorption sites or orientation dependence in the formation of a single zigzag chain. Therefore, no significant forces hindered two chains from approaching closely enough to maximize attractive interactions. Eventually, two chains in identical phase could approach each other to within 17 Å, limited only by steric hindrance between the nearest neighboring molecules. Although our DFT calculations suggest that the interactions between [7]TH and the Ag surface are weak, surface localization of the molecules still appears to influence the ordered structures formed by *rac*-[7]TH on Ag(111).

4.6 Conclusions

The formation mechanism of the ordered structures of *rac*-[7]TH on Ag(111) was theoretically studied with a small number of molecules. DFT calculations suggested that [7]TH was physisorbed on Ag(111), with no significant S–Ag interactions during adsorption, which well coincided with XPS. MD simulations were conducted on a graphene substrate and successfully reproduced zigzag-chain structures similar to those observed by STM on Ag(111), in which the heterochiral dimer, combined through π–π interactions, was formed as a crucial building block for the chain structure. The arrangements of the neighboring chains were also evaluated using four *rac*-[7]TH molecules, in which two energetically equivalent arrangements between the neighboring chains appeared. Compared with the STM observations, MD simulations showed a smaller distance between two neighboring chains on graphene, suggesting that the correlation between the Ag(111) surface localization and the molecular assemblies slightly modulated the two-dimensional long-range ordering of [7]TH. The MD simulations clearly demonstrated the initial stage of chiral recognition consisting of a small number of molecules, which was difficult to demonstrate as the molecular level by experimental methods such as STM. The dynamic process involved in the formation of assemblies of chiral molecules can clarify the formation processes for two-dimensional chiral systems by using artificial, and nonbiological helicene molecules. This approach is promising for investigating other similar systems and even for exploring the hierarchical diversity of chiral biosystems.

Chapter 5

Chiral Recognition Mechanism of 2,13-Bis(hydroxymethyl)-[7]Thiaheterohelicene on Ag(111) Investigated by STM and MD Simulations

The main results presented in this chapter have been published in the following paper.

Changqing Ye, Takuma Hattori, Yuji Hamamoto, Pawel Krukowski, Akira Saito, Hideji Osuga, Yoshitada Morikawa, and Yuji Kuwahara, "Chiral Recognition Mechanism of 2,13-Bis(hydroxymethyl)-[7]thiaheterohelicene on Ag(111) Investigated by STM and MD Simulation." *Int. J. Mol. Sci.* **2025** *26*(23), 11458.

5.1 Introduction

As introduced in chapter 2, among the various ordered structures formed by helicenes on solid surfaces, racemic and enantiopure helicenes are often found to exhibit distinct assembly patterns. In particular, chain-like structures are commonly observed in racemic helicenes, while the structural motifs formed by enantiopure helcienes are more strongly influenced by the properties of the underlying substrate, which reflect the subtle interplay between molecular chirality and surface symmetry.

Thiaheterohelicenes, consisting of alternant thiophene and benzene rings, have attracted significant attention due to their inherent helical geometry and the easy functionalization at the terminal thiophene rings. This structural tunability makes

them ideal candidates for studying how functional groups affect molecular recognition and self-assembly on surfaces.

This chapter investigates the adsorption and aggregation properties of 2,13-dihydroxymethyl-[7]thiaheterohelicene (refer as [7]TH-diol, Figure 5.1) on Ag(111) using STM and MD simulations. The hydroxymethyl groups at the terminal of the molecular skeleton are expected to facilitate hydrogen bonding with neighboring molecules, thereby modulating the molecular arrangement and stabilizing ordered two-dimensional structures.

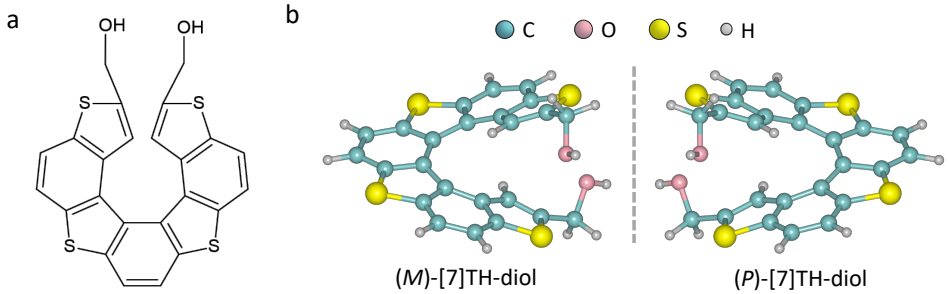


Figure 5.1: (a) Structure, and (b) ball-and-stick models of [7]TH-diol.

5.2 Methods

All the experiments were carried out using a low-temperature ultrahigh-vacuum STM system (UNISOKU Co., Ltd., USM1400) at a base pressure of less than 1.0×10^{-10} Torr. The scanning system was controlled by a Nanonis BP 5 controller (SPECS GmbH). STM images were obtained at 80 K in constant-current mode using electropolished PtIr tips (UNISOKU Co., Ltd.) and analyzed using the Gwyddion[153] package. The Ag(111) films epitaxially grown on mica (Georg Albert PVD) were used as substrates. The Ag(111) surfaces were cleaned by repeated cycles of Ar^+ ion sputtering and subsequent annealing at 633 K. The *rac*- and (*M*)-[7]TH-diols were thermally deposited separately at a pressure less than 3.0×10^{-8} Torr using a Knudsen-type organic molecular evaporator (KITANO SEIKI Co., Ltd.) inside a preparation chamber. The *rac*- and (*M*)-[7]TH-diols were deposited on the substrates at 483 K and 510 K, respectively, while the substrates were held at room temperature. The synthesis and optical resolution of [7]TH-diol were described elsewhere[154]. Previous studies have shown that [7]TH possesses a much high activation barrier for racemization, and that the introduction of functional groups to the helical backbone does not significantly alter this activation energy.[155] Such a large barrier ensures that the helical configuration remains stable under our experimental

conditions. Accordingly, we expect a similar activation barrier for [7]TH-diol, and its chirality should be well preserved during the sublimation process in the experiments.

MD simulations were carried out using the LAMMPS[148] program. The force field parameters were derived from the GAFF[117,118] and applied as identical as described in Chapter 4. A flat Ag(111) surface was approximated by a monolayer graphene sheet with a lattice constant of 2.46 Å. To investigate the aggregation behavior of [7]TH-diol on graphene at a low surface coverage, the size of a unit cell (*xy*-plane) was changed with a constant molecular number density of approximately 0.2 molecules/nm^2, which corresponded to a different number of molecules in the system (see Figure S1). To investigate the formation of long-range zigzag chains, the *x*-dimension was changed to be commensurate with the periods of chain structures, and the y-dimension was fixed at 51.05 Å. The perpendicular dimension (*z*) was 40.00 Å and kept orthogonal to the *xy*-plane in all the cases. Periodic boundary conditions were applied in all three directions. Initially, the molecules were randomly positioned on the graphene substrate, and the distances between the geometric center of molecules and the substrate were set at 5.00 Å.

The general AMBER force field (GAFF)[118,156] was employed to describe the interactions between atoms. The force fields used in this study all rely on fixed partial charges to describe Coulomb interactions and on the Lennard–Jones 6–12 model to describe van der Waals interactions. The Coulomb interaction energy E_{Coul} and van der Waals interaction energy E_{vdW} are presented as,

$$E_{\mathrm{Coul}} = \sum_{i=1}^{N} \sum_{j>i}^{N} \frac{q_i q_j}{4\pi\varepsilon_0 r_{ij}} \tag{5.1}$$

$$E_{\mathrm{vdW}} = \sum_{i=1}^{N} \sum_{j>i}^{N} 4\epsilon_{ij} \left[\left(\frac{\sigma_{ij}}{r_{ij}} \right)^{12} - \left(\frac{\sigma_{ij}}{r_{ij}} \right)^{6} \right] \tag{5.2}$$

r_{ij} represents distance between two atoms i and j. Partial charges q_i and q_j were calculated using the AM1-BCC algorithm[122,123] and are listed in Table S1. The Lennard–Jones interaction parameters σ_{ii} and ϵ_{ii} were obtained from AMBER force field[118,156]. For unlike atom pairs, the Lennard–Jones parameters were calculated using the Lorentz–Berthelot rules. Note that partial charges and Lennard–Jones parameters were not assigned to the carbon atoms in the graphene sheet. The graphene substrate was frozen, and the structures of adsorbates were fully relaxed while the SHAKE algorithm[157] was adopted to keep C–H bonds rigid during the simulations. The molecules' temperature was controlled using the Nosé–Hoover thermostat[134,135] with a time step of 1 fs. After the initial energy minimization, the system was equilibrated at 275 K for 2 ns and cooled to 80 K at a controlled cooling

rate of 100 K/ns. After cooling, the system was equilibrated at 80 K for 0.5 ns, and thermal dynamic data were sampled every 0.1 ps during this period for further analysis.

The adsorption energy of molecular clusters on the surface was defined as

$$E_{\mathrm{ads}} = (E_{\mathrm{molecule/substrate}} - nE_{\mathrm{molecule}} - E_{\mathrm{substrate}})/n \tag{5.3}$$

where $E_{\mathrm{molecule/substrate}}$, E_{molecule}, and $E_{\mathrm{substrate}}$ represent the potential energies of the adsorption system, isolated free molecule, and isolated substrate, respectively; *n* is the number of molecules included in the adsorption system.

5.3 STM Observation of Ordered Structures of [7]TH-diol on Ag(111)

After depositing *rac*-[7]TH-diol on Ag(111), the molecules self-assembled into well-ordered islands surrounded by disordered areas on the terraces of Ag(111), as shown in Figure 5.2a. The ordered islands were characterized as zigzag chains, with the chain directions tilted clockwise or anticlockwise by $20 \pm 5^{\circ}$ from the $[1\bar{1}0]$ direction of the substrate surface. The distance between neighboring molecules along the chain direction was 1.2 ± 0.1 nm. The density of molecules in the zigzag chain structures was 0.69 ± 0.04 molecules/nm^2, which is defined as one monolayer (ML). Such ordered molecular islands were observed only when the surface coverage of the molecules reached approximately 1 ML. At lower coverages, molecular resolution was degraded due to the high mobility of the molecules on the surface. Similar chain structures were also observed for [7]TH and [7]TH-CHO on Ag(111).[71,72] The circular protrusions represent individual [7]TH-diol molecules in Figure 5.2b, in which small bright spots are randomly distributed inside these protrusions and were shifted close to the twin rows. These randomly distributed bright spots suggest the highest parts of individual molecules, possibly the hydroxymethyl groups oriented away from the surface.

On the other hand, (*M*)-[7]TH-diol was observed to form chain structures on Ag(111), as shown in Figure 5.2c. The chain directions were tilted clockwise or anticlockwise by $31 \pm 10^{\circ}$ from the $[1\bar{1}0]$ direction. Figure 5.2d shows an enlarged STM image of the chain structures, where each bright protrusion represents a single molecule. The distance between neighboring molecules along the chain was 1.1 ± 0.1 nm, and the density of molecules was 0.74 ± 0.06 molecules/nm^2. Further contrast within the protrusions reveals an off-centered bright spot in each molecule. The equally distributed bright spots suggest that the chain structures were composed of (*M*)-[7]TH-diol molecules with the same orientation.

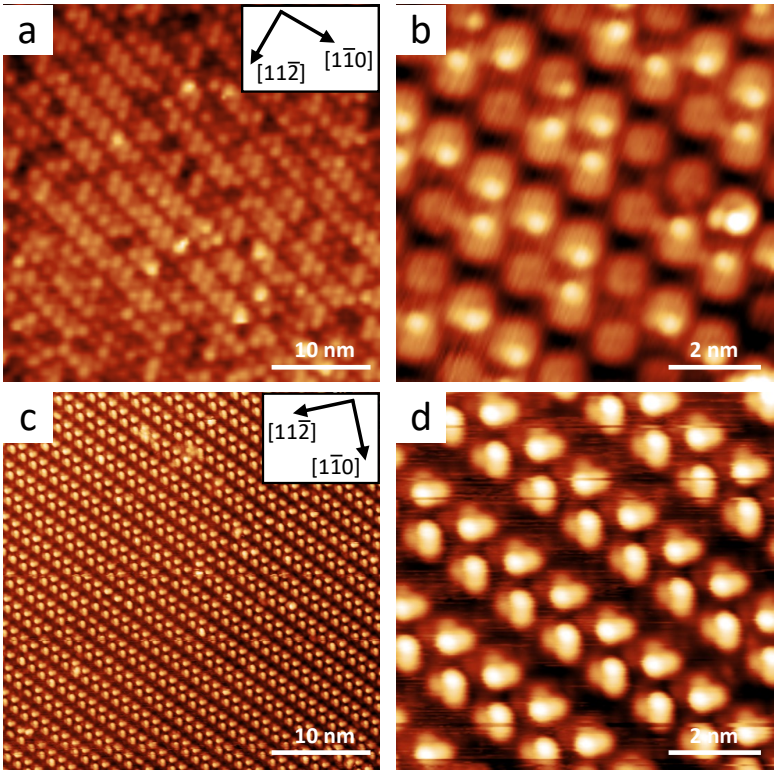


Figure 5.2: (a) and (b) STM images of the self-assembled structures of *rac*-[7]TH-diol on Ag(111). (c) and (d) STM images of the self-assembled structures of (*M*)-[7]TH-diol on Ag(111). The STM images were obtained at (a) 1.0 V, 20 pA, (b) 1.0 V, 20 pA, (c) –2.5 V, 25 pA, and (d) –2.5 V, 25 pA.

Although the overall chain morphology closely resembled that formed by *rac*-[7]TH-diol, notable differences were observed. The chains formed by (*M*)-[7]TH-diol exhibited a larger tilting angle relative to the substrate, a shorter intermolecular distance, and consequently a higher packing density, indicating a more compact molecular arrangement. These structural differences suggest that the chain conformations of *rac*- and (*M*)-[7]TH-diol may be inherently distinct.

Note that enantiopure carbohelicene molecules usually form trimers on the (111) surfaces or tetramers on the (100) surfaces of Cu, Ag, and Au substrates, reflecting the surface symmetry.[96,98,137] This contrasts with (*M*)-[7]TH-diol, which forms zigzag chains on both Ag(111) and Au(111).[70] This suggests that molecular recognition among [7]TH-diol molecules is largely influenced by the hydroxymethyl groups, and that molecule–substrate interactions becomes less significant for (*M*)- or (*P*)-[7]TH-diol.

5.4 MD simulations of [7]TH-diol

To elucidate the formation mechanisms of the self-assembled zigzag chains of [7]TH-diol on Ag(111), MD simulations were conducted for both racemic and enantiopure systems to investigate the molecule–molecule interactions in the ordered structures. Our X-ray photoelectron spectroscopy and DFT results have shown that [7]TH is certainly physisorbed on Ag(111).[72,158] As observed by STM, [7]TH and [7]TH-diol were highly mobile at low coverages on Ag(111), due to weak adsorption and the influence of the STM tip. These findings suggest that functionalization by hydroxymethyl groups at the terminals does not significantly affect the adsorption properties of [7]TH-diol on Ag(111).

Accordingly, intermolecular interactions are expected to play the dominant role in determining the arrangement of the self-assembled structures. To better capture these intrinsic interactions while minimizing substrate effects, a single-layer graphene sheet was employed in the MD simulations, as graphene provides a chemically inert and structurally simple platform with minimal influence on molecular assembly.

In addition, the GAFF force field used in this study is parameterized for organic and biomolecular systems and does not include reliable parameters for metallic atoms such as silver. As a result, directly modeling the Ag(111) surface would not provide reliable molecule–substrate interactions within this framework. Graphene, on the other hand, is widely adopted as a weakly interacting substrate in MD simulations, offering a well-defined and computationally compatible model that reproduces the essential physisorption characteristics observed experimentally on Ag(111). This approach allow us to isolate and analyze the intrinsic inter-molecular interactions governing the experimentally observed chain formation.[159]

5.4.1 Dimer Conformations

First, one (*M*)- and one (*P*)-[7]TH-diol enantiomer, as well as two (*M*)-[7]TH-diol enantiomers, were randomly placed on the graphene substrate to investigate the aggregation behavior of two molecules. At a temperature of 275 K, the molecules migrated across the surface and eventually associated to form dimers. The [7]TH-diol molecules were found to adsorb with one terminal oriented nearly parallel to the surface plane, with a perpendicular distance of approximately 3.5 Å between the center of the second benzene ring and the substrate, which is essentially identical to that observed for [7]TH on graphene.[158]

The trajectories of the two molecules were traced throughout the simulations, and their relative alignments were evaluated at 80 K using 50 different initial configurations. For a system consisting of one (*M*)-type and one (*P*)-type [7]TH-diol enantiomer, several distinct dimer configurations were identified. Among them, two

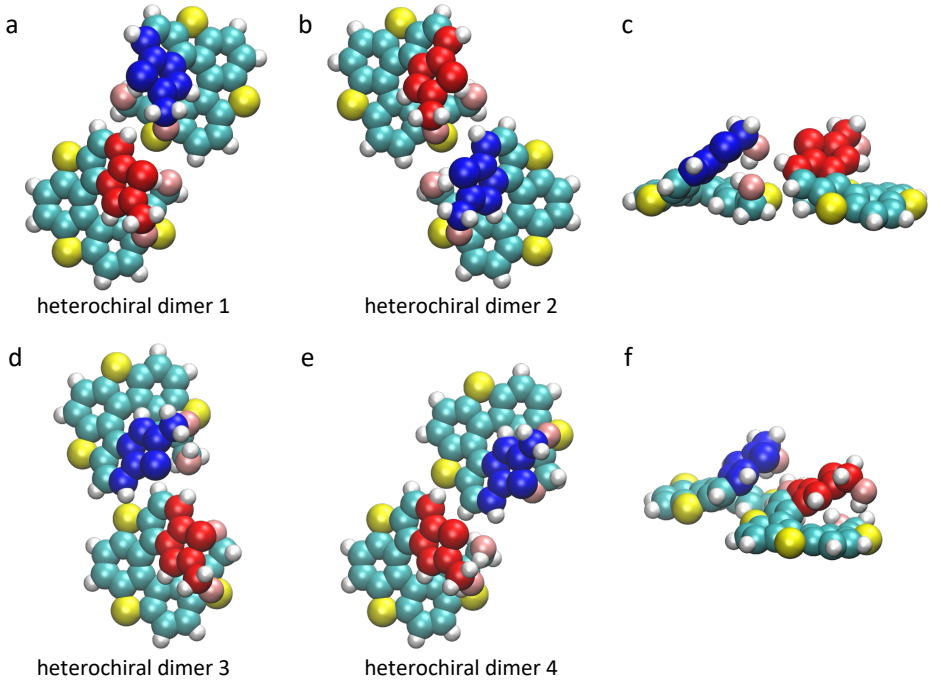


Figure 5.3: (a) and (b) Top views of the most favorable heterochiral dimers of [7]TH-diol. To distinguish enantiomers, the tops of (*M*)-type and (*P*)-type molecules are shown in red and blue, respectively. (c) Side view of heterochiral dimer 1.

particularly favorable arrangements are shown in Figure 5.3a, b, referred to as heterochiral dimers 1 and 2, respectively. These dimers had similar adsorption energies (E_{ads}) of –1.327 $\pm$ 0.010 eV per molecule, with formation probabilities of 38% and 32%, respectively. Notably, heterochiral dimers 1 and 2 are mirror images of each other, and the slight difference in their probabilities is attributed to statistical variation.

Heterochiral dimers are characterized by a "face-to-face" configuration, in which the enantiomers are rotated by approximately 180° relative to each other. This arrangement prevents partial overlap between the upper part of one molecule and the lower part of the other because of steric hindrance introduced by the terminal hydroxymethyl groups. In this geometry, the –OH groups are oriented inward toward the helical skeletons, and the O$\cdots$H distance between the nearest hydroxyl groups exceeds 4.00 Å. The side view of heterochiral dimer 2 (Figure 5.3c) indicates that interactions between the spiral skeletons, dominated by van der Waals forces, play a central role in stabilizing heterochiral dimers of [7]TH-diol. Additional heterochiral dimer configurations are shown in Figure 5.3d, e. In these dimers, the two enantiomers align in the same direction, similar to the case of [7]TH dimers.[158] However,

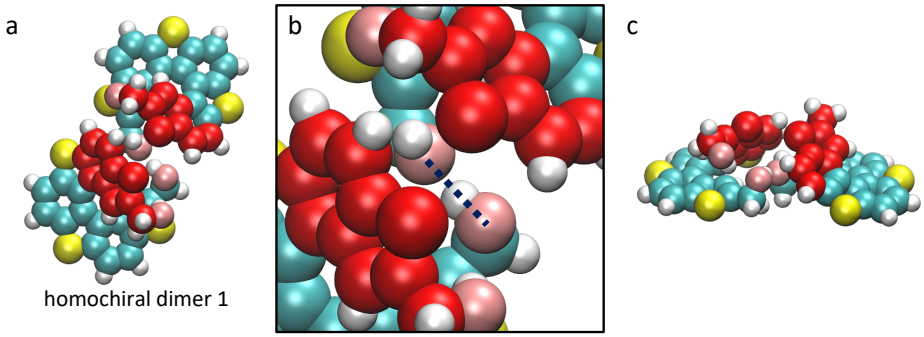


Figure 5.4: (a) Top view of the most favorable homochiral dimer of [7]TH-diol. (b) Enlarged image of the lower hydroxymethyl groups of two molecules, the dashed blue line represents the hydrogen bond forming between the molecules. (c) Side view of the homochiral dimer.

the steric repulsion between the hydroxymethyl groups increases the intermolecular separation, resulting in weaker interactions and lower stability compared with heterochiral dimers 1 and 2.

In the case of two (*M*)-type enantiomers, only one unique homochiral dimer was identified as a stable structure (Figure 5.4a). The E_{ads} of this dimer was calculated to be –1.371 $\pm$ 0.010 eV per molecule, indicating that the homochiral dimer is slightly more stable than the heterochiral ones. In this homochiral dimer, the (*M*)-type molecules are rotated approximately 90° relative to each other, with the upper parts of their helical skeletons standing upright and facing each other (Figure 5.4c). Additionally, the –OH groups proximal to the surface have a specific orientation, forming a hydrogen bond characterized by an angle of approximately 162° between O$\cdots$H–O and an O$\cdots$H distance of 1.86 Å (Figure 5.4b).[160] Importantly, while the lower –OH groups participate in hydrogen bonding within the dimer, the upper –OH groups remain exposed and face outward. This dimer configuration allows for additional hydrogen bonding interactions when another [7]TH-diol molecule approaches. The upper –OH groups of the third molecule can interact with the outward-facing –OH groups of the dimer, extending the hydrogen bond network among enantiopure [7]TH-diol molecules. This network facilitates the formation of larger assemblies and may influence the growth direction of the chain structures.

5.4.2 Formation of Chain-like Structures

Second, the number of molecules (*n*) in the MD simulations was increased to elucidate the formation mechanism of the zigzag-chain structures observed in both heterochiral and homochiral systems. With increasing *n*, the molecules showed a

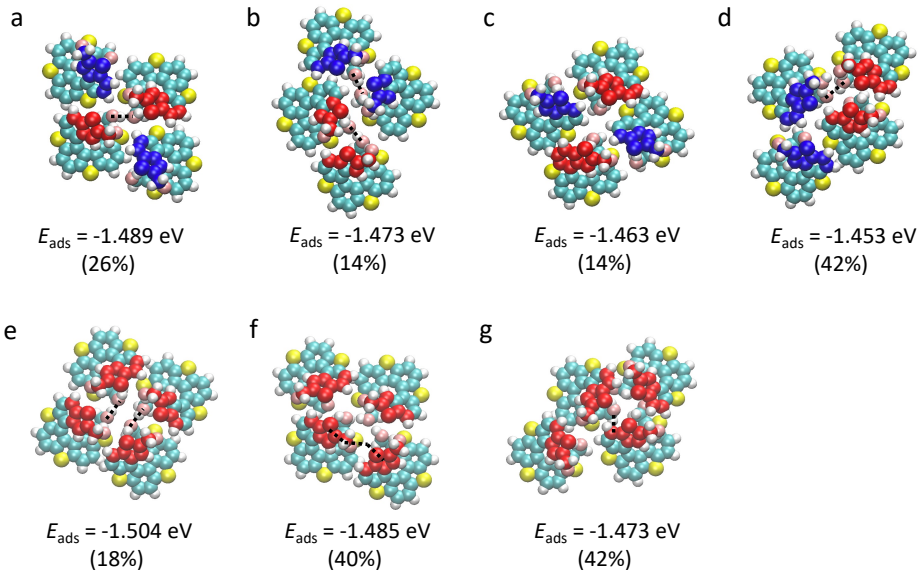


Figure 5.5: (a)–(d) and (e)–(g) homochiral tetramers of [7]TH-diol. The black dashed lines show hydrogen bonds forming between the molecules.

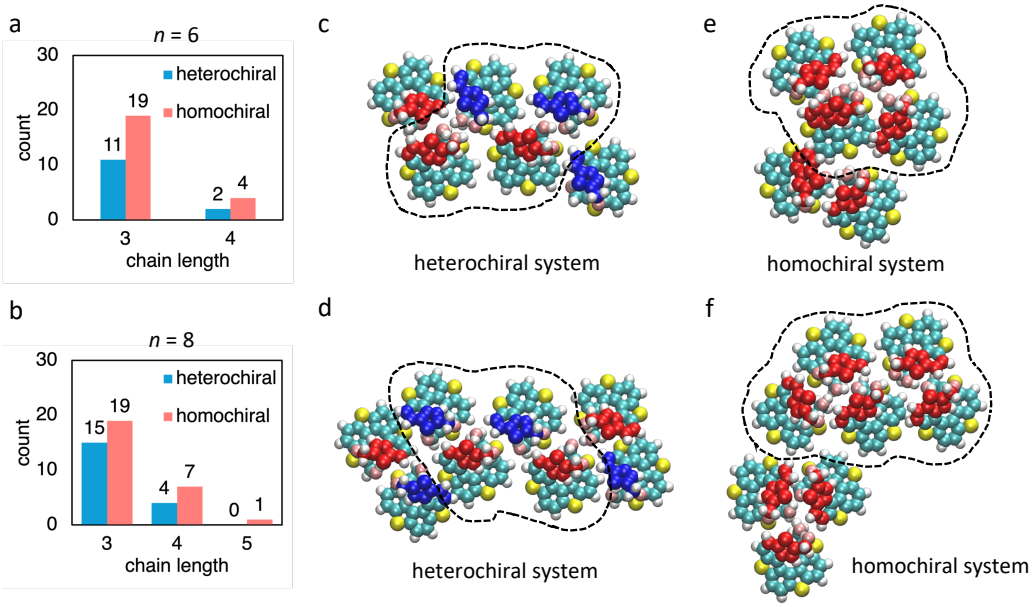


Figure 5.6: Histograms of chain-like structures found for systems composed of (a) $n = 6$ molecules, and (b) $n = 8$ molecules. (c) and (d) Molecular arrangements containing chain-like structures found in heterochiral systems. (e) and (f) Molecular arrangements containing chain-like structures found in homochiral systems. The frames with dashed lines represent the chain-like structures.

pronounced tendency to aggregate into clusters. When *n* reached four, the molecules formed tetramers with various molecular arrangements, with the predominant heterochiral and homochiral tetramers shown in Figure 5.5. Note that hydroxymethyl groups always approached one another to form hydrogen bonds with neighboring molecules, and at least one hydrogen bond was present in both heterochiral and homochiral tetramers.

Although hydrogen bonding between hydroxymethyl groups was preserved, the tetramer geometries did not correspond to straightforward one-dimensional extensions of the dimer configurations. This deviation is attributed to changes in intermolecular interactions and increased steric constraints as additional molecules were incorporated into the assemblies.

To gain further insight into these chain-like arrangements, a population analysis was performed based on 50 independent simulations with different initial molecular configurations. The results are presented as histograms in Figure 5.6a, b for larger clusters with *n*= 6 or 8. Here, the chain length is defined as the number of molecules arranged in dimer-like configurations. Chain-like motifs were identified within the molecular assemblies, as illustrated in Figure 5.6c–f.

The nearest-neighbor arrangements within these chains closely resemble those observed in both heterochiral and homochiral dimers, indicating that dimer interactions play a key role in guiding the formation of extended structures. Predominantly short chain segments were observed, typically consisting of three or four molecules arranged in a chain-like manner. Owing to the presence of surrounding molecules, the molecules in short chains slightly adjust their relative orientations. The molecules were initially placed at random positions on the substrate, which allowed for a high degree of freedom. Therefore, it was difficult for all molecules in the system to form a single, extended linear chain. Notably, the probability of forming chain structures in heterochiral systems was lower than that in homochiral systems. This phenomenon is attributed to a slight difference in E_{ads} between the heterochiral and homochiral dimer configurations. Additionally, in the heterochiral systems, the combination of one (*M*)-type and (*P*)-type molecules can lead to several different heterochiral dimers, further impeding the formation of extended chain-like structures. As a result, the molecules tend to become trapped in specific metastable configurations that are stable throughout the simulations, making it difficult for them to overcome the associated energy barrier to reorganize and facilitate chain elongation.

Extended Molecular Chain Models

To clarify the intermolecular interactions in the formation of long-range zigzag chains of [7]TH-diol, chain-like assemblies consisting of eight molecules were constructed to build models under periodic boundary conditions. Initially, the molecules

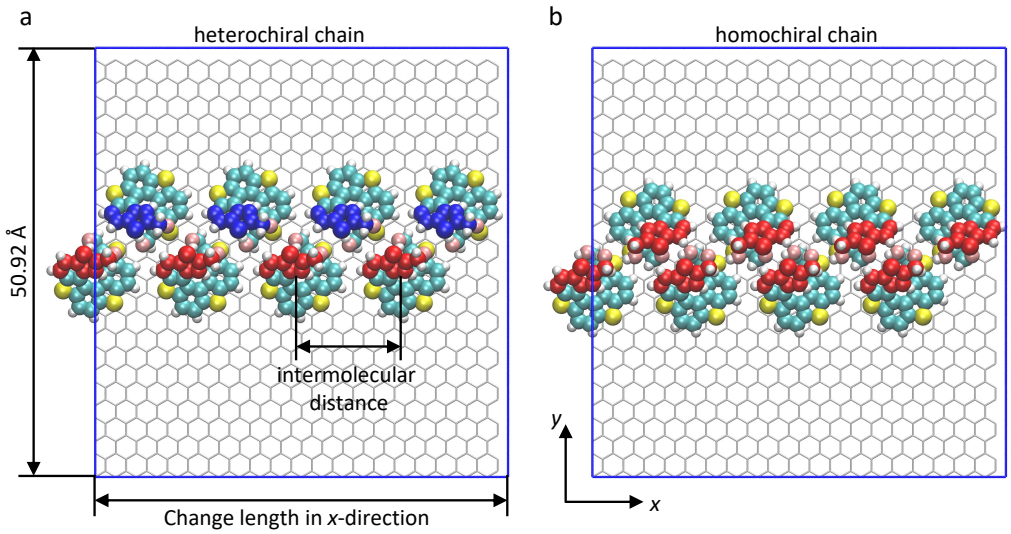


Figure 5.7: Molecular models of (a) racemic and (b) enantiopure chains on graphene, the intermolecular distance is 13.50 Å. Blue frames represent the unit cells used in the MD simulations.

were set to be uniformly arranged along the chain that extended in the *x*-direction. In the heterochiral system (Figure 5.7a), each neighboring pair of (*M*)-type and (*P*)-type enantiomers has either the configuration of heterochiral dimer 1 or 2, with an alternating arrangement of different enantiomers along the racemic chain. In contrast, in the homochiral system (Figure 5.7b), the hydroxymethyl groups of (*M*)-type molecules gather toward the center of the enantiopure chain, bringing the –OH groups close together. This arrangement allows the lower and upper –OH groups to form alternating hydrogen bonds with neighboring molecules along the chain.

The adsorption energy of the chain was obtained by changing the distance between neighboring molecules, which was carried out by modifying the unit cell length in the *x*-direction for the integer of multiples of the graphene lattice constant. To maintain the chain structures with different periodicities, the chain models were equilibrated at 1 K for 500 ps. The chain structures after equilibration are present in Figure 5.8 and Figure 5.9.

In Figure 5.10a, E_{ads} is plotted as a function of intermolecular distance. It was found that the racemic chain exhibited its lowest E_{ads} of –1.869 eV with an optimized intermolecular distance of 12.28 Å, whereas the enantiopure chain showed a slightly higher E_{ads} of –1.863 eV at 10.44 Å. Although the energy difference between the two chain configurations appears small on a per-molecule basis, it becomes more appreciable when considering extended chains, leading to a more distinct thermodynamic preference for the racemic arrangement. This small dif-

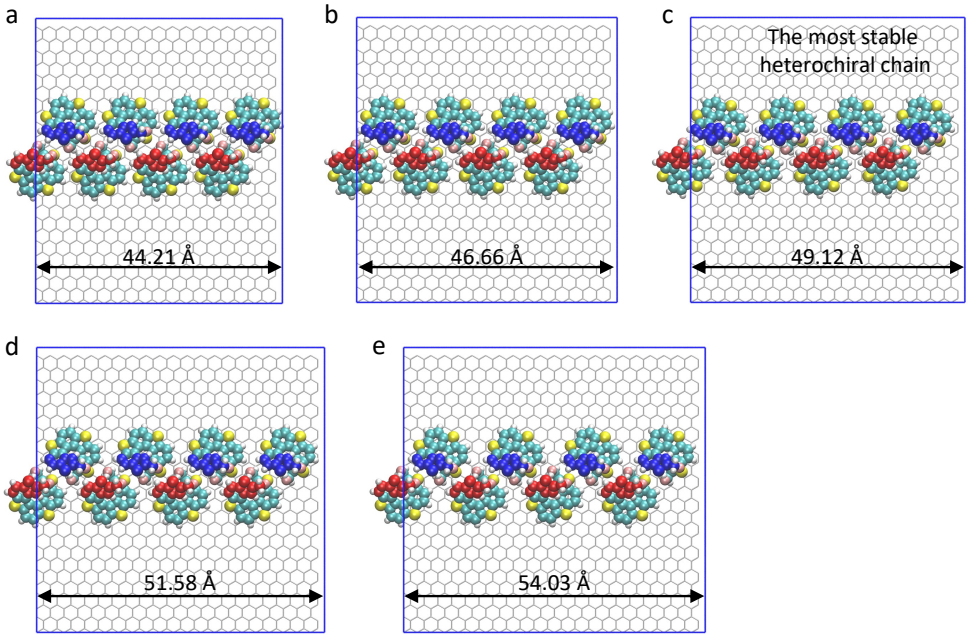


Figure 5.8: The optimized structures of racemic chain with different length. The most stable racemic chain has intermolecular distance of 12.28 Å.

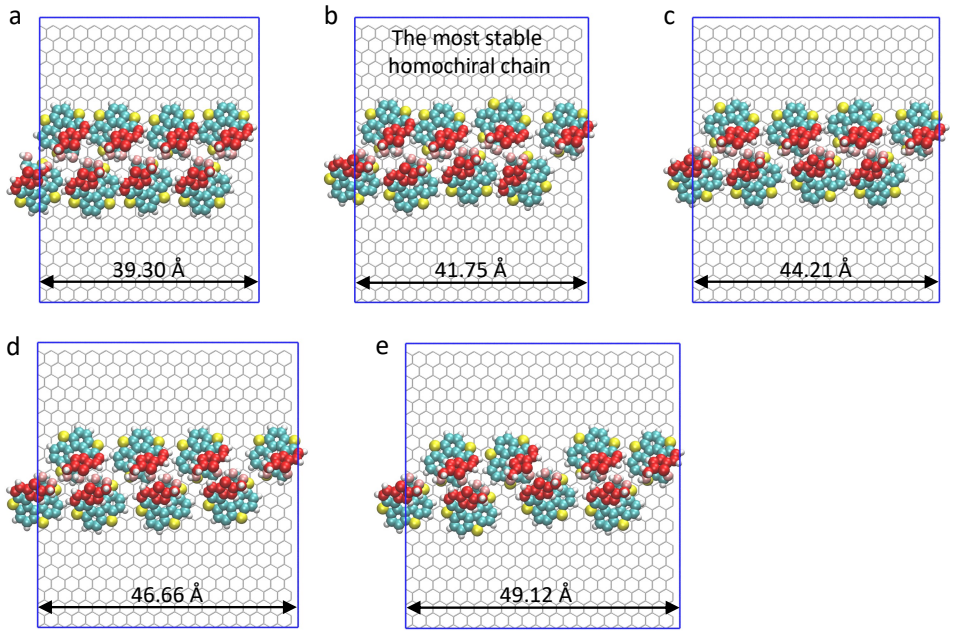


Figure 5.9: The optimized structures of enantiopure chain with different length. The most stable enantiopure chain has intermolecular distance of 10.44 Å.

ference is comparable to the intrinsic uncertainty of the force field; however, the consistent trend observed across multiple chain lengths and its agreement with the experimentally observed geometry indicate that the calculated preference is physically meaningful. The small energy difference between two chain configurations might be important for the chain formation at this low temperature. These intermolecular distances are in good agreement with the STM observations, where the racemic and enantiopure chains exhibited distances along the chains of approximately 1.2 ± 0.1 nm and 1.1 ± 0.1 nm, respectively. However, since the simulations were performed on a graphene substrate with weak molecule–substrate interactions, the adsorbed [7]TH-diol had no significant preferred adsorption site. As a result, the specific chain orientation observed in STM images could not be fully reproduced. The optimized racemic and enantiopure chain models were then equilibrated at 80 K for 500 ps, and both structures remained stable.

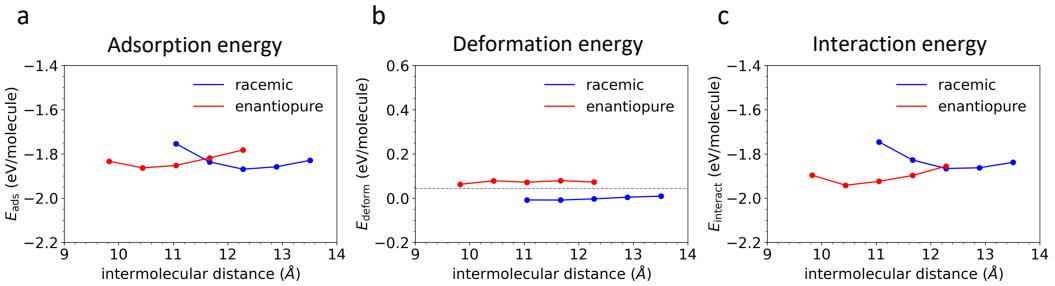


Figure 5.10: Energy profiles of (a) adsorption energy (E_{ads}), (b) the molecular deformation energy of the molecules (E_{deform}), (c) interaction energy (E_{interact}) are plotted as functions of intermolecular distance. The dashed line in (b) represents the E_{deform} of the adsorption of a single [7]TH-diol molecule on the graphene surface.

In MD simulations, the total potential energy consists of two main components: bonded energy and nonbonded interactions. The bonded energy accounts for intramolecular interactions within a molecule, including bond stretching, angle bending, and dihedral torsions. In contrast, the nonbonded energy comprises interactions between atoms that are not directly connected by covalent bonds, such as van der Waals forces and electrostatic (Coulomb) interactions. The bonded energy reflects how the internal molecular structure contributes to the overall energy, whereas the nonbonded energy governs how molecules interact with each other and with the substrate.

Accordingly, the difference in bonded energy between adsorbed molecule and free molecules can be interpreted as the deformation energy (E_{deform}, see Figure 5.10b). This deformation energy is calculated as the bonded energy of

the adsorbed molecule subtract that of the free molecule, reflecting the structural distortion induced by adsorption and/or interactions with neighboring molecules. Similarly, the difference in nonbonded energy can be interpreted as the interaction energy (E_{interact}, see Figure 5.10c), which includes contributions from both molecule–molecule and molecule–substrate interactions.

The total adsorption energy per molecule can therefore be expressed as:

$$E_{\mathrm{ads}} = E_{\mathrm{deform}} + E_{\mathrm{interact}} \tag{5.4}$$

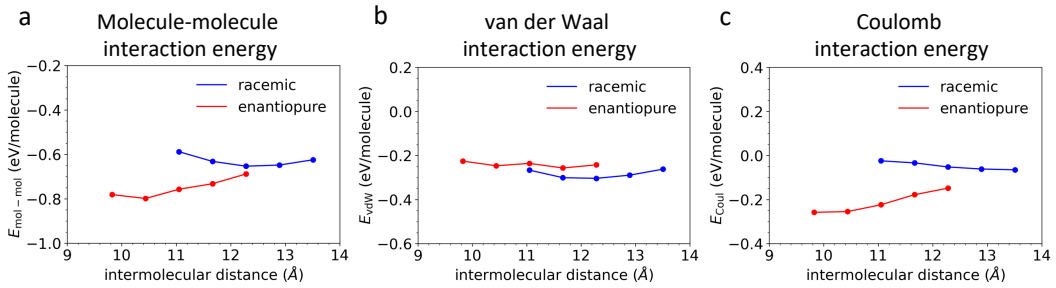


Figure 5.11: Energy profiles of (a) Molecule–molecule interaction energy ($E_{\mathrm{mol–mol}}$), (b) van der Waals interaction energy (E_{vdW}), and (c) Coulomb interaction energy (E_{Coul}) are plotted as functions of intermolecular distance.

As the averaged intermolecular distance increased shown in Figure 5.10, that is, unit length along the molecular chain increased, structural rearrangements were observed in both racemic and enantiopure chains to maintain favorable intermolecular interactions. In racemic chains, (*M*)-type and (*P*)-type enantiomers approached each other along the *y*-direction, resulting in a new molecular arrangement to preserved intermolecular distances (Figure 5.8). In contrast, in enantiopure chains, an increment of the unit length led to a deviation from a uniform molecular distribution, in which molecules tended to form closely associated pairs (Figure 5.9). Consequently, the average distance between the nearest-neighbor molecules remained nearly unchanged, and thus, E_{deform} remained nearly constant in both systems. These observations suggest that the intermolecular interactions are primarily governed by the interactions between nearest-neighbor molecules.

Notably, the absolute values of E_{deform} differ between the two systems: molecules in the enantiopure chain exhibit greater structural deformation than those in the racemic chain. This indicates that differences in molecular arrangement give rise to distinct intermolecular interactions, which in turn induce molecular deformation to stabilize the overall structure. When a single molecule is adsorbed, it may undergo conformational changes–such as changes in bond angles, dihedrals, or internal strain–to optimize its interactions with the substrate. The E_{deform} for a single

adsorbed molecule is shown as the dashed line in Figure 5.10b. Upon the adsorption of multiple molecules, additional intermolecular interactions can further affect the molecular conformation. In the case of enantiopure chains, the larger E_{deform} than that of a single adsorbed molecule is mainly due to hydrogen bonding between the neighboring molecules, which might cause additional structural distortion for the adsorbates. In contrast, for racemic chains, the E_{deform} is smaller than that of a single adsorbed molecule, suggesting that molecular deformation is reduced when multiple molecules are adsorbed together. The intermolecular interactions in racemic chains appear to stabilize the adsorbed molecules in a way that decreases their distortions. This implies that neighboring molecules can help support each other structurally, effectively reducing the strain on individual molecules and promoting a more energetically favorable structure.

The profile of E_{interact} (Figure 5.10c) shows that molecules in the enantiopure chain exhibit stronger intermolecular interactions than those in the racemic chain. Since the conformational changes induced by the molecular adsorption on the surface should be identical for both (*M*)-type and (*P*)-type enantiomers, the molecule–substrate interactions must also be identical for both enantiomers. Therefore, the greater deformation and interaction energies observed in the enantiopure chain should originate from interactions between neighboring molecules rather than from interactions between the molecules and the substrate.

To further elucidate the role of intermolecular interactions, the potential energy of the adsorbates was recalculated using the same molecular trajectories obtained from the MD simulations, while excluding molecule–substrate interactions. This approach enables direct evaluation of the intermolecular interaction energy, confirming that differences in molecular arrangements between racemic and enantiopure chains are primarily governed by intermolecular forces. Figure 5.11a shows molecule–molecule interactions ($E_{\mathrm{mol–mol}}$) of individual molecules within the chains.

To clarify how intermolecular interactions influence molecular arrangements, $E_{\mathrm{mol–mol}}$ was further decomposed into van der Waals and Coulomb components, as shown in Figure 5.11b and c, respectively. In the heterochiral system, van der Waals interactions dominate the formation of racemic chains, as the opposite helicities of the [7]TH-diol molecules allow their spiral skeletons to fit together effectively. In the homochiral system, van der Waals interaction also played a crucial role in the formation of the enantiopure chain. Additionally, In addition, Coulomb interactions make a significant contribution to structural stabilization, arising from hydrogen bonds formed between neighboring [7]TH-diol molecules.

Effect of different partial charge distributions

Since hydrogen bonding between neighboring molecules was found to play a crucial role in stabilizing the ordered structures of [7]TH-diol, particularly for zigzag

chains formed by (*M*)-[7]TH-diol, the influence of partial atomic charges on intermolecular interactions was examined in the MD simulations. AM1-BCC charges were used as the reference, and the Mulliken charges obtained at the B3LYP/6-311++G(d,p) level with Gaussian09 were tested for comparison. When Mulliken charges with reduced –OH polarity were employed, the resulting chains failed to preserve ordered structures, indicating that partial charges significantly affect the formation and stability of molecular assemblies.

5.4.3 Role of Functional Groups in Molecular Arrangements

The periodicities along individual zigzag chains observed experimentally were well reproduced by the MD simulations in both heterochiral and homochiral systems, indicating that the intermolecular interactions among [7]TH-diol are well captured by the simulation models. However, while chain-like structures formed from random initial configurations in the MD simulations on graphene do not exhibit any preferred orientation, the experimentally observed chains on Ag(111) tend to align along specific directions relative to the step edges. This contrast highlights the role of the substrate in directing large-scale organization and underscores a limitation of using graphene as a model substrate in the MD simulations. Despite this, the graphene-based simulations remain valuable for elucidating the inter-molecular recognition mechanisms that drive chain formation.

In the STM images, individual [7]TH-diol enantiomers appear as circular protrusions, and there were extra off-centered bright spots inside the protrusions. These bright spots are attributed to the upper portions of the molecules. Therefore, the STM images in Figure 5.2 can be interpreted as follows.

In the heterochiral system, neighboring molecules within the zigzag chains are primarily stabilized by van der Waals interactions between their steric skeletons. Under these conditions, the hydroxymethyl groups retain a relatively high degree of rotational freedom during STM measurements. Because [7]TH-diol adsorbs nearly flat on the surface, only localized rotations around the σ bonds connecting the hydroxymethyl groups to the helicene backbone are involved. Such localized rotations modulate the apparent height of terminal groups without altering the overall footprint. Consequently, the randomly distributed bright spots within the circular protrusions indicate that the orientations of the hydroxymethyl groups are only partially constrained and do not strongly influence the overall self-assembled structure. In contrast, in the homochiral system, hydrogen bonds form between the –OH groups of neighboring molecules, which restrict the rotation of the σ bonds connecting the hydroxymethyl groups to the helicene skeletons. As a result, the orientations of the hydroxymethyl groups become more fixed, leading to the uniform distribution of bright spots observed in the STM images.

Unlike other enantiopure helicenes on (111) surfaces of Cu, Ag, and Au,[96,98,137] which form trimer or tetramer motifs, (*M*)-[7]TH-diol assembled into zigzag chains, indicating that its molecular arrangement was primarily governed by intermolecular interactions rather than substrate effects. Since the molecule–substrate interactions for helicene and its derivatives are expected to be similar, the key factor differentiating the observed structures is the nature of the intermolecular interactions. In the case of enantiopure helicenes, the formation of small three-fold and four-fold motifs suggests that intermolecular forces alone are insufficient to drive extended chain formation, and surface symmetry plays a role in guiding molecular arrangement. In contrast, for [7]TH-diol, the presence of hydroxymethyl groups likely introduced additional hydrogen bonding interactions, which strengthened intermolecular attraction and promoted the formation of continuous chains, overriding any potential effect of surface symmetry. This suggests that functional groups play a crucial role in directing molecular assembly, even in cases where molecule–substrate interactions remain constant.

Accordingly, STM observations were performed for a series of thiaheterohelicene derivatives,[70–72,103] in which *rac*-[7]TH, *rac*-[7]TH-diol, and (*M*)-[7]TH-diol all form similar zigzag chains on Ag(111). Despite this apparent structural similarity in the STM images, MD simulations demonstrate that the molecular arrangements and conformations within the chains differ fundamentally among the three systems. For [7]TH on graphene, MD simulations show that *rac*-[7]TH forms zigzag chains with alternating (*M*)-type and (*P*)-type enantiomers arranged "back on back" via π–π interactions between neighboring molecules. In contrast, steric hindrance introduced by the terminal hydroxymethyl groups in [7]TH-diol prevents the similar conformation from [7]TH. As a result, *rac*-[7]TH-diol forms zigzag chains in which alternating (*M*)- and (*P*)-type enantiomers adopt a face-to-face arrangement, with the chain stabilized by van der Waals interactions between the spiral skeletons of neighboring molecules. The opposite conformation of neighboring molecules in the zigzag chains of [7]TH-diol also leads to an intermolecular distance along the chain larger than 11.1 ± 0.1 Å observed for [7]TH by STM.

In the case of (*M*)-[7]TH-diol, STM observations reveal the formation of zigzag-chain structures on Ag(111) that are similar to those observed in the racemic system. Within these chains, the –OH groups are oriented toward the interior of the chain, while the molecular backbones point outward, enabling the formation of hydrogen bonds with neighboring molecules through alternating upper and lower hydroxyl groups. As a result, the upper and lower hydrogen bonds alternate along the chains. Unlike the triangular or hexagonal motifs commonly formed by other helicene derivatives on the (111) surfaces of noble metal substrates,[67,96,103] these zigzag-chain structures do not reflect the threefold symmetry of the substrate. This behavior indicates that intermolecular interactions dominate the formation of the

ordered chain structures. The same chain motifs were reproduced in MD simulations performed on a graphene substrate, which features weaker molecule–substrate interactions and lacks site-specific adsorption. These simulation results further emphasize the crucial role of intermolecular interactions, particularly hydrogen bonding, in determining the structural arrangements.

5.5 Conclusions

This study examines the self-assembled structures of racemic and enantiopure (*M*)-[7]TH-diol on Ag(111) using STM observations and MD simulations. In contrast to many helicenes and their derivatives, both *rac*- and (*M*)-[7]TH-diols formed identical zigzag chains. Notably, the chain structures formed by the (*M*)-type [7]TH-diol on Ag(111) were not affected by the surface symmetry, in contrast to other enantiopure helicene derivatives, which typically form triangular or hexagonal motifs reflecting the threefold surface symmetry. Although [7]TH-diol maintains adsorption characteristics similarly to [7]TH owing to weak molecule–substrate interactions, the hydroxymethyl groups significantly affect intermolecular interactions, particularly in homochiral systems. The hydroxymethyl groups facilitate hydrogen bonding, stabilizing homochiral dimers and enabling their assembly into extended chain-like structures. In contrast, heterochiral assemblies are dominated by van der Waals interactions between the helical skeletons, as steric constraints hinder hydrogen bond formation. The zigzag-chain motifs observed experimentally were successfully reproduced by MD simulations, confirming that intermolecular interactions outweigh molecule–substrate interactions in directing self-assembly. Notably, the structural differences between [7]TH and [7]TH-diol chains highlight the critical role of terminal functional groups. These insights enhance our understanding of the relationship between the molecular structure and the self-assembly, providing insight into the molecular design principles for surface-confined chiral architectures with tunable properties.

Chapter 6

Interplay of Molecule–Substrate and Intermolecular Interactions in [5]Thiaheterohelicene Assembly on Ag(111)

The main results presented in this chapter have been published in the following paper.

Changqing Ye, Takuma Hattori, Yuji Hamamoto, Pawel Krukowski, Akira Saito, Hideji Osuga, Yoshitada Morikawa, and Yuji Kuwahara, "Interplay of Molecule–Substrate and Intermolecular Interactions in [5]Thiaheterohelicene Assembly on Ag(111)," submitted (under review).

6.1 Introduction

Previous studies[67,70,98,101,103,158,161,162] have shown that helicenes with a larger helical length, such as [7]CH and its functionalized derivatives, tend to form representative ordered structures on the metal surfaces. As discussed in the Chapters 4 and 5, both pristine [7]TH[158] and [7]TH-diol[162] exhibit characteristic self-assembled motifs on Ag(111) that are largely preserved across different experimental conditions, reflecting strong intermolecular recognition governed by their pronounced helicity and steric features. These systems therefore serve as model examples illustrating how molecular chirality and intermolecular interactions direct the formation of two-dimensional chiral assemblies on Ag(111).

In contrast,[5]TH (Figure 6.1) on Ag(111) exhibits distinctly different behavior as the molecular coverage increases. Unlike the circular protrusions typically observed for [7]TH in STM images, individual [5]TH molecules appear as crescent-

shaped features. As introduced in Section 2.2.3, *rac*-[5]TH forms several different ordered structures on Ag(111) depending on the coverage.[72] At submonolayer coverage, the molecules assemble into a honeycomb-like structure with relatively low packing density. However, no high-resolution images of individual molecules with clearly resolved chirality were obtained, which was likely due to random molecular orientations and possible rotational motion within the porous network. Upon increasing the coverage toward saturation, instead of forming a single dominant packing motif, the molecules self-assemble into more compact, ordered domains composed of aligned molecular rows. Specifically, structure I consists of face-to-face molecular pairs forming linear rows, while structure II is composed of tetrameric units that also align into row-like patterns, as illustrated in Figure 6.2. These ordered domains with different molecular arrangements were observed to coexist on the same terrace. Although the structures possess nearly identical molecular densities, their formation mechanisms cannot be distinguished based solely on STM observations.

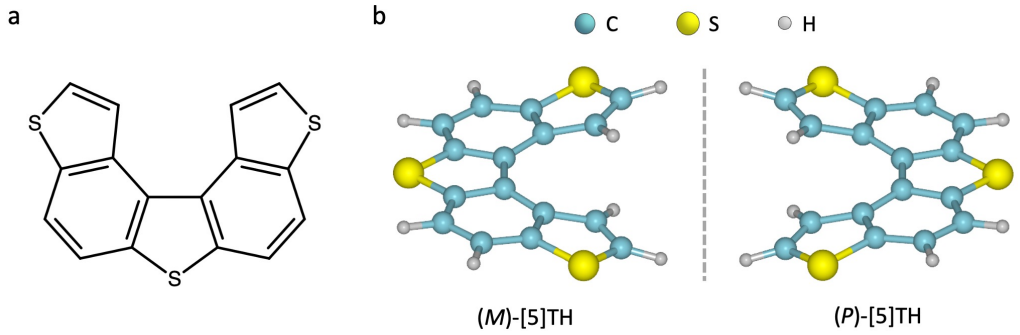


Figure 6.1: (a) Molecular structure of *rac*-[5]TH and (b) its three-dimensional models of both enantiomers. Cyan, yellow, and gray spheres represent C, S, and H atoms, respectively.

In this chapter, I present a theoretical study of the adsorption and self-assembly behavior of *rac*-[5]TH on Ag(111) using MD simulations and DFT calculations. Compared with longer helicenes, [5]TH possesses a smaller helical pitch and a reduced steric structure, which is expected to weaken intermolecular recognition and thereby enhance the relative importance of molecule–substrate interactions. Therefore, [5]TH provides a meaningful contrast to [7]TH for studying how the number of fused aromatic rings, namely, degree of helicity, influences the formation and stability of two-dimensional chiral assemblies.

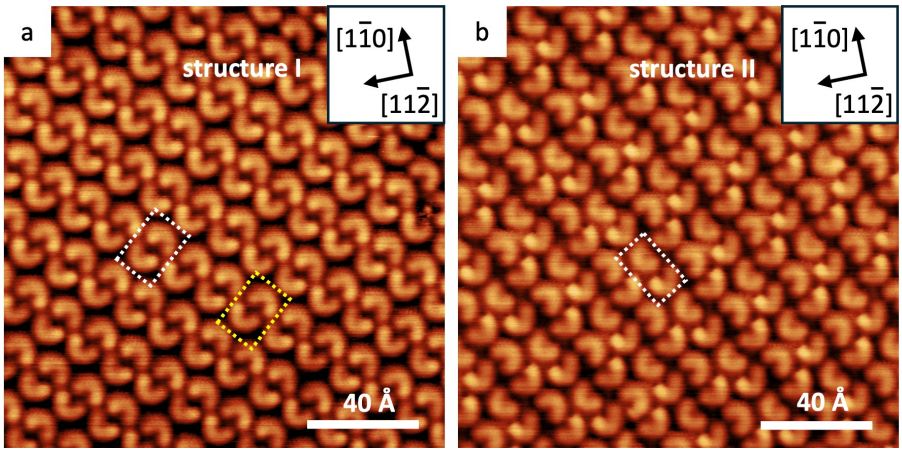


Figure 6.2: STM images of two ordered structures formed by *rac*-[5]TH on Ag(111): (a) structure I and (b) structure II. The frames highlight the representative dimer units of each ordered structure. The STM images were obtained at 0.5 V, 50 pA.

6.2 Methods

The basic setup of MD simulations followed the same protocol as in chapter 4. The simulation cell dimensions were 34.4×34.0×40.0 Å^3, and periodic boundary conditions were applied in all three directions. In the experiments, *rac*-[5]TH was deposited at 170 °C while the Ag(111) substrate were maintained at room temperature, and STM scanning was performed at 80 K. However, it remains unclear at which stage the ordered structures begin to form. In the previous simulations, the temperature was held at 275 K during equilibration. In this study, due to relatively weak intermolecular interactions between [5]TH (as discussed later), a lower temperature was employed to prevent dimer dissociation at low coverages. Specifically, the system was first equilibrated at 250 K for 500000 timesteps (0.5 ns), followed by cooling to 80 K at a rate of 100 K/ns. Finally, it was equilibrated at 80 K for an additional 500000 timesteps (0.5 ns). The data from the last 100 ps was extracted for further analysis.

The computational details of the DFT calculations for structural optimization were identical to those described in chapter 4. The Ag(111) surface was modeled by a 6×6 surface unit cell with a calculated lattice constant of 4.09 Å. The slab consisted of three atomic layers, and the bottom layer was fixed at bulk positions. A vacuum spacing of approximately 22 Å was introduced to eliminate interactions between periodic images. Brillouin-zone sampling was performed using a 4×4×1 *k*-point mesh. To investigate intermolecular interactions between dimers, the molecules were placed in a 37.04×37.04×26.46 Å^3 unit cell. Struc-

tural optimizations were performed until the residual forces on all atoms were below 5.14×10^{-2} eV Å^{-1}. Simulated STM images were generated using the Tersoff–Hamann approximation[112,113,163] with a threshold of 1.0×10^{-4} e Å^{-3}.

The adsorption energy (E_{ads}) between an adsorbate and the surface and interaction energy (E_{int}) between two molecules within a dimer were defined as

$$E_{\mathrm{ads}} = (E_{\mathrm{molecule/substrate}} - nE_{\mathrm{molecule}} - E_{\mathrm{substrate}})/n \tag{6.1}$$

$$E_{\mathrm{int}} = (E_{\mathrm{dimer}} - 2E_{\mathrm{molecule}})/2 \tag{6.2}$$

Where $E_{\mathrm{molecule/substrate}}$, E_{molecule}, $E_{\mathrm{substrate}}$, E_{dimer} are the total (potential) energies of the adsorption system, the single free molecule, the clean surface, and the dimer system in DFT calculations (MD simulations), respectively. *n* represents the number of molecules.

6.3 MD Investigation of Intrinsic Molecular Recognition of [5]TH

Based on previous studies of [7]TH and its derivatives,[72,158,162] the formation of ordered surface structures has often been interpreted as being governed primarily by molecular recognition between neighboring molecules. I first investigated the intrinsic molecular recognition of [5]TH by performing MD simulations on graphene. The same protocol previously applied to the [7]TH-diol system was adopted, as described in Chapter 5.

To investigate the self-assembly behavior of *rac*-[5]TH, 100 independent MD simulations were performed, each starting from different initial configurations involving either two different enantiomers (*M–M*) or two identical enantiomers (*M–P*). A series of trajectory snapshots illustrates the behavior of two different [5]TH enantiomers on graphene during equilibration at 250 K is shown in Figure 6.3a. Starting from random initial configurations, the two different enantiomers move across the surface and eventually form dimers. A structural rearrangement occurs during the equilibration at the high temperature.

Due to the nearly circular shape of [5]TH on the surface, the distance between the geometric centers of the molecules, d_{int}, shows a minor variation with time, as shown by the blue curve in Figure 6.3b. To better capture changes in dimer configurations, the off-centered distance between two sulfur atoms, $d_{\mathrm{s-s}}$ (green curve in Figure 6.3b), was also measured. Discrete step changes in $d_{\mathrm{s-s}}$ correspond to

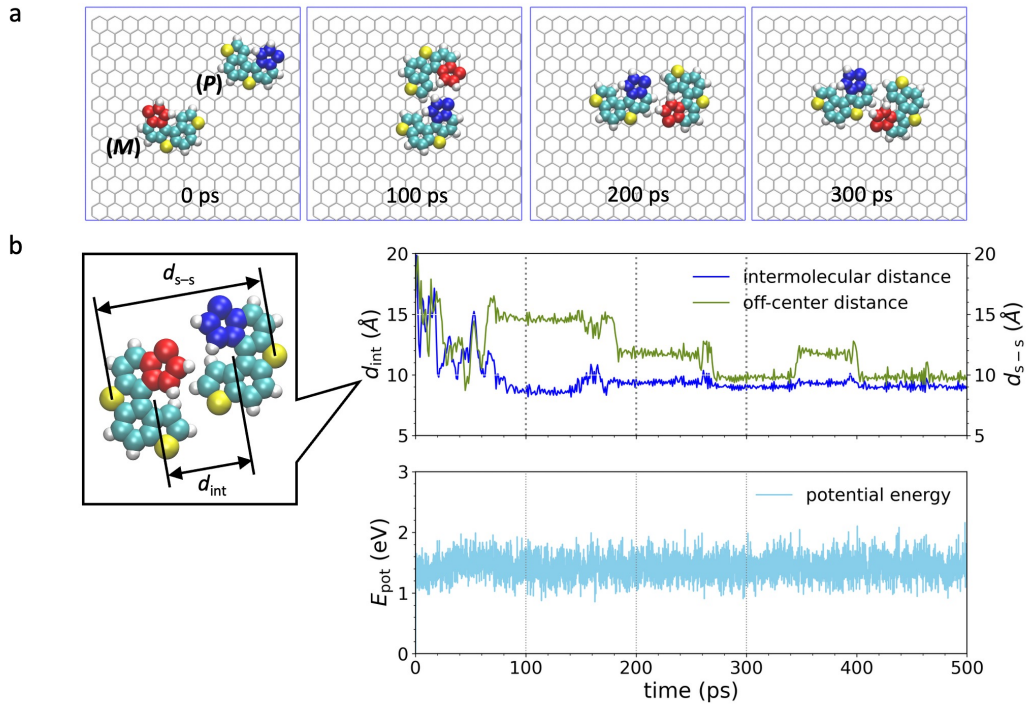


Figure 6.3: (a) Representative trajectory snapshots of two different [5]TH enantiomers on graphene. To distinguish the enantiomers, the uppermost thiophene ring of the (*M*)-type enantiomer is highlighted in red, while that of the (*P*)-type enantiomers is highlighted in blue. (b) Corresponding time evolution of intermolecular distance between the geometric centers of two molecules (d_{int}) and the sulfur–sulfur distance between the middle thiophene rings ($d_{\mathrm{s-s}}$) (upper panel) and system potential energy (E_{pot}) (lower panel).

transitions between different dimer configurations. Although the relative orientations of the molecules evolve during the equilibration, the system's potential energy E_{pot} only fluctuate around an average value with small variations (lower panel in Figure 6.3b). This suggests that the energy barriers between different dimer arrangements are small, allowing the molecules to adjust their configurations on the surface.

In most cases, dimer formation occurred and the resulting dimers remained stable throughout the simulation. However, in a fraction of trajectories, transient dimer formation was observed: the molecules initially assembled into dimers but subsequently separated and remained as isolated monomers on the surface. This behavior contrasts with that of [7]TH, for which dimer formation is highly stable and nearly irreversible. For both homochiral and heterochiral systems, approximately 70% of the simulations resulted in stable dimer formation, while the remaining $\sim$30%

ended with monomers dispersed on the surface.

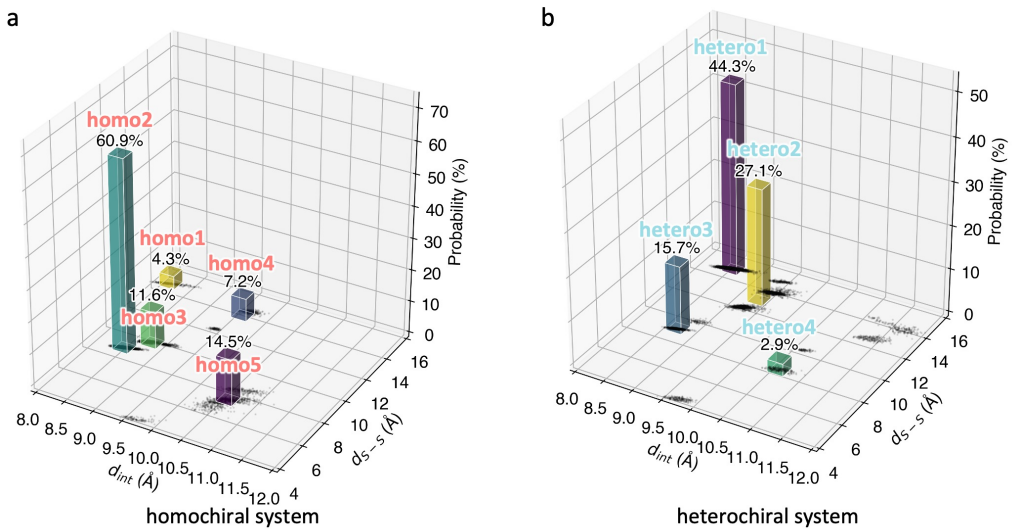


Figure 6.4: Three-dimensional histograms showing the formation probability of different dimer configurations in homochiral systems and (b) heterochiral systems. The x- and y-axes represent the intermolecular distance between the geometric centers (d_{int}) and the sulfur–sulfur distance between the middle thiophene rings ($d_{\mathrm{s-s}}$), respectively, while the z-axis indicates the formation probability of each dimer configuration.

After cooling the systems to 80 K to match the STM measurement conditions, d_{int} and $d_{\mathrm{s-s}}$ were plotted and K-means clustering were then applied to classify different dimer configurations (Figure 6.4). In the homochiral system, five distinct dimer configurations were obtained from the simulations, as illustrated in Figure 6.5a, while four distinct dimer configurations were identified in the heterochiral system (Figure 6.5b). Despite the diversity of observed dimer geometries, their intermolecular interaction energies (E_{int}) are found to be closely spaced, about 10 meV, indicating weak energetic discrimination among different binding motifs. Among the identified configurations, one homochiral and one heterochiral dimers exhibit geometric features consistent with the dimer motifs observed in STM images: **homo1**, in which two molecules are rotated by approximately 180° with respect to each other, such that their concave edges face each other symmetrically, and **hetero2**, in which the molecules are rotated by about 90°, with the concave edge of one molecule facing the lateral side of the other. These configurations were therefore chosen as representative motifs for subsequent analysis of intermolecular interactions.

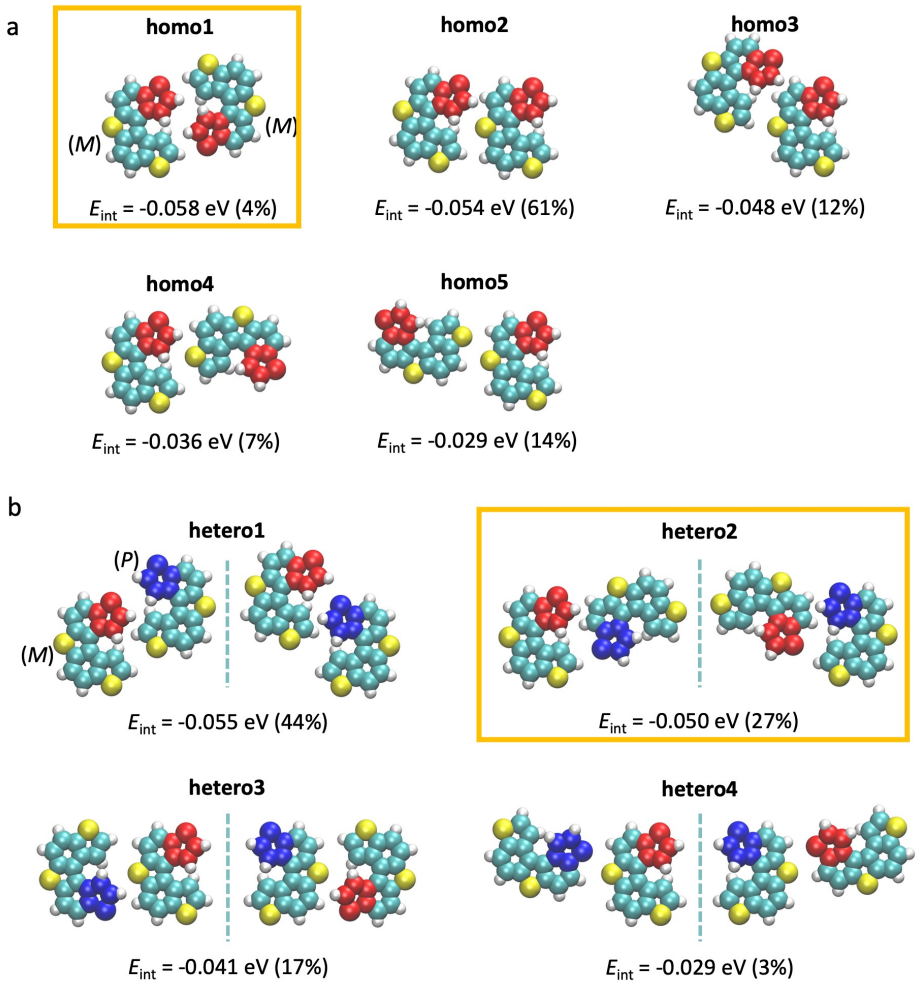


Figure 6.5: Representative (a) homochiral and (b) heterochiral dimer configurations obtained from MD simulations, with the corresponding interaction energies and formation probabilities indicated below. Two dimer configurations that resemble STM observed dimer motifs are highlighted by yellow frames.

To further characterize the intermolecular interaction landscape, two-dimensional interaction energy maps were constructed for the representative dimers, **homo1** (Figure 6.6a) and **hetero2** (Figure 6.6b). One molecule ((*M*)-[5]TH) was fixed at the middle of the graphene, while the second molecule was laterally displaced across the surface in the *xy*-plane on a grid with a step size of 0.1 Å. The intermolecular interaction energy was then evaluated for each configurations. For both homochiral and heterochiral cases, two shallow energy minima were identified, and corresponding dimer configurations are shown in Figure 6.6c, d.

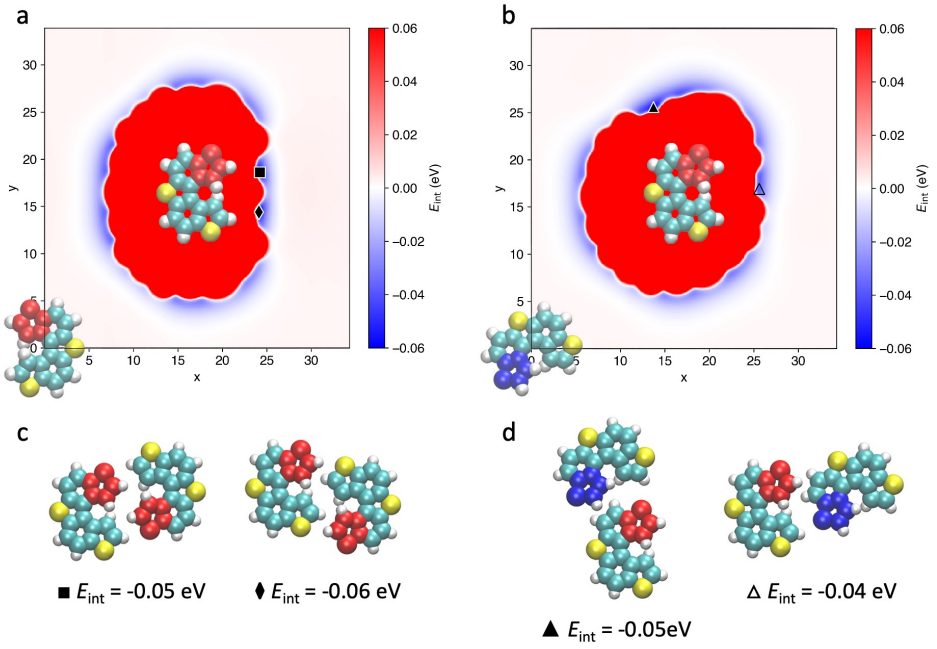


Figure 6.6: Two-dimensional intermolecular interaction energy maps of (a) homochiral and (b) heterochiral [5]TH dimers on graphene. The first molecule (*M*-[5]TH) is fixed at the center of the substrate, while the second molecule is laterally displaced in the surface plane. The *x* and *y* axes represent the lateral displacement of the geometric center of the second molecule. The symbols ■, ♦ in (a) and ▲, △ in (b), mark the local energy minima in the interaction energy profiles. The optimized dimer configurations corresponding to the energy minima are shown below the maps.

The number of molecules in the system was then increased to 4, 6, and 8 while keeping the unit cell fixed, corresponding to molecular densities of 0.34, 0.51, and 0.68 molecules/nm^2, respectively. At eight molecules, the density matches that experimentally observed for the ordered structures (0.7 molecules/nm^2 for structure I, 0.69 molecules/nm^2 for structure II). However, even in the eight-molecule sys-

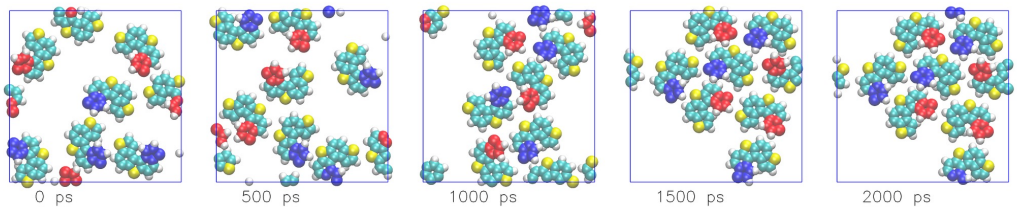


Figure 6.7: Representative trajectory snapshots of eight [5]TH enantiomers on graphene. The graphene substrate is rendered transparent for clarity. During equilibration at 250 K, the molecules continuously reorient and rearrange, leading to the formation of different intermolecular configurations.

tem, the molecules continuously rearranged on the surface, and no persistent long-range order emerged during the simulations (Figure 6.7). Instead, the molecules continuously reoriented and rearranged, indicating that intermolecular interactions alone do not provide sufficient selectivity to stabilize extended ordered structures of [5]TH. This behavior contrasts with that of [7]TH systems,[158] for which MD simulations successfully reproduce experimentally observed chain assemblies. These results demonstrate that intrinsic molecular recognition is insufficient to stabilize the formation of extended ordered structures of [5]TH, highlighting the necessity of explicitly considering the role of the Ag(111) substrate in the self-assembly process.

6.3.1 Single-Molecule Adsorption of [5]TH on Ag(111)

To evaluate the molecule–substrate interactions, the adsorption behavior of an individual [5]TH molecule on Ag(111) was investigated using DFT calculations. The adsorption geometry was systematically explored by varying the adsorption site (the top, fcc-hollow, hcp-hollow, and bridge sites), molecular height d, and azimuthal angle θ relative to the Ag(111) lattice (Figure 6.8), while keeping the molecular geometry fixed.

As shown in Figure 6.9a, the enantiomer exhibits a clear energy minimum at an equilibrium height of d = 3.3 Å, which is comparable to that reported for [7]TH on Ag(111).[158] This adsorption distance is characterize of van der Waals interactions between aromatic molecules and metal surfaces,[164,165] indicating that [5]TH is physisorbed on Ag(111). To further elucidate the molecule–substrate interactions, the orientation dependence of adsorption was explored by rotating the molecule at d = 3.3 Å. The adsorption energy exhibits a clear dependence on the azimuthal orientation with respect to the substrate for both enantiomers (Figure 6.9b), reflecting anisotropic interactions between the molecular framework and the Ag(111) lattice.

For the (*M*)-type enantiomer, the most stable configuration corresponds to an ad-

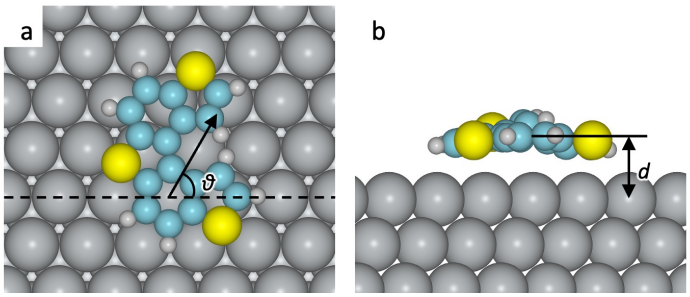


Figure 6.8: (a) Top and (b) side views of (*M*)-[5]TH on Ag(111). The molecular position is defined by the geometric center of the second benzene ring proximal to the surface. The molecular orientation is described by azimuthal angle θ, measured anti-clockwise from the close-packed direction of the Ag(111) surface atoms, as indicated by the black arrow. The molecule–substrate distance d is defined as the distance between the geometric center of the second benzene ring of the molecule to the center of the atoms in the topmost Ag layer.

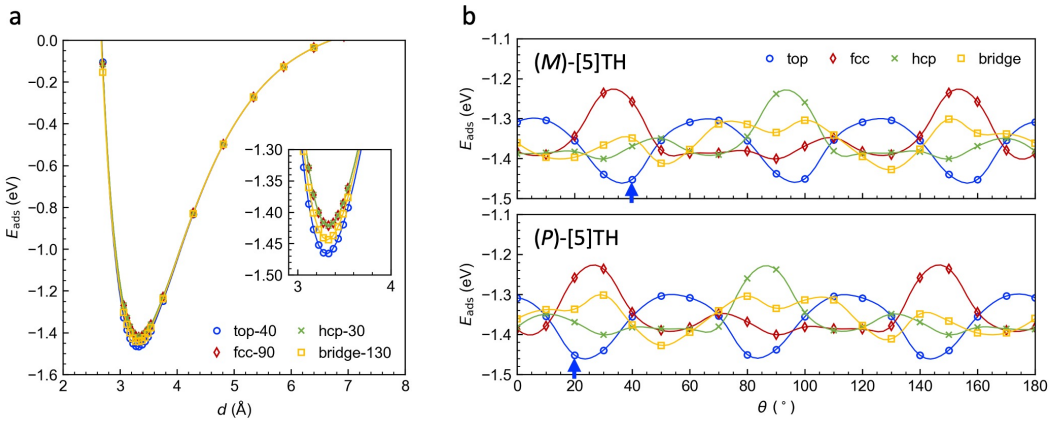


Figure 6.9: (a) Adsorption energy (E_{ads}) as a function of molecular height for a single (*M*)-[5]TH on Ag(111). Insets show enlarged views around the energy minima. (b) Orientation dependence of the E_{ads} at d = 3.3 Å. The upper and lower panels correspond to (*M*)- and (*P*)-[5]TH, respectively.

sorption geometry at the top site with an azimuthal orientation of 40° relative to the close-packed direction of surface atoms (top-40), whereas the (*P*)-type enantiomer preferentially adopts a stable configuration at top-20, reflecting mirror relationship between two enantiomers with respect to close-packed atomic direction. Both enantiomers were subsequently fully relaxed at their respective most stable adsorption geometries, and optimized structures are shown in Figure 6.10a. The calculated adsorption energies are identical for the two enantiomers, with $E_{\mathrm{ads}} = -1.76$ eV.

Simulated STM images based on the optimized adsorption geometries (Figure 6.10b) reproduce the characteristic crescent-shaped appearance in the experimental STM image, in which a single bright protrusion appears at one end of the molecule. This asymmetric contrast arises from height variations within the adsorbed molecule, where the higher molecular part looks brighter in the STM image. Based on the crescent-shaped contrast and the direction of brightness decrease along the molecular backbone, the chirality and adsorption orientation of individual enantiomers can therefore be unambiguously assigned, which was not possible in previous STM studies.[72] Specifically, an anti-clockwise brightness decrease corresponds to the (*M*)-type enantiomer, whereas a clockwise decrease corresponds to the (*P*)-type enantiomer (Figure 6.10c).

6.4 Intermolecular Interactions of [5]TH Dimers

To investigate intermolecular interactions between [5]TH molecules, [5]TH dimers were evaluated in the absence of the Ag(111) substrate. The dimer configurations were extracted from MD simulations, and two characteristic motifs were considered: a homochiral dimer composed of two identical enantiomers arranged in an antiparallel face-to-face arrangement with a relative rotation of approximately 180°, and a heterochiral dimer consisting of one (*M*)- and one (*P*)-[5]TH molecules arrange in a face-to-side configuration with a relative rotation of approximately 90°, as illustrated in Figure 6.2. In the calculations, the molecular geometries were taken from the optimized adsorption structures, and the substrate was removed to eliminate molecule–substrate contributions. Interaction energy maps were generated by fixing one molecule ((*M*)-[5]TH) and systematically varying the position of the second molecule in the *xy*-plane using a grid spacing of 0.5 Å, with E_{int} calculated for each configuration. The computational approach is comparable to that used in MD simulations discussed in Section 6.3.

For the homochiral dimer, the interaction energy profile exhibits two distinct local minima with E_{int} of -0.07 eV, marked by filled symbols ■, ♦ in Figure 6.11a. These minima correspond to two closely related configurations as : homochiral dimer 1, in which the upper thiophene rings of the two molecules stay close with a distance of 6.2 Å, and homochiral dimer 2, in which the upper thiophene rings are

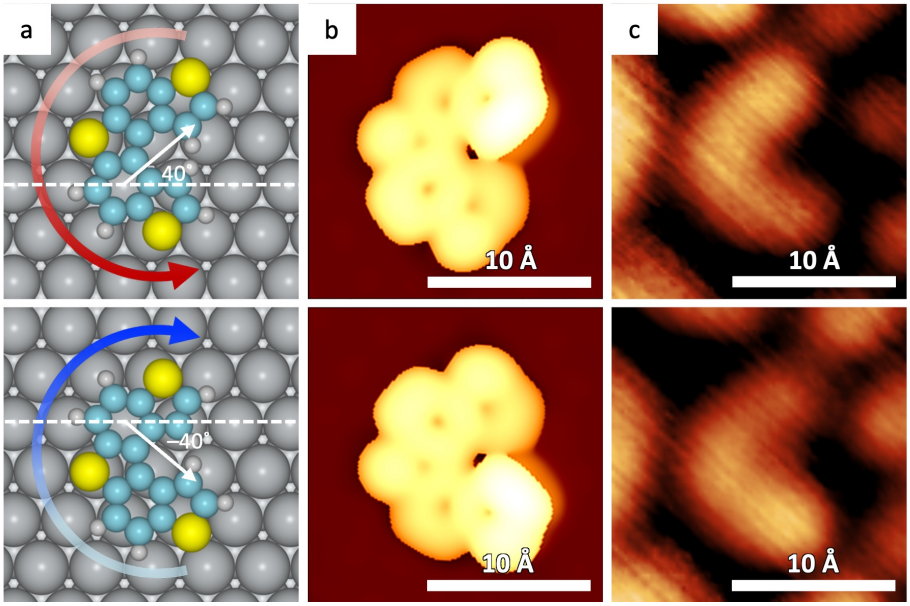


Figure 6.10: (a) Optimized adsorption geometries and (b) simulated STM images for (*M*)-[5]TH (upper) on the top-40 site and (*P*)-[5]TH (bottom) on the top-20 site. Red and blue arrows indicate the direction of the molecular spiral toward the surface. Dashed lines denote the close-packed directions of the Ag(111) surface atoms, and white arrows indicate the molecular orientations, which are mirror images with respect to the close-packed direction. (c) Corresponding experimental STM images of (*M*)- (upper) and (*P*)-[5]TH (bottom). The STM images were obtained at 0.5 V, 50 pA.

more widely separated, with a distance of 9.5 Å. Both configurations resemble the dimer motifs observed in STM images, where the bright protrusions appear either closer together or farther apart, as highlighted by the white and yellow frames in Figure 6.2a, respectively. In the STM images, the corresponding distances between the bright protrusions are approximately 9.4 Å and 12.3 Å, respectively, which are larger than the separations obtained from the calculations.

Similarly, the interaction energy profile of the heterochiral dimer exhibits two local minima, both with E_{int} of -0.04 eV, whose positions are marked ▲ by in the map of Figure 6.11b. The corresponding configurations, denoted as heterochiral dimer 1 and 2, are mirror images of each other. In the calculated structures, the separation between the bright protrusions is 6.6 Å, whereas the corresponding distance in the STM images is approximately 8.5 Å.

Compared with the MD simulations results in Section 6.3, the DFT calculations resolved clearer energy differences between the distinct dimer configurations. This improved energetic discrimination facilitates the identification of representa-

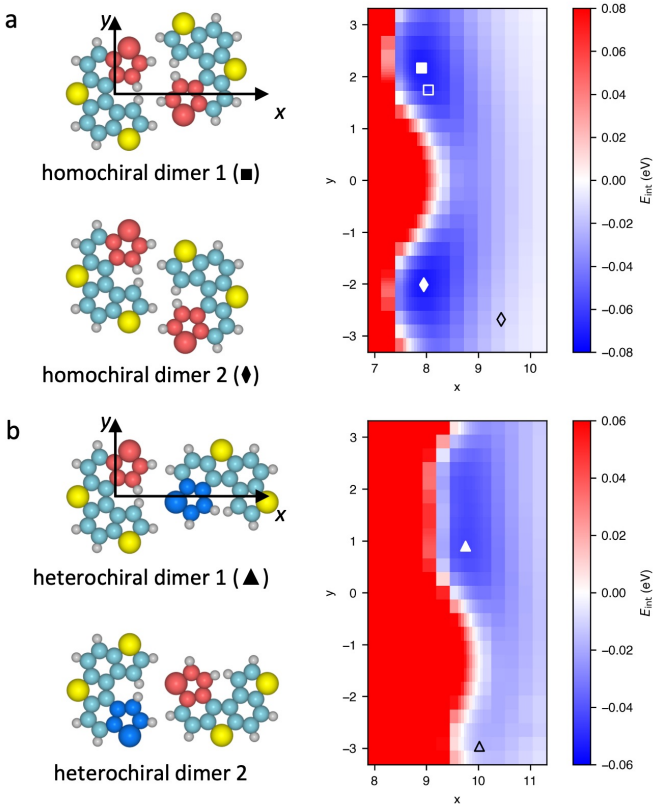


Figure 6.11: Two-dimensional intermolecular interaction energy maps of (a) homochiral and (b) heterochiral dimers. The x and y axes represent the relative lateral displacement of the geometric center of the second molecule with respect to the fixed molecule in the surface plane. The optimized dimer configurations corresponding to the energy minima are shown on the left of each map: homochiral dimer 1 (■) and dimer 2(⧫), and heterochiral dimer 1(▲) and 2. The energy map of heterochiral dimer 2 is a mirror image of that of heterochiral dimer 1 and is therefore not shown. The unfilled symbols (□, ◊ in (a), and △ in (b)) represent dimer configurations that relaxed to occupy the most stable adsorption sites on Ag(111).

tive homochiral and heterochiral dimer motifs relevant to the experimentally observed structures. However, even at the DFT level, the intermolecular interaction energies remain weak with only small difference, indicating that intermolecular interactions alone provide only limited selectivity in the formation of ordered structures of [5]TH.

6.5 Competition between Adsorption-Site Registry and Intermolecular Distance Optimization

The optimized homochiral and heterochiral dimer configurations were subsequently placed onto the Ag(111) substrate in order to investigate their stability under adsorption-site registry constraints. As discussed above, the adsorption of [5]TH on Ag(111) exhibits a pronounced dependence on both adsorption site and molecular orientation, therefore, individual molecules are expected to preferentially occupy their most stable adsorption geometries. Accordingly, in each dimer one molecule ((*M*)-[5]TH) was fixed at its most stable adsorption site and orientation (top-40; shown as the left-side molecule in Figure 6.12a–d). To maintain the optimized dimer geometries, the second molecules was consequently displaced from its energetically preferred adsorption site, as illustrated as the right-side molecule in Figure 6.12a–d. The molecular geometries were taken from the optimized single-molecule adsorption structures and kept fixed during the calculations, while the adsorption height was allowed to relax in order to locate the minimum-energy configuration.

The adsorption-site energy cost associated with dimer formation, ΔE_{site}, was defined as the difference between the adsorption energy of the displaced molecule and that of an isolated molecule adsorbed at its most stable site. For the homochiral dimers, the E_{ads} of the displaced molecules are -1.42 eV and -1.39 eV for homochiral dimer 1 and 2 (Figure 6.12a, b), respectively. Compared with -1.76 eV for adsorption at the most stable top-40 site, these values correspond to ΔE_{site} of 0.34 eV and 0.37 eV. Similarly, for the heterochiral dimers, the displaced molecule exhibit E_{ads} of -1.43 eV and -1.31 eV for heterochiral dimer 1 and 2 on Ag(111) (Figure 6.12c, d), yielding ΔE_{site} of 0.33 eV and 0.45 eV, respectively.

To evaluate the energy cost associated with deviations from the optimal intermolecular distance under surface constraints, lateral relaxation of the second molecule towards a nearby top site was considered while preserving the overall dimer motif. The intermolecular interaction energies of these relaxed dimers (indicated by unfilled symbols in Figure 6.11) were then evaluated and compared with those of the corresponding optimized dimers. Here, $\Delta E_{\mathrm{distance}}$ reflects the difference in intermolecular interaction energy of optimized dimer and the laterally re-

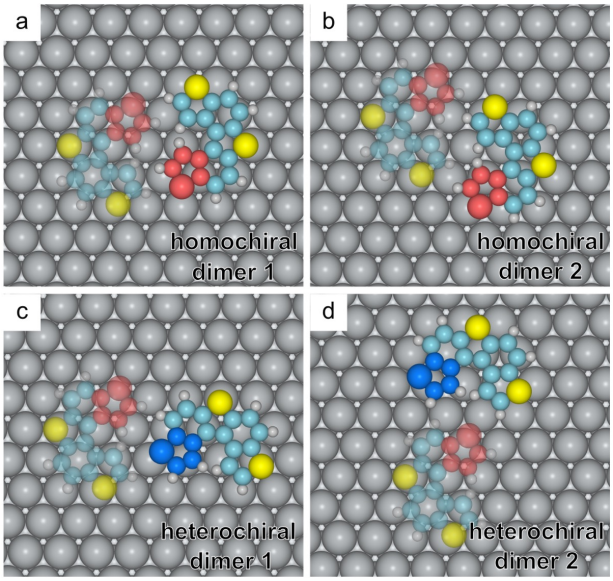


Figure 6.12: Adsorption configurations of the displaced [5]TH molecules on Ag(111) corresponding to the optimized dimer geometries. The left-side (*M*)-[5]TH is located at the most stable adsorption site (top-40) and used as the reference. The second molecule is placed at the corresponding site-shifted on the surface for evaluating the adsorption-site energy cost, ΔE_{site}. (a, b) Configurations derived from the homochiral dimers and (c, d) from the heterochiral dimers at the optimized intermolecular distances. E_{ads} was evaluated only for the second molecule. The calculated E_{ads} values of the displaced molecule are (a) -1.42 eV and (b) -1.39 eV for homochiral cases, and (c) -1.43 eV and (d) -1.28 eV for the heterochiral cases.

laxed configuration.

In the homochiral case, the relaxed configurations yield E_{int} of -0.07 eV for homochiral dimer 1 ($\square$) and -0.02 eV for homochiral dimer 2 ($\lozenge$), corresponding to $\Delta E_{\mathrm{distance}}$ of approximately 0.05 eV relative the optimized intermolecular minima. In the heterochiral case, both relaxed configurations exhibit E_{int} of -0.02 eV ($\triangle$), corresponding to $\Delta E_{\mathrm{distance}}$ of approximately 0.04 eV.

The adsorption-site energy cost associated with dimer formation on Ag(111) ($\Delta E_{\mathrm{site}} \approx$ 0.3–0.5 eV) is nearly an order of magnitude larger than the energy cost arising from deviations from optimal intermolecular distances ($\Delta E_{\mathrm{distance}} \approx$ 0.01–0.04 eV). This energetic imbalance demonstrates that molecule–substrate interactions dominate the formation of ordered structure of *rac*-[5]TH on Ag(111), while intermolecular interactions play a secondary role, accommodating the adsorption geometry imposed by substrate.

6.6 Molecular Models of Ordered [5]TH Structures

Based on the energetic hierarchy between molecule–substrate and intermolecular interactions, molecular models were constructed for the long-range ordered structures observed in STM. Experimental STM images show that all molecules within ordered structures adopt uniform azimuthal orientations and form commensurate ordered phases with respect to the Ag(111) lattice. Notably, the preferred molecular orientations predicted by DFT calculations (40° for (*M*)-[5]TH and 20° for (*P*)-[5]TH relative to Ag(111) lattice) are consistent with the orientations observed experimentally.

Accordingly, the molecular models were generated by placing all [5]TH molecules at their most stable adsorption sites with orientations determined from the single-molecule DFT results. Local intermolecular arrangements were then guided by the representative homochiral and heterochiral dimer motifs identified from DFT calculations, which capture the preferred local packing patterns without requiring fully optimizing intermolecular distances. To reproduce the experimentally observed long-range order, the unit-cell periodicities were taken directly from STM measurements, while the local molecular arrangements were defined by the DFT-derived dimer motifs.

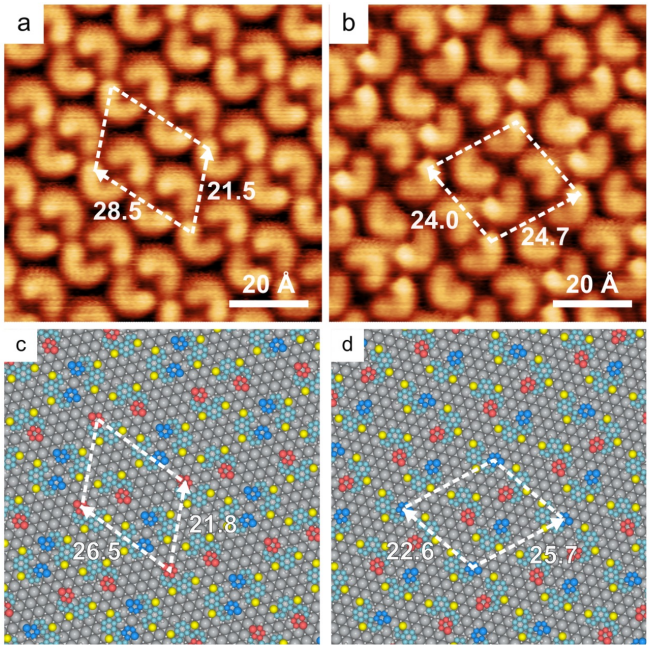


Figure 6.13: STM images of (a) structure I and (b) structure II with unit cells. The STM images were obtained at 0.5 V, 50 pA. (c) and (d) Corresponding structural models of structure I and structure II on Ag(111). White frames indicate the unit cells.

The resulting molecular arrangements and unit cell periodicities are shown in Figure 6.13c, d. In these models, the molecular arrangements are constrained to remain commensurate with the Ag(111) lattice. For structure I, the calculated unit cell is 21.8×26.5 Å^2, compared with 21.5×28.5 Å^2 obtained experimentally (Figure 6.13a). For structure II, the calculated unit cell is 25.7×22.6 Å^2 compared with 24.7×24.0 Å^2 derived from STM images (Figure 6.13b). The deviations in uni-cell lengths are within approximately 8%, which can be attributed to uncertainties in STM-based unit-cell determination, suggesting good agreement between the proposed models and experimental observations.

This energetic hierarchy also explains why MD simulations performed on graphene fail to reproduce long-range ordered structures for [5]TH. On graphene, where the adsorption energy potential is relatively flat and no preferred adsorption registry exists, the weak and nearly equivalent intermolecular interactions of [5]TH are insufficient to select a unique packing pattern, leading to continuous molecular rearrangements rather than stable periodic self-assembled motifs. In contrast, DFT calculations on Ag(111) reveal an adsorption landscape that provides a strong positional and orientational template, anchoring [5]TH molecules to specific sites and orientations. This substrate-imposed constraint enables the formation of ordered assemblies even in the presence of weak intrinsic intermolecular recognition between [5]TH.

6.7 Effect of Helical Structure on Intermolecular and Molecule–Substrate Interactions

A comparison between the molecular assemblies of [5]TH and [7]TH[158] highlights a fundamental difference in the dominant molecular recognition mechanisms that govern their self-assembly. DFT calculations show that [7]TH is physisorbed on Ag(111) with E_{ads} of –1.83 eV and exhibits a similar orientation dependence upon adsorption to that observed for [5]TH (E_{ads} = –1.76 eV). Despite the presence of molecule–substrate interactions, MD simulations performed on graphene successfully reproduce the experimentally observed zigzag chain structures of [7]TH on Ag(111), in which opposite enantiomers partially overlap their helical backbones and act as the fundamental building blocks of the assembly. This behavior demonstrates that, for [7]TH, intermolecular interactions are sufficiently strong to determine the self-assembled structure even in the absence of explicit substrate effects, with the Ag(111) surface primarily acting as a template that directs the orientation and growth of chains on the surface.

Consistent with this interpretation, DFT calculations show that intermolecular interaction energy of a representative heterochiral [7]TH dimer (E_{int} = –0.19 eV) is

substantially larger than that of [5]TH dimers ($E_{\mathrm{int}} \approx -0.07$ eV). In contrast, the [5]TH molecule exhibits pronounced site- and orientation-dependence on Ag(111), while its intrinsic intermolecular interactions provide only weak energetic discrimination among different homochiral and heterochiral dimer motifs. The intermolecular interaction energy accounts for 10% of the adsorption energy in [7]TH, whereas this ratio is reduced to 4% for [5]TH, illustrating a clear shift from intermolecularly driven recognition to substrate-guided assembly.

This difference can be attributed to the reduced helical length of [5]TH, which results in a smaller steric structure and a more extended, nearly planar footprint on the surface. This geometry enhances sensitivity to the symmetry and corrugation of the Ag(111) substrate, while simultaneously limiting the effective lateral contact area and overlap between neighboring molecules. As a result, the self-assembly of [5]TH is governed primarily by accommodation of adsorption-site constraints rather than by maximizing intermolecular binding, allowing multiple ordered phases with comparable stability to coexist on the surface.

6.8 Conclusions

The self-assembly behavior of *rac*-[5]TH on Ag(111) was investigated using a combination of MD simulations and DFT calculations, and was compared with experimental STM observations. Analysis of energetic contributions from DFT calculations reveals a clear hierarchy in which molecule–substrate interactions dominate over intrinsically weak intermolecular interactions. In particular, the energetic cost associated with deviations from the preferred adsorption sites is nearly an order of magnitude larger than that arising from non-optimal intermolecular distances, suggesting substrate registry as the primary factor governing the formation of ordered structures. The inability of MD simulations performed on graphene to reproduce long-range ordered structures further supports this substrate-guided assembly mechanism, as the absence of a corrugated adsorption potential prevents the selection of a unique packing motif.

These results show that the self-assembly of *rac*-[5]TH on Ag(111) is governed by a substrate-guided recognition mechanism. While intermolecular interactions define the local building blocks, the adsorption-site and orientation preferences imposed by the Ag(111) surface determine how these motifs are arranged into extended ordered structures. Compared with [7]TH, the reduced helical length of [5]TH weakens intermolecular recognition and shifts the balance of structural control from molecule–molecule interactions to molecule–substrate interactions, thereby enabling the coexistence of multiple ordered phases. The work in this chapter highlights molecular helicity as an effective design parameter for tuning chiral molecular architectures on solid surfaces by modifying molecular helicity to control

the balance between intermolecular and molecule–substrate interactions.

Chapter 7

Summary

In this thesis, the adsorption, self-assembly, and chiral recognition behaviors of thiaheterohelicene derivatives on Ag(111) were investigated. By integrating DFT calculations and MD simulations with experimental observations using STM, this study aimed to elucidate the molecular recognition mechanism of chiral molecules at the nanoscale.

Chapter 1 introduced the concept of chirality and its relevance in nature, and its essential role in biological recognition and scientific research. The motivation for studying chiral systems on solid surfaces was presented, together with the advantages of helicenes as model molecules for probing chirality at the molecular level.

Chapter 2 provided background on molecular chirality and helicenes, including their classification and structural characteristics. The rationale for using helicenes as a model system was discussed, followed by a review of recent studies on the self-assembly and chiral recognition of helicenes on solid surfaces.

Chapter 3 introduced computational and experimental methods employed in this work, including DFT calculations and MD simulations for evaluating molecular interactions and assembly behavior, as well as STM for surface topology observation.

Chapter 4 focused on the chiral recognition behavior of *rac*-[7]TH on Ag(111), particularly during the early stages of structure formation. After describing the computational details of DFT calculations and simulation setups, DFT results revealed an adsorption geometry in which one terminal of [7]TH lies nearly parallel on the surface. MD simulations were then used to trace the structural evolution from isolated adsorbates to chain-like aggregates on a graphene substrate, providing insights beyond the spatial resolution of STM due to high molecular mobility. The results indicated that *rac*-[7]TH preferentially forms heterochiral dimers as initial building blocks, which subsequently grow into zigzag chains stabilized by π–π interactions between the helical skeletons. The alternating arrangement of enantiomers along the chains reproduced the features observed in STM images. The influence of steric repulsion on chain alignment and interchain interactions was also examined. These

steric effects were found to play a critical role in directing long-range supramolecular structures.

Chapter 5 investigated the influence of functional groups on chiral recognition using [7]TH-diol, in which terminal hydrogen atoms are substituted by hydroxymethyl groups. STM measurements revealed that both *rac*- and (*M*)-[7]TH-diol formed similar zigzag chain structures on Ag(111), which contrast with self-assembly behavior of other helicene derivatives. However, MD simulations showed that the formation mechanisms were different between two systems: in the heterochiral case, the chains were primarily stabilized through van der Waals interactions between molecular skeletons, while in homochiral case, hydrogen bonds between terminal hydroxymethyl groups played a dominant role in chain stabilization. The results demonstrate that terminal functional groups can significantly modulate the balance of intermolecular interactions that driving different self-assembled structures.

Chapter 6 presented a theoretical study on the self-assembly behavior of *rac*-[5]TH on Ag(111), aimed at elucidating the influence of molecular length and helicity on adsorption and chiral recognition. DFT calculations showed pronounced site- and orientation-dependent adsorption of [5]TH on Ag(111), while the intrinsic intermolecular interactions were found to be weak and energetically similar among different homochiral and heterochiral dimer motifs. The substantially larger energy cost associated with deviations from preferred adsorption sites demonstrated that self-assembly is governed primarily by substrate registry, with intermolecular interactions acting as secondary constraints. Molecular models constructed by combining DFT-derived adsorption geometries with experimentally determined unit-cell parameters reproduced the observed ordered structures, while MD simulations on graphene failed to produce stable long-range order, highlighting the essential role of Ag(111) adsorption landscape. Comparison with [7]TH further reveals that reducing molecular helicity weakens intermolecular interactions and shifts the balance of controlling self-assembly from molecule–molecule interactions to molecule–substrate interactions.

Taken together, the results of this thesis establish a coherent picture of the molecular recognition mechanisms governing the self-assembly of thiaheterohelicene derivatives on Ag(111). The interplay of intermolecular interactions and molecule–substrate coupling is shown to be sensitive to molecular helicity, functionalization, and helical length. Longer helicenes such as [7]TH exhibit strong intermolecular recognition driven by π–π interaction and steric complementarity, enabling stable self-assembly even when substrate effects are not explicitly considered. Functional group substitution further modulates these interactions by introducing directional bonding motifs, such as hydrogen bonding, which can modify intrinsic molecular recognition among the molecules. In contrast, shorter helicenes

such as [5]TH possess reduced steric structure and weaker intermolecular interactions, rendering their self-assembly predominantly governed by adsorption-site registry and orientation constraints imposed by the substrate.

These findings highlight molecular helicity as a key design parameter for tuning the hierarchy of interactions that dictate chiral self-assembly at surfaces. By rationally controlling molecular structure and functionalization, it becomes possible to shift between intermolecularly driven and substrate-guided recognition regimes, thereby accessing diverse two-dimensional chiral architectures. This work provides a fundamental framework for understanding and designing chiral molecular systems on solid surfaces, with potential implications for molecular sensing, enantioselective catalysis, and surface-based nanodevices. Future studies may extend this approach to externally driven systems, such as those influenced by light or electric fields, as well as to alternative functional groups and substrate materials, further advancing the development of functional chiral interfaces.

Acknowledgements

I am deeply grateful to my supervisor, Prof. Yuji Kuwahara, for giving me the opportunity to study in his laboratory. I sincerely thank him for his excellent guidance and kind support throughout my academic studies and research.

I would also like to express my heartfelt thanks to Prof. Takuma Hattori for his generous guidance, endless patience in my research, and kind support in my daily life. My sincere appreciation goes to Prof. Yoshitada Morikawa for his valuable guidance and insightful comments on my theoretical research. I am also grateful to Prof. Yuji Hamamoto for his patient instruction and constructive discussions on my theoretical work, as well as for his support in computer programming and technical aspects, especially during my early days in research. I thank Prof. Akira Saito for his insightful advice and helpful comments on my research. I would also like to thank Prof. Pawel Krukowski for daily discussions and for providing fascinating STM images, and Prof. Hideji Osuga for synthesizing the helicene molecules used in our experiments.

I would like to thank all the past and present members of the Kuwahara Laboratory for their friendship and support. The five years I spent in the lab, during both my master's and doctoral studies, have been a truly memorable and invaluable experience. In particular, I would like to thank Mr. Masaki Okada for providing beautiful STM images and for his kind support and discussion throughout my time in the lab. I would like to thank Mr. Sho Kimura and Mr. Kento Seta for or their help and valuable discussions. I am also grateful to. I am also grateful to Ms. Kana Taniguchi for her kind conversations, which helped me relax and ease my anxiety about life in Japan. I cherish the friendship we built.

I also wish to acknowledge the essential support of our lab secretaries, Ms. Ena Ogami and Ms. Makiko Makioka, for their kind assistance and encouragement. I am grateful to Ms. Sayoko Sakai, Ms. Tomoko Kumagai, and Ms. Sawako Kudo for her help and support regarding course-related matters.

I would also like to thank all the friends I met in Japan, both on and off campus, who offered me different perspectives on my research and enriched my life with their presence.

Finally, I am deeply thankful to my parents for their unconditional love and

support. Their understanding and respect for every decision I make have been my greatest strength and encouragement.

January, 2026, at Suita, Osaka
Ye Changqing

Publication List

Publications:

1. Changqing Ye, Takuma Hattori, Yuji Hamamoto, Pawel Krukowski, Kouji Inagaki, Akira Saito, Hideji Osuga, Yoshitada Morikawa, and Yuji Kuwahara, "Chiral Recognition Mechanism of Two-Dimensional Self-Assembly Formed by [7]Thiaheterohelicene." *J. Phys. Chem. C* **2023**, *127*, 21305–21312.

2. Changqing Ye, Takuma Hattori, Yuji Hamamoto, Pawel Krukowski, Akira Saito, Hideji Osuga, Yoshitada Morikawa, and Yuji Kuwahara, "Chiral Recognition Mechanism of 2,13-Bis(hydroxymethyl)-[7]thiaheterohelicene on Ag(111) Investigated by STM and MD Simulation." *Int. J. Mol. Sci.* **2025** *26*(23), 11458.

3. Changqing Ye, Takuma Hattori, Yuji Hamamoto, Pawel Krukowski, Akira Saito, Hideji Osuga, Yoshitada Morikawa, and Yuji Kuwahara, "Interplay of Molecule–Substrate and Intermolecular Interactions in [5]Thiaheterohelicene Assembly on Ag(111), submitted (under review).

4. Sho Kimura, Takuma Hattori, Changqing Ye, Masaki Okada, Satoshi Kondo, Yui Sakurama, Akira Saito, Pawel Krukowski, and Yuji Kuwahara, "STM/TERS observation of (*M*)-type diphenyl[7]thiaheterohelicene on Ag(111)." *Phys. Chem. Chem. Phys.* **2024**, *26*, 7658.

Conferences:

1. Changqing Ye, *et al.*, "Theoretical study on the chiral recognition mechanism of thiaheterohelicene molecules using DFT and MD calculations." 2022 Kansai Thin Film · Surface Physics Seminar, Online, November 2022. (Oral presentation)

2. Changqing Ye, *et al.*, "Molecular dynamics study on chiral recognition mechanism of thiaheteroheliene molecules." The Physical Society of Japan 2023 Spring Meeting, Online, March 2023. (Oral presentation)

3. Changqing Ye, *et al.*, “Theoretical study on stereo recognition of thiaheterohelicene on Ag(111).” 36th European Conference on Surface Science (ECOSS36), Lodz, Poland, August 2023. (Oral presentation)

4. Changqing Ye, *et al.*, “Dependence of functional groups on chiral recognition of thiaheterohelicene derivatives.” The Physical Society of Japan 2024 Spring Meeting, Online, March 2023. (Poster presentation)

5. Changqing Ye, *et al.*, “Two-dimensional chiral recognition of thiaheterohelicene derivatives using molecular dynamics simulation.” The Japan Society of Applied Physics 2024 Autumn Meeting, Niigata, Japan, September 2024. (Oral presentation)

6. Changqing Ye, *et al.*, “Two-dimensional chiral recognition of thiaheterohelicene derivatives using molecular dynamics simulation.” The 10th International Symposium on Surface Science (ISSS-10), Kita-kyushu, Japan, October 2024. (Poster presentation)

7. Changqing Ye, *et al.*, ”Study on chiral recognition mechanism of thiaheterohelicene derivatives by STM and MD simulation.” SPIE Optics + Photonics 2025, San Diego, California, United States, August 2025. (Poster presentation)

8. Changqing Ye, *et al.*, ”Chiral Recognition of Thiaheterohelicene Derivatives on Ag(111).” 2025 Kansai Thin Film · Surface Physics Seminar, Kobei, Japan, November 2025. (Oral presentation)

Award:

1. The 10th International Symposium on Surface Science (ISSS-10) Student prize.

References

[1] M. Schilthuizen, P. G. Craze, A. S. Cabanban, A. Davison, J. Stone, E. Gittenberger, and B. J. Scott, Journal of Evolutionary Biology **20**, 1941 (2007).

[2] R. Ueshima and T. Asami, Nature **425**, 679 (2003).

[3] M. J. Morgan, in *Ciba Foundation symposium* (John Wiley & Sons, Ltd, 1991), Vol. 162, pp. 234–250.

[4] M. S. Sousa-Baena, J. Hernandes-Lopes, and M. A. V. Sluys, Current Opinion in Plant Biology **59**, 101982 (2021).

[5] C. Huang, Z. Wang, D. Quinn, S. Suresh, and K. J. Hsia, Proceedings of the National Academy of Sciences of the United States of America **115**, 12359 (2018).

[6] S. J. Gerbode, J. R. Puzey, A. G. McCormick, and L. Mahadevan, Science **337**, 1087 (2012).

[7] D. R. Smyth, Development **143**, 3272 (2016).

[8] T. Matsuura and H. Koshima, Journal of Photochemistry and Photobiology C: Photochemistry Reviews **6**, 7 (2005).

[9] H. Ueda, M. García-Fernández, S. Agrestini, C. P. Romao, J. van den Brink, N. A. Spaldin, K. J. Zhou, and U. Staub, Nature **618**, 946 (2023).

[10] L. Pasteur, Compt. rend. **26**, 535 (1848).

[11] L. Pasteur, Annales Chimie Phys. **24**, 442 (1848).

[12] J. Gal, Helvetica Chimica Acta **102**, e1900098 (2019).

[13] S. F. Mason, International Reviews in Physical Chemistry **3**, 217 (1983).

[14] W. A. Bonner, Origins of Life and Evolution of the Biosphere **25**, 175 (1995).

[15] D. Burke and D. J. Henderson, British Journal of Anaesthesia **88**, 563 (2002).

[16] R. Bentley, Chemical Society Reviews **34**, 609 (2005).

[17] R. Rohs, X. Jin, S. M. West, R. Joshi, B. Honig, and R. S. Mann, Annual Review of Biochemistry **79**, 233 (2010).

[18] B. Kasprzyk-Hordern, Chemical Society Reviews **39**, 4466 (2010).

[19] C. Ollivaux, D. Soyez, and J. Y. Toullec, Journal of Peptide Science **20**, 595 (2014).

[20] J. E. Hein and D. G. Blackmond, Accounts of Chemical Research **45**, 2045 (2012).

[21] D. G. Blackmond, Philosophical Transactions of the Royal Society B: Biological Sciences **366**, 2878 (2011).

[22] L. D. Barron, Space Science Reviews **135**, 187 (2008).

[23] J. S. Richardson, Advances in Protein Chemistry **34**, 167 (1981).

[24] A. S. Pillai, S. A. Chandler, Y. Liu, A. V. Signore, C. R. Cortez-Romero, J. L. Benesch, A. Laganowsky, J. F. Storz, G. K. Hochberg, and J. W. Thornton, Nature 2020 581:7809 **581**, 480 (2020).

[25] H. Fu, R. R. Subramanian, and S. C. Masters, Annual Review of Pharmacology and Toxicology **40**, 617 (2000).

[26] D. E. Koshland, Proceedings of the National Academy of Sciences **44**, 98 (1958).

[27] R. C. L. Milton, S. C. Milton, and S. B. Kent, Science **256**, 1445 (1992).

[28] E. R. Jarvo and S. J. Miller, Tetrahedron **58**, 2481 (2002).

[29] G. L. Holliday, J. B. Mitchell, and J. M. Thornton, Journal of Molecular Biology **390**, 560 (2009).

[30] A. A. Koesoema, D. M. Standley, T. Senda, and T. Matsuda, Applied Microbiology and Biotechnology **104**, 2897 (2020).

[31] M. Morvan and I. Mikšík, Separations 2021, Vol. 8, Page 112 **8**, 112 (2021).

[32] H. E. Moser and P. B. Dervan, Science **238**, 645 (1987).

[33] A. H. Wang, G. J. Quigley, F. J. Kolpak, J. L. Crawford, J. H. V. Boom, G. V. D. Marel, and A. Rich, Nature **282**, 680 (1979).

[34] N. C. Seeman, Annual Review of Biochemistry **79**, 65 (2010).

[35] H. J. Lehmler, S. J. Harrad, H. Hühnerfuss, I. Kania-Korwel, C. M. Lee, Z. Lu, and C. S. Wong, Environmental Science and Technology **44**, 2757 (2010).

[36] H. Ramezani and H. Dietz, Nature Reviews Genetics 2019 21:1 **21**, 5 (2019).

[37] L. A. Nguyen, H. He, and C. Pham-Huy, International Journal of Biomedical Science : IJBS **2**, 85 (2006).

[38] T. Huber, S. Menon, and T. P. Sakmar, Biochemistry **47**, 11013 (2008).

[39] R. Rozenfeld and L. A. Devi, Biochemical Journal **433**, 11 (2011).

[40] F. O. Battiti, S. L. Cemaj, A. M. Guerrero, A. B. Shaik, J. Lam, R. Rais, B. S. Slusher, J. R. Deschamps, G. H. Imler, A. H. Newman, and A. Bonifazi, Journal of Medicinal Chemistry **62**, 6287 (2019).

[41] R. Corradini, S. Sforza, T. Tedeschi, and R. Marchelli, Chirality **19**, 269 (2007).

[42] A. Zask, J. Murphy, and G. A. Ellestad, Chirality **25**, 265 (2013).

[43] Y. Wang, H. Huang, Q. Zhang, and P. Zhang, Dalton Transactions **47**, 4017 (2018).

[44] J. Yeom, P. P. Guimaraes, H. M. Ahn, B. K. Jung, Q. Hu, K. McHugh, M. J. Mitchell, C. O. Yun, R. Langer, and A. Jaklenec, Advanced Materials **32**, 1903878 (2020).

[45] E. Jongedijk, K. Cankar, M. Buchhaupt, J. Schrader, H. Bouwmeester, and J. Beekwilder, Applied Microbiology and Biotechnology **100**, 2927 (2016).

[46] A. J. Vieira, F. P. Beserra, M. C. Souza, B. M. Totti, and A. L. Rozza, Chemico-Biological Interactions **283**, 97 (2018).

[47] J. H. Kim and A. R. Scialli, Toxicological Sciences **122**, 1 (2011).

[48] N. Vargesson, Birth Defects Research Part C - Embryo Today: Reviews **105**, 140 (2015).

[49] T. Mallat, E. Orglmeister, and A. Baiker, Chemical Reviews **107**, 4863 (2007).

[50] R. J. Phipps, G. L. Hamilton, and F. D. Toste, Nature Chemistry **4**, 603 (2012).

[51] S. Krautwald and E. M. Carreira, Journal of the American Chemical Society **139**, 5627 (2017).

[52] J. G. Ibanez, M. E. Rincón, S. Gutierrez-Granados, M. Chahma, O. A. Jaramillo-Quintero, and B. A. Frontana-Uribe, Chemical Reviews **118**, 4731 (2018).

[53] Y. Y. Lee, R. M. Kim, S. W. Im, M. Balamurugan, and K. T. Nam, Nanoscale **12**, 58 (2019).

[54] X. Niu, X. Yang, H. Li, J. Liu, Z. Liu, and K. Wang, Microchimica Acta **187**, 1 (2020).

[55] G. Binnig and H. Rohrer, Reviews of Modern Physics **59**, 615 (1987).

[56] A. C. Anderson, M. E. Malinowski, P. Rev, E. J. Cotts, D. M. Miliotis, G. A. Northrop, G. A. Kneezel, A. V. Granato, P. B. Bev, G. Binning, H. Rohrer, C. Gerber, and E. Weibel, Physical Review Letters **49**, 57 (1982).

[57] C. J. Chen, *Introduction to scanning tunneling microscopy* (Oxford University Press, 2021), pp. 1–452.

[58] K. H. Ernst, Physica Status Solidi (B) Basic Research **249**, 2057 (2012).

[59] F. Zaera, Chemical Society Reviews **46**, 7374 (2017).

[60] X. Peng, Y. Zhang, X. Liu, Y. Qian, Z. Ouyang, and H. Kong, Small **20**, 2307171 (2024).

[61] Y. Shen and C. F. Chen, Chemical Reviews **112**, 1463 (2012).

[62] M. Gingras, Chemical Society Reviews **42**, 968 (2013).

[63] G. Gingras, Chemical Society Reviews **42**, 1051 (2013).

[64] Y. Yang, R. C. D. Costa, M. J. Fuchter, and A. J. Campbell, Nature Photonics **7**, 634 (2013).

[65] T. Mori, Chemical Reviews **121**, 2373 (2021).

[66] R. Fasel, M. Parschau, and K. H. Ernst, Nature **439**, 449 (2006).

[67] J. Seibel, L. Zoppi, and K. H. Ernst, Chemical Communications **50**, 8751 (2014).

[68] K. H. Ernst, Accounts of Chemical Research **49**, 1182 (2016).

[69] Q. Han, Z. Li, K. Sun, M. L. Tao, M. X. Shi, D. X. Yang, J. X. Xia, J. J. Wan, and J. Z. Wang, Physical Chemistry Chemical Physics **24**, 10292 (2022).

[70] S. Chaunchaiyakul, P. Krukowski, T. Tsuzuki, Y. Minagawa, M. Akai-Kasaya, A. Saito, H. Osuga, and Y. Kuwahara, Journal of Physical Chemistry C **119**, 21434 (2015).

[71] S. Chaunchaiyakul, A. Setiadi, P. Krukowski, F. C. I. Catalan, M. Akai-Kasaya, A. Saito, N. Hayazawa, Y. Kim, H. Osuga, and Y. Kuwahara, Journal of Physical Chemistry C **121**, 18162 (2017).

[72] P. Krukowski, T. Hattori, M. Okada, M. Piskorski, I. Lutsyk, A. Saito, H. Osuga, and Y. Kuwahara, Applied Surface Science **589**, 152860 (2022).

[73] B. C. Baciu, T. de Ara, C. Sabater, C. Untiedt, and A. Guijarro, Nanoscale Advances **2**, 1921 (2020).

[74] M. Stöhr, S. Boz, M. Schär, M. T. Nguyen, C. A. Pignedoli, D. Passerone, W. B. Schweizer, C. Thilgen, T. A. Jung, and F. Diederich, Angewandte Chemie - International Edition **50**, 9982 (2011).

[75] A. Mairena, J. I. Mendieta, O. Stetsovych, A. Terfort, I. G. Stará, I. Starý, P. Jelínek, and K. H. Ernst, Chemical Communications **55**, 10595 (2019).

[76] E. Tuca and I. Paci, Physical Chemistry Chemical Physics **21**, 9189 (2019).

[77] L. Kelvin, *The Molecular Tactics of a Crystal. The 2nd Robert Boyle Lecture* (Oxford Univ. Junior Sci. Club, 1894), Vol. 18, p. 25.

[78] J. Gal, Chirality **24**, 959 (2012).

[79] W. H. Brooks, W. C. Guida, and K. G. Daniel, Current Topics in Medicinal Chemistry **11**, 760 (2011).

[80] R. S. Cahn, C. Ingold, and V. Prelog, Angewandte Chemie International Edition in English **5**, 385 (1966).

[81] D. R. Klein, *Organic chemistry* (John Wiley & Sons, 2020).

[82] R. S. Cahn, Journal of Chemical Education **1**, 116 (1964).

[83] D. W. Slocum, D. Sugarman, and S. P. Tucker, Journal of Chemical Education **48**, 597 (1971).

[84] W. H. Hartung and J. Andrako, Journal of Pharmaceutical Sciences **50**, 805 (1961).

[85] J. Meisenheimer and K. Witte, Berichte der deutschen chemischen Gesellschaft **36**, 4153 (1903).

[86] K. Mori, T. Murase, and M. Fujita, Angewandte Chemie - International Edition **54**, 6847 (2015).

[87] M. S. Newman, W. B. Lutz, and D. Lednicer, Journal of the American Chemical Society **77**, 3420 (1955).

[88] M. S. Newman and R. M. Wise, Journal of the American Chemical Society **78**, 450 (1956).

[89] M. S. Newman and D. Lednicer, Journal of the American Chemical Society **78**, 4765 (1956).

[90] G. R. Kiel, H. M. Bergman, A. E. Samkian, N. J. Schuster, R. C. Handford, A. J. Rothenberger, R. Gomez-Bombarelli, C. Nuckolls, and T. D. Tilley, Journal of the American Chemical Society **144**, 23421 (2022).

[91] K. P. Meurer and F. Vögtle, in *Organic Chemistry* (Springer, Berlin, Heidelberg, 1985), pp. 1–76.

[92] G. D. Ellison and A. Zanchetti, Nature **232**, 124 (1971).

[93] H. Nakagawa, A. Obata, K. I. Yamada, H. Kawazura, M. Konno, and H. Miyamae, Journal of the Chemical Society, Perkin Transactions 2 1899 (1985).

[94] M. B. Groen, H. Schadenberg, and H. Wynberg, Journal of Organic Chemistry **36**, 2797 (1971).

[95] W. H. Laarhoven and W. J. C. Prinsen, in *Carbohelicenes and heterohelicenes* (Springer, Berlin, Heidelberg, 1984), pp. 63–130.

[96] M. Parschau, R. Fasel, and K. H. Ernst, Crystal Growth and Design **8**, 1890 (2008).

[97] R. Fasel, M. Parschau, and K. H. Ernst, Angewandte Chemie International Edition **42**, 5178 (2003).

[98] J. Seibel, M. Parschau, and K. H. Ernst, Journal of Physical Chemistry C **118**, 29135 (2014).

[99] J. Seibel, M. Parschau, and K. H. Ernst, Journal of the American Chemical Society **137**, 7970 (2015).

[100] A. Mairena, L. Zoppi, J. Seibel, A. F. Tröster, K. Grenader, M. Parschau, A. Terfort, and K. H. Ernst, ACS Nano **11**, 865 (2017).

[101] J. X. Xia, Z. Li, Q. Han, J. J. Wan, M. X. Shi, M. L. Tao, K. Sun, and J. Z. Wang, Physical Chemistry Chemical Physics **23**, 24344 (2021).

[102] O. Masaki, Master's thesis, Osaka University, 2022.

[103] S. Kimura, T. Hattori, C. Ye, M. Okada, S. Kondo, Y. Sakurama, A. Saito, P. Krukowski, H. Osuga, and Y. Kuwahara, Physical Chemistry Chemical Physics **26**, 7658 (2024).

[104] R. G. Parr and Y. Weitao, *Density-Functional Theory of Atoms and Molecules* (Oxford University Press, 1995).

[105] E. Runge and E. K. Gross, Physical Review Letters **52**, 997 (1984).

[106] W. Kohn, A. D. Becke, and R. G. Parr, Journal of Physical Chemistry **100**, 12974 (1996).

[107] V. Fock, Zeitschrift für Physik **61**, 126 (1930).

[108] D. R. H. Artree and W. H. Artree, Proceedings of the Royal Society of London. Series A - Mathematical and Physical Sciences **150**, 9 (1935).

[109] J. C. Slater, Physical Review **81**, 385 (1951).

[110] P. Hohenberg and W. Kohn, Physical Review **136**, B864 (1964).

[111] W. Kohn and L. J. Sham, Physical Review **140**, A1133 (1965).

[112] J. Tersoff and D. R. Hamann, Physical Review B **31**, 805 (1985).

[113] J. Tersoff, Physical Review B **40**, 11990 (1989).

[114] B. J. Alder and T. E. Wainwright, The Journal of Chemical Physics **31**, 459 (1959).

[115] S. A. Hollingsworth and R. O. Dror, Neuron **99**, 1129 (2018).

[116] D. Frenkel and B. Smit, *Understanding Molecular Simulation: From Algorithms to Applications, Third Edition* (Elsevier, 2023), pp. 1–728.

[117] C. I. Bayly, K. M. Merz, D. M. Ferguson, W. D. Cornell, T. Fox, J. W. Caldwell, P. A. Kollman, P. Cieplak, I. R. Gould, and D. C. Spellmeyer, Journal of the American Chemical Society **117**, 5179 (1995).

[118] J. Wang, R. M. Wolf, J. W. Caldwell, P. A. Kollman, and D. A. Case, Journal of Computational Chemistry **25**, 1157 (2004).

[119] H. Heinz and U. W. Suter, Journal of Physical Chemistry B **108**, 18341 (2004).

[120] C. Kramer, A. Spinn, and K. R. Liedl, Journal of Chemical Theory and Computation **10**, 4488 (2014).

[121] C. I. Bayly, P. Cieplak, W. D. Cornell, and P. A. Kollman, J. Phys. Chem **97**, 10269 (1993).

[122] A. Jakalian, B. L. Bush, D. B. Jack, and C. I. Bayly, Journal of Computational Chemistry **21**, 132 (2000).

[123] A. Jakalian, D. B. Jack, and C. I. Bayly, Journal of Computational Chemistry **23**, 1623 (2002).

[124] J. W. Storer, D. J. Giesen, C. J. Cramer, and D. G. Truhlar, Journal of Computer-Aided Molecular Design **9**, 87 (1995).

[125] J. Fischer and M. Wendland, Fluid Phase Equilibria **573**, 113876 (2023).

[126] J. Lenhard, S. Stephan, and H. Hasse, Annalen der Physik **536**, 2400115 (2024).

[127] J. E. Jones, Proceedings of the Royal Society of London. Series A, Containing Papers of a Mathematical and Physical Character **106**, 441 (1924).

[128] J. E. Lennard-Jones, Proceedings of the Physical Society **43**, 461 (1931).

[129] A. Rahman, Physical Review **136**, A405 (1964).

[130] L. Verlet, Physical Review **159**, 98 (1967).

[131] H. C. Andersen and J. C. Phys, The Journal of Chemical Physics **72**, 2384 (1980).

[132] H. J. Berendsen, J. P. Postma, W. F. V. Gunsteren, A. Dinola, and J. R. Haak, The Journal of Chemical Physics **81**, 3684 (1984).

[133] T. Schneider and E. Stoll, Physical Review B **17**, 1302 (1978).

[134] S. Nosé, The Journal of Chemical Physics **81**, 511 (1984).

[135] W. G. Hoover, Physical Review A **31**, 1695 (1985).

[136] M. P. Allen and D. J. Tildesley, *Computer simulation of liquids: Second edition* (Oxford University Press, 2017), pp. 1–626.

[137] H. Ascolani, M. W. V. D. Meijden, L. J. Cristina, J. E. Gayone, R. M. Kellogg, J. D. Fuhr, and M. Lingenfelder, Chemical Communications **50**, 13907 (2014).

[138] Y. Morikawa, Physical Review B **63**, 033405 (2001).

[139] Y. Morikawa, K. Iwata, and K. Terakura, Applied Surface Science **169-170**, 11 (2001).

[140] Y. Morikawa, H. Ishii, and K. Seki, Physical Review B **69**, 041403 (2004).

[141] N. Troullier and J. L. Martins, Physical Review B **43**, 1993 (1991).

[142] G. Román-Pérez and J. M. Soler, Physical Review Letters **103**, 096102 (2009).

[143] J. Wu and F. Gygi, Journal of Chemical Physics **136**, 224107 (2012).

[144] Y. Hamamoto, I. Hamada, K. Inagaki, and Y. Morikawa, Physical Review B **93**, 245440 (2016).

[145] M. Dion, H. Rydberg, E. Schröder, D. C. Langreth, and B. I. Lundqvist, Physical Review Letters **92**, 246401 (2004).

[146] I. Hamada, Physical Review B - Condensed Matter and Materials Physics **89**, 121103 (2014).

[147] M. Callsen and I. Hamada, Physical Review B - Condensed Matter and Materials Physics **91**, 195103 (2015).

[148] A. P. Thompson, H. M. Aktulga, R. Berger, D. S. Bolintineanu, W. M. Brown, P. S. Crozier, P. J. in 't Veld, A. Kohlmeyer, S. G. Moore, T. D. Nguyen, R. Shan, M. J. Stevens, J. Tranchida, C. Trott, and S. J. Plimpton, Computer Physics Communications **271**, 108171 (2022).

[149] R. Fasel, A. Cossy, K. H. Ernst, F. Baumberger, T. Greber, and J. Osterwalder, The Journal of Chemical Physics **115**, 1020 (2001).

[150] M. Shen, D. J. Liu, C. J. Jenks, and P. A. Thiel, Journal of Physical Chemistry C **112**, 4281 (2008).

[151] M. O. Sinnokrot, E. F. Valeev, and C. D. Sherrill, Journal of the American Chemical Society **124**, 10887 (2002).

[152] E. G. Hohenstein and C. D. Sherrill, Journal of Physical Chemistry A **113**, 878 (2009).

[153] D. Nečas and P. Klapetek, Open Physics **10**, 181 (2012).

[154] K. Tanaka, H. Osuga, H. Suzuki, Y. Shogase, and Y. Kitahara, Journal of the Chemical Society, Perkin Transactions 1 935 (1998).

[155] K. ichi Yamada, H. Nakagawa, and H. Kawazura, Bulletin of the Chemical Society of Japan **59**, 2429 (1986).

[156] W. D. Cornell, P. Cieplak, C. I. Bayly, I. R. Gould, K. M. Merz, D. M. Ferguson, D. C. Spellmeyer, T. Fox, J. W. Caldwell, and P. A. Kollman, Journal of the American Chemical Society **117**, 5179 (1995).

[157] H. C. Andersen, Journal of Computational Physics **52**, 24 (1983).

[158] C. Ye, T. Hattori, Y. Hamamoto, P. Krukowski, K. Inagaki, A. Saito, H. Osuga, Y. Morikawa, and Y. Kuwahara, Journal of Physical Chemistry C **127**, 21305 (2023).

[159] M. Ruben, D. Payer, A. Landa, A. Comisso, C. Gattinoni, N. Lin, J. P. Collin, J. P. Sauvage, A. D. Vita, and K. Kern, Journal of the American Chemical Society **128**, 15644 (2006).

[160] A. Maleki, S. Alavi, and B. Najafi, Journal of Physical Chemistry C **115**, 22484 (2011).

[161] H. Zhang, H. Liu, C. Shen, F. Gan, X. Su, H. Qiu, B. Yang, and P. Yu, International Journal of Molecular Sciences **20**, 2018 (2019).

[162] C. Ye, T. Hattori, Y. Hamamoto, P. Krukowski, A. Saito, H. Osuga, Y. Morikawa, and Y. Kuwahara, International Journal of Molecular Sciences **26**, 11458 (2025).

[163] I. Hamada, R. Shimizu, T. Ohsawa, K. Iwaya, T. Hashizume, M. Tsukada, K. Akagi, and T. Hitosugi, J. Am. Chem. Soc **136**, 17201 (2014).

[164] S. Adhikari, H. Tang, B. Neupane, A. Ruzsinszky, and G. I. Csonka, Physical Review Materials **4**, 025005 (2020).

[165] W. Liu, F. Maaß, M. Willenbockel, C. Bronner, M. Schulze, S. Soubatch, F. S. Tautz, P. Tegeder, and A. Tkatchenko, Phys. Rev. Lett. **115**, 036104 (2015).